




University of
Stavanger

Faculty of Science and Technology

MASTER'S THESIS

Study program/ Specialization: MSc. in Marine- and Offshore Technology	Spring semester, 2019 Open / Restricted access
Writer: Kjartan T. Eie	 (Writer's signature)
Faculty supervisor: Prof. Muk Chen Ong Marek Jan Janocha	
Thesis title: Numerical Simulations of Near-Wall Vortex-Induced Vibrations of two Circular Cylinders in Tandem	
Credits (ECTS): 30	
Key words: Vortex shedding, CFD, OpenFOAM, vortex-induced vibration, near-wall, tandem cylinder, turbulent flow, URANS, high Reynolds number	Pages: 79 + enclosure: 12 Stavanger, June 15, 2019 Date/year

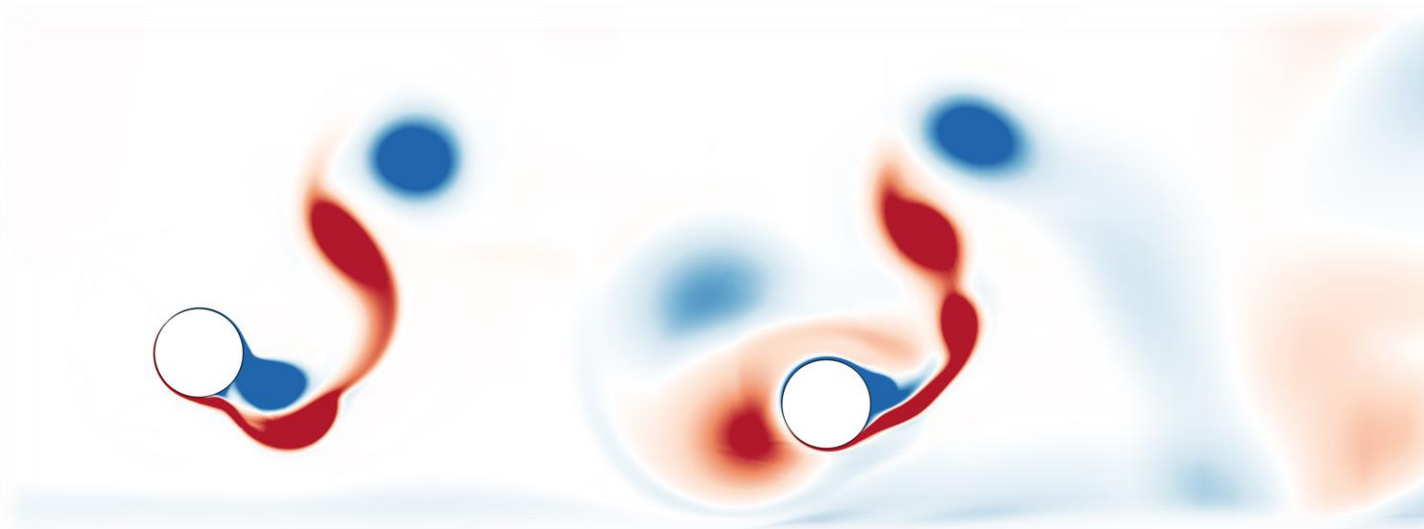
Numerical Simulations of Near-Wall Vortex-Induced Vibrations of two Circular Cylinders in Tandem

Author:
Kjartan Tjøstheim Eie

Supervisor:
Prof. Muk Chen Ong
Co-supervisor:
Marek Jan Janocha

UNIVERSITY OF STAVANGER

Master of Science Thesis, Marine- and Offshore Technology, Spring 2019
Department of Mechanical and Structural Engineering and Materials Science



To my Father

ABSTRACT

Free-spanning subsea pipelines may experience vortex-induced vibrations (VIV) when exposed to fluid flow. These resonant motions can cause fatigue-related problems and in some cases failure of the pipe. A common configuration is to have two pipelines laid next to each other. This further complicates the dynamic response, as the downstream pipeline is affected by the flow-interference induced by the upstream pipe. Two cylinders in tandem arrangement in the vicinity of a horizontal plane wall have been investigated numerically using 2D Unsteady Reynolds-Averaged Navier-Stokes (URANS) equations with a $k - \omega$ SST turbulence model. The cylinders are modelled as elastically supported with two-degrees-of-freedom (2DoF) which allow for both transverse and inline vibrations. Based on the cylinder diameter, D , the Reynolds number investigated in the present study is $Re = 3.6 \times 10^6$, corresponding to the transcritical flow regime. The effects of three main parameters are investigated; (i) gap ratio, G^* , is the gap distance from the horizontal boundary to the cylinder surface, (ii) cylinder spacing, L^* , is the horizontal surface-to-surface distance of the tandem cylinders (iii) reduced velocity, U_r , is the ratio of flow velocity to vibration frequency and diameter. Numerical simulations are performed for $U_r = \{4, 5\}$, $G^* = \{1.5, 2\}$, $L^* = \{4, 5, 6\}$ using the open source CFD code OpenFOAM. The mass ratio is set to $m^* = 10$, damping ratio to $\zeta = 0$, and boundary layer thickness $\delta/D = 0.48$. The model is validated against similar published studies. The single static cylinder model is in a good agreement with similar numerical studies. The model is modified to include a second downstream cylinder and allow for 2DoF vibrations. A second mesh sensitivity study is performed to determine the appropriate mesh density for the tandem case. Hydrodynamic forces, response amplitudes, motion trajectories, flow fields and frequency power spectra for displacements and hydrodynamic coefficients are analyzed and presented with respect to the parameter matrix defined in the study.

ACKNOWLEDGEMENTS

I would like to thank Prof. Muk Chen Ong for his continuous support and motivation throughout this thesis. His encouragement and his dedication are beyond comparison. Prof. Ong has been indispensable in his role both as academic, and administrative supervisor.

I would also like to express my deepest gratitude towards my co-supervisor, Marek Jan Janocha. Marek has been my mentor for the better part of a year and has always assisted me with any questions or issues I might have had, however ludicrous my queries might have been. He is truly devoted to his work in CFD, and I would like to wish him all the best in his Ph.D. study.

To my dear colleagues at the office, Bjørnar Nitter and Martin Andersen, I wish to extend a heartfelt thank you for the good times we have spent together. Our conversations and discussions have been paramount for my personal understanding of the complex aspects of CFD. I wish you both the very best in the times to come, both personally and professionally.

Lastly, I would like to thank my girlfriend for her endless patience and support. Bits and pieces.

TABLE OF CONTENTS

ABSTRACT	V
ACKNOWLEDGEMENTS	VI
TABLE OF CONTENTS	VII
LIST OF FIGURES	X
LIST OF TABLES	XIII
ABBREVIATIONS.....	XIV
LIST OF SYMBOLS	XV
1 INTRODUCTION	1
1.1 Background and motivation	1
1.2 Scope and outline of thesis.....	1
1.3 Previous work.....	3
1.3.1 Experimental studies.....	3
1.3.2 Numerical studies	7
2 FLOW AROUND CYLINDERS AND VORTEX-INDUCED VIBRATIONS	10
2.1 Flow regimes	10
2.2 Boundary layer concept.....	12
2.2.1 Flow separation.....	14
2.2.2 Turbulent boundary layer equations	14
2.3 Turbulent flow.....	16
2.4 Vortex shedding	16
2.4.1 Vortex shedding frequency.....	17
2.4.2 Vortex shedding pattern.....	18
2.5 Tandem cylinders	19
2.6 Surface roughness	20

2.7	Wall proximity	21
2.8	Hydrodynamic force.....	22
2.8.1	Drag and lift coefficients	23
2.9	Equation of motion.....	24
2.9.1	Two-degree-of-freedom system	25
2.10	Vortex-induced vibrations.....	25
2.10.1	Reduced velocity	26
2.10.2	Mass ratio	26
2.10.3	Displacement amplitude ratio	26
2.10.4	Lock-in phenomenon.....	27
3	COMPUTATIONAL FLUID DYNAMICS.....	30
3.1	Introduction	30
3.2	OpenFOAM.....	30
3.3	Governing equations	32
3.3.1	Continuity	32
3.3.2	Momentum.....	33
3.3.3	Navier-Stokes equations	34
3.4	Finite Volume Method	34
3.4.1	Spatial discretization.....	35
3.4.2	Temporal discretization	36
3.4.3	Equation discretization	37
3.5	PIMPLE algorithm	38
3.6	Turbulence modelling	39
3.6.1	Unsteady Reynolds-averaged Navier-Stokes (URANS)	39
3.6.2	$k - \omega$ SST Turbulence Model.....	40
3.6.3	Blended wall function.....	41
4	STATIC CYLINDER IN WALL PROXIMITY.....	42
4.1	Grid generation.....	42
4.2	Model description.....	43

4.3	Convergence study	45
4.4	Model validation	47
5	VORTEX-INDUCED VIBRATIONS OF TANDEM CYLINDERS	49
5.1	Grid generation.....	49
5.2	Model description.....	49
5.3	Convergence study	50
6	RESULTS AND DISCUSSION	53
6.1	Hydrodynamic forces	53
6.2	Response amplitudes	57
6.3	Motion trajectories	60
6.4	Flow fields.....	64
6.5	Vibration frequency.....	70
7	CONCLUSIONS AND RECOMMENDATIONS.....	72
7.1	Conclusions	72
7.2	Further work.....	74
	REFERENCES	75
	APPENDIX A: TIMESERIES OF HYDRODYNAMIC COEFFICIENTS	
	APPENDIX B: MOTION TRAJECTORIES	
	APPENDIX C: FREQUENCY POWER SPECTRA	

LIST OF FIGURES

Figure 1.1: Test matrix diagram.....	2
Figure 2.1: Flow around a cylinder.....	10
Figure 2.2: Transition from laminar to turbulent boundary layer.....	13
Figure 2.3: Comparison of viscous sublayer, log-law layer and experimental velocity profiles.	15
Figure 2.4: Vortex shedding principle	17
Figure 2.5: Strouhal number at different Reynolds number	18
Figure 2.6: Tandem flow regimes.....	20
Figure 2.7: Strouhal number at different Reynolds for different surface roughness parameters	20
Figure 2.8: Pressure distribution at different wall gap ratios.....	22
Figure 2.9: Drag and lift force of a cylinder in flow.....	23
Figure 2.10: Pressure distribution on cylinder surface for a cycle of vortex shedding.	23
Figure 2.11: Crossflow response of a submerged cylinder.....	27
Figure 2.12: Dependence between displacement amplitude ratio and reduced velocity for a submerged cylinder	28
Figure 2.13: Low mass system amplitude response diagram	28
Figure 3.1: Overview of OpenFOAM structure.....	31
Figure 3.2: Example OpenFOAM directory hierarchy.	31
Figure 3.3: Mass-flow in and out of fluid element	33
Figure 3.4: Example control volume	35
Figure 3.5: Structured (top) and unstructured (bottom) meshes.....	36
Figure 3.6: Trapezoidal rule applied in Crank-Nicolson numerical integration scheme.....	37
Figure 3.7: Flowchart of PIMPLE solver.	38
Figure 3.8: Reynolds decomposition of a turbulent velocity signal.	40
Figure 4.1: Mesh of tandem cylinders.	42
Figure 4.2: Upstream cylinder and close-up of radial cell distribution.	43
Figure 4.3: Schematic of computational domain for single static cylinder, given in terms of cylindrical diameter, D	43
Figure 5.1: Schematic of the computational domain for tandem cylinder setup.	49

Figure 6.1: a) CD and b) CL_{rms} for up- and downstream cylinders at $G^* = \{1.5, 2\}$ and $Ur = \{4, 5\}$ for cylinder spacing $L^* = 4$.	54
Figure 6.2: CD at $Ur = 5$ for up- and downstream cylinders at different cylinder spacing and gap ratio.	55
Figure 6.3: CL, UC for different gap ratios.	55
Figure 6.4: Hydrodynamic coefficients and displacements for upstream cylinder at $\tau = [0, 300]$, $Ur = 5$, $G^* = 1.5$, $L^* = 4$. Periods of large CL spikes are highlighted.	56
Figure 6.5: Hydrodynamic coefficients and displacements for upstream cylinder at $\tau = [100, 170]$, $Ur = 5$, $G^* = 1.5$, $L^* = 4$. Transition from large spikes in CL to a more regular pattern and corresponding reset of streamwise oscillation amplitude.	56
Figure 6.6: a) $AY, maxUC/D$ and b) $AY, maxDC/D$ for different gap ratios.	57
Figure 6.7: a) $AY, maxUC/D$ and b) $AY, maxDC/D$ with respect to cylinder spacing, L^* .	58
Figure 6.8: a) $AX, maxUC/D$ and b) $AX, maxDC/D$ for different gap ratios.	59
Figure 6.9: a) $AX, maxUC/D$ and b) $AX, maxDC/D$ for different reduced velocity.	59
Figure 6.10: a) $AX, rmsUC/D$ and b) $AX, rmsDC/D$ for different gap ratios.	60
Figure 6.11: $AX, rmsDC/D$ for different cylinder spacing.	60
Figure 6.12: Probability density plots of cylinder positions at $Ur = 4$, $G^* = 2$, $L^* = 4$ for a) upstream cylinder, and b) downstream cylinder.	61
Figure 6.13: Motion trajectories in the $X - Y$ plane for cylinder spacing $L^* = [4, 5, 6]$ at $\tau = [50, 150]$ for $Ur = 4$, $G^* = 2$.	62
Figure 6.14: Motion trajectories in the $X - Y$ plane for cylinder spacing $L^* = [4, 5, 6]$ at $\tau = [50, 150]$ for $Ur = 5$, $G^* = 2$.	63
Figure 6.15: Probability density plots of cylinder positions for a) $Ur = 5, G^* = 2, L^* = 5$ and b) $Ur = 5, G^* = 2, L^* = 6$.	64
Figure 6.16: Vorticity and pressure contour plots for a vortex shedding cycle at $Ur = 4$, $G^* = 1.5$ and $L^* = 5$. Upstream cylinder is approximately π ahead in phase.	66
Figure 6.17: Vorticity contour plots at $Ur = 4$, $G^* = 2$ and $L^* = 6$ in which vortices shed upstream impinge the downstream cylinder. Cylinders are in-phase.	67
Figure 6.18: Upstream hydrodynamic coefficients and response amplitudes for a period of vortex shedding. Vertical dotted lines A-D are timesteps corresponding to Figure 6.17.	68

Figure 6.19: Downstream hydrodynamic coefficients and response amplitudes for a period of vortex shedding. Vertical dotted lines a-d are timesteps corresponding to Figure 6.17.....68

Figure 6.20: Vorticity contour plots at $Ur = 4$, $G^* = 2$ and $L^* = 5$. The upstream cylinder displacement phase is lagging by approximately $\pi/2$69

Figure 6.21: Frequency power spectra of hydrodynamic coefficients and displacements for upstream (a)) and downstream (b)) cylinder at $Ur = 5$, $G^* = 1.5$ and $L^* = 5$...70

Figure 6.22: Frequency power spectra of hydrodynamic coefficients and displacements for upstream (a)) and downstream (b)) cylinder at $Ur = 4$, $G^* = 1.5$ and $L^* = 5$...71

LIST OF TABLES

Table 2.1: Flow regimes around a cylinder in steady current.....	11
Table 2.2: Some different vortex shedding patterns	19
Table 4.1: Parameters of convergence study meshes for single static cylinder.....	46
Table 4.2: Convergence study: single static cylinder, effects of mesh density. Simulated at Reynolds number 3.6×10^6 and gap ratio $G^* = 1$	47
Table 4.3: Model validation: numerical results of present study and similar works in the upper transition regime.	47
Table 5.1: Dimensionless parameters applied for convergence study of VIV for 2DoF tandem cylinders.....	50
Table 5.2: Parameters of convergence study meshes for 2DoF tandem cylinders.	51
Table 5.3: Convergence study: Upstream 2DoF cylinder, effects of mesh density. Simulated at Reynolds number 3.6×10^6 , gap ratio $G^* = 2$, and cylinder spacing $L^* = 4$	51
Table 5.4: Convergence study: Downstream 2DoF cylinder, effects of mesh density. Simulated at Reynolds number 3.6×10^6 , gap ratio $G^* = 2$, and cylinder spacing $L^* = 4$	51
Table 6.1: Mean drag and RMS lift coefficients for $Ur = \{4, 5\}$, $G^* = \{1.5, 2\}$ and $L^* = \{4, 5, 6\}$	53
Table 6.2: Maximum response amplitudes for both transverse ($AY, max/D$) and streamwise ($AX, max/D$) vibrations and inline RMS response ($AX, rms/D$).....	59

ABBREVIATIONS

2D	Two-dimensional
CFD	Computational Fluid Dynamics
CF	Crossflow
DC	Downstream Cylinder
DoF	Degree-of-Freedom
DNS	Direct Numerical Simulation
DNV	Det Norske Veritas
FIV	Flow-Induced Vibrations
FVM	Finite Volume Method
GUI	Global User-Interface
IL	In-line
LES	Large Eddy Simulation
PISO	Pressure-Implicit with Splitting of Operators
PIV	Particle Imaging Velocimetry
RANS	Reynolds-Averaged Navier-Stokes
RMS	Root-mean-square
SIMPLE	Semi-Implicit Method for Pressure Linked Equations
SST	Shear Stress Transport
UC	Upstream Cylinder
URANS	Unsteady Reynolds-Averaged Navier-Stokes
VIV	Vortex-Induced Vibrations
WIV	Wake-Induced Vibrations

LIST OF SYMBOLS

Roman symbols

A	Amplitude of vibration
c	Damping coefficient
C_D	Drag coefficient
C_L	Lift coefficient
Co	Courant number
D	Diameter/characteristic length
e	Gap distance
F_D	Drag force
F_L	Lift force
f_n	Natural frequency
f_{osc}	Oscillation frequency
f_v	Vortex-shedding frequency
G^*	Gap ratio
k	Spring stiffness
L	Cylinder gap
L^*	Cylinder spacing ratio
m	Mass
m^*	Mass ratio
m_a	Added mass
p	Pressure
Re	Reynolds number

St	Strouhal number
U, U_∞	Freestream velocity
U^+	Non-dimensional velocity
U_r	Reduced velocity
u	Velocity x-component
v	Velocity y-component
w	Velocity z-component
X	Streamwise direction
y^+	Non-dimensional wall distance
Y	Transverse direction

Greek symbols

δ	Boundary layer thickness
κ	von Kármán constant
μ	Dynamic viscosity
ν	Kinematic viscosity
ϕ	Transport equation variable/angle from stagnation to separation point
ρ	Density
τ	Dimensionless time/shear stress
ζ	Damping ratio

1 INTRODUCTION

1.1 Background and motivation

Subsea pipelines are not always fixed to the bottom of the seabed. Free spans can exist as a result of scour, at pipeline crossings or due to uneven seabed. The length of free spanning pipe can range from only a few times the pipe diameter to hundreds, with a typical seabed clearance of almost zero to about two- or threefold pipeline diameter. When free spanning pipelines are exposed to fluid flow, they may experience flow induced motions as a result of alternating vortex shedding in the cylinder wake. The dynamic motions are referred to as vortex-induced vibrations (VIV), and can cause fatigue-related failures. There have been incidents with subsea pipelines floating to the surface after losing their concrete casing as a result of flow-induced motions. A recommended practice for the handling of free spanning pipelines is provided by Det Norske Veritas (DNV GL, 2017). DNV suggests that computational fluid dynamics (CFD) can be used as one of the tools for VIV assessment of subsea pipelines. However, a note is made on the knowledge gap and further efforts required to establish appropriate guidelines for CFD simulations of VIV. In the present thesis, a numerical approach is selected to study the dynamic motions of two cylindrical pipelines in a tandem arrangement close to the seabed. An advantage of a numerical study is the ease of adjusting simulation parameters once a numerical model is established. A parametric study allows for a detailed investigation of influencing parameters for the complex VIV dynamics. The model validation study will strengthen the reliability of CFD as a tool for predicting flow field characteristics and hydrodynamics. Further model development will provide insight into a field of the science in which very limited research has been conducted thus far.

1.2 Scope and outline of thesis

The main scope of the thesis is to numerically investigate the 2D VIV characteristics of two circular cylinders with two degrees-of-freedom (2DoF) in a tandem arrangement in the close proximity of a horizontal plane wall, at very high Reynolds number. The fluid flow fields are solved using the opensource software OpenFOAM (Open Field Operation and Manipulation) based on the finite-volume method (FVM). First, a numerical model is built and validated against similar numerical studies. Second, the model is modified according to the simulation

parameters of interest. Third, results and postprocessing of flow fields and characteristics are presented.

Three main parameters are investigated. U_r is the reduced velocity which is the normalized ratio of flow velocity to vibration frequency, defined as $U_r = U/f_n D$ (where U is the free stream velocity, f_n is the natural frequency of the cylinder and D is the diameter), G^* is the gap ratio distance to the cylinders from the wall, defined as $G^* = e/D$ (where e is the gap distance from the wall to cylinder surface), and L^* is the gap ratio distance between the two cylinders, defined as $L^* = L/D$ (where L is the surface-to-surface gap distance between the cylinders). A test matrix of investigated parameters is presented in Figure 1.1.

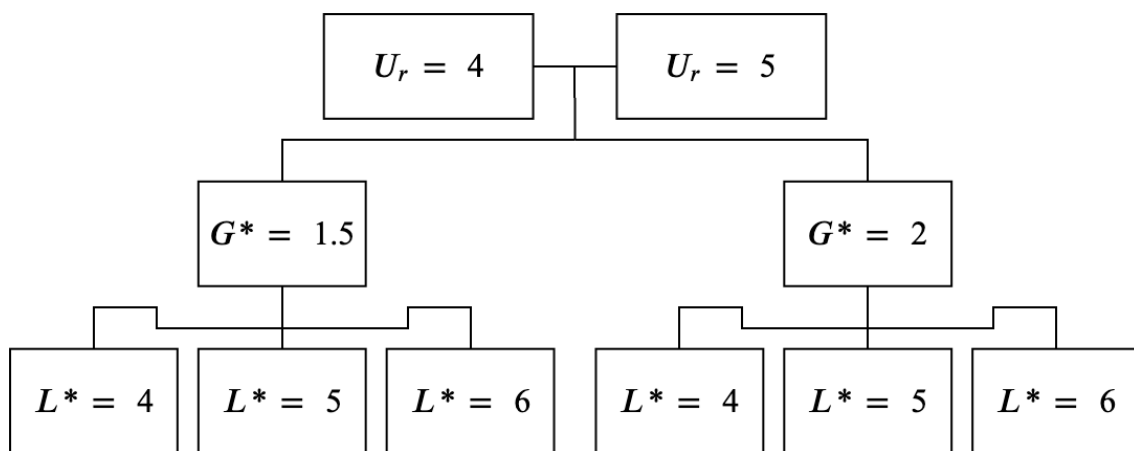


Figure 1.1: Test matrix diagram.

The outline of the thesis can be summarized as follows:

Chapter 1: The general background and motivation of the study is introduced, and the scope and outline are defined. A summary of previous work is presented.

Chapter 2: The general theory of flow around cylindrical structures and VIV mechanics are presented.

Chapter 3: An overview of the applied computational methods is presented. The Finite Volume Method and turbulence modelling is reviewed.

Chapter 4: Presents the results from the convergence and model validation study of a single static cylinder.

Chapter 5: Presents the results from the convergence study of two near-wall 2DoF cylinders in tandem.

Chapter 6: Results of simulations are presented. Hydrodynamic properties, vibration amplitudes, motion trajectories, frequency power spectra, phase plots, and flow fields are investigated.

Chapter 7: A summary of the most important observations and suggestions for further work is given.

1.3 Previous work

Vortex-induced vibration (VIV) of isolated, elastically mounted cylinders has been subject to extensive studies (e.g. Sarpkaya, 2004; Bearman, 2011; Williamson and Govardhan 2004, 2008). Flow around cylinders and flow-induced vibrations (FIV) were studied in the works of Sumer and Fredsøe (2006), Sarpkaya (2010) and Blevins (1990). Some of the earliest VIV experiments are those conducted by Feng (1968). Feng (1968) showed that for a range of reduced velocity $U_r = U/f_n D$, (where U is the freestream velocity, f_n is the natural frequency of the cylinder, and D is the diameter) the cylindrical body experienced resonant responses when the oscillation frequency coincided with the vortex shedding frequency, thus confirming the onset of VIV. VIV is often studied by investigating the transverse motion of a single cylinder in freestream. In the present study, the cylinders are free to vibrate in both transverse and in-line directions. The difference in response when allowing a second degree-of-motion is discussed in Moe and Wu (1990), Sarpkaya (1995) and Jauvits and Williamson (2003). In the present chapter, we will take a deeper look at the work that has been done with regards to the effect of wall proximity, and flow around two tandem cylinders.

1.3.1 Experimental studies

Early studies of the effect of wall proximity on the flow around cylinders were performed by Bearman and Zdravkovich (1978). In their wind tunnel experiments at Reynolds number $Re = 2.5 \times 10^4$ and $Re = 4.8 \times 10^4$, ($Re = UD/\nu$, where U is the freestream velocity, D is the characteristic length (diameter for cylinders) and ν is the kinematic viscosity of the fluid) Bearman and Zdravkovich (1978) observed a suppression of the vortex shedding for gap ratios smaller than $G^* = 0.3$, where $G^* = e/D$ (e is the gap distance from the wall, and D is the diameter of the cylinder). Jacobsen et al. (1984) found that cross-flow vibration amplitudes were reduced at $G^* = 0.5$ compared to $G^* = 1.0$, at Reynolds number in the range of

$0.5 \times 10^5 < Re < 1.7 \times 10^5$. At very small gaps no vortex shedding was observed, but vibrations were still present. The vortex shedding frequency lock-in was demonstrated by Anand and Tørum (1985) by transverse free span vibration experiments of submarine pipelines in steady and wave-induced flow. Anand and Tørum (1985) showed that both the maximum magnitude of mean drag coefficient and the maximum amplitude of transverse vibration shifts towards a higher reduced velocity, U_r , when gap ratio, G^* , is decreased. Zdravkovich (1985) continued to perform wind tunnel experiments and investigated drag and lift force in conjunction with gap ratio and boundary layer thickness δ . The parameter ranges used were $4.8 \times 10^4 < Re < 3 \times 10^5$, $0 < G^* < 2$, and $0.12 < \delta/D < 0.97$. Zdravkovich (1985) found that the lift coefficient is governed by G^* , while the drag coefficient is dominated by the ratio of gap thickness of the boundary layer, G/δ . Fredsøe et al. (1987) investigated transverse vibrations of a cylinder at gap ratios between zero and unity. Fredsøe et al. (1987) suggested that vibrations at very small gap ratios are partly vortex-induced vibrations and partly self-excited vibrations. For $U_r < 3$ vibration frequency was found to be close to vortex shedding frequency for a stationary cylinder. For $3 \leq U_r \leq 8$ vibration frequency was significantly larger than vortex shedding frequency. At Reynolds number range $1.30 \times 10^4 < Re < 1.45 \times 10^4$, Lei et al. (1999) investigated the effects of bed proximity, thickness of boundary layer, hydrodynamic forces and vortex shedding behavior of a stationary smooth cylinder using wind tunnel experiments. Variation in the root-mean-square (RMS) value of the lift coefficient was used to detect the onset or suppression of vortex shedding. A critical gap ratio, G_c^* , at which vortex shedding is suppressed, was found to be in the range of $G^* = 0.2 - 0.3$ depending on the thickness of the boundary layer. Yang et al. (2009) studied vortex-induced vibrations of a cylinder near a rigid plane in a flume at sub-critical Reynolds number. The parameters under investigation were reduced velocity, U_r , gap ratio, G^* , stability parameter, $K_s = 4(m + m_a)\zeta/\pi\rho D^2$ (where m and m_a is mass and added mass, respectively, and ζ is the structural damping factor of the cylinder) and mass ratio, $m^* = 4m/\pi\rho D^2$. Amplitude response was in good agreement with that of Fredsøe et al. (1987) and Jacobsen et al. (1984) for larger gap ratios. However, some discrepancies were found at gap ratios of 0.2 or less. The process of increasing-maximum decreasing-variation of transverse vibration amplitudes with increasing reduced velocity was identified. In the case of increasing gap ratio, G^* , the amplitude ratio was also increasing. The frequency ratio, f/f_n (f is the vibration frequency and f_n is the natural frequency of the cylinder), was much larger for small gap ratios ($G^* < 0.3$). Width of lock-in range and frequency ratio was increasing with decreasing mass ratio, m^* . Wang et al.

(2013) investigated VIV of a neutrally buoyant cylinder in wall proximity. At Reynolds numbers ranging from $Re = 3 \times 10^3$ to $Re = 1.3 \times 10^4$, flow around a cylinder with mass ratio $m^* = 1.0$, damping ratio $\zeta = 0.0173$ and variations of gap ratio ($0.05 < G^* < 2.5$) and reduced velocity ($1.53 < U_r < 6.62$) was captured using particle image velocimetry (PIV) as well as direct drag force measurements by a piezoelectric load cell. In contrast to the case of a stationary cylinder, at which vortex shedding is suppressed at gap ratios of $0.2 \sim 0.3$ (Bearman and Zdravkovich (1978), Lei et al., (1999)), vibrations were found even at very small gap ratios ($G^* = 0.05$), similar to the observations made by Jacobsen et al. (1984). Fu et al. (2014) performed VIV experiments on cylinders at high Reynolds numbers ($Re = 2 \times 10^5$) and found the lock-in range to occur at a higher non-dimensional frequency when in proximity to a wall. At a gap ratio $G^* = 0.1$, vortex shedding was completely suppressed. In Daneshvar and Morton's (2017) VIV experiments, little influence of wall proximity was found at gap ratios larger than $G^* = 3$. At smaller gap ratios ($G^* < 0.5$) the cylinder began to periodically impact the wall.

Zdravkovich (1977) performed an extensive review of studies on flow interference between two circular cylinders in different arrangements. For the tandem arrangement, Zdravkovich (1977) investigated force measurements, pressure distributions, velocity profiles, vortex shedding, drag, and Reynolds number effects. Igarashi (1982) studied flow characteristics around two circular cylinders with diameter ratio $D_2/D_1 = 0.68$ in tandem, at $1.3 \times 10^4 \leq Re \leq 5.8 \times 10^4$ and cylinder spacing $0.9 \leq L/D_1 \leq 4.0$ (L is the gap distance between the cylinders). His wind tunnel experiments confirmed the reattachment of a separated shear layer from the first cylinder and bistable flow at the critical region ($1.9 < L/D_1 < 2.1$) was found similar for both different and equal diameter cylinders. In his study of flow interference between circular cylinders in cross-flow, Zdravkovich (1987) suggested that the flow could be classified into three characteristic types, depending on cylinder spacing ratio ($L^* = L/D$): a single bluff-body regime at $1 \leq L^* \leq 1.2 \sim 1.8$ in which the von Kármán street is only observed in the wake of the downstream cylinder. A re-attachment regime ($1.2 \sim 1.8 \leq L^* \leq 3.4 \sim 3.8$) where free shear layers emanating from the upstream cylinder reattach to the downstream cylinder, still featuring only a single von Kármán street, and lastly, an impingement regime ($L^* > 3.4 \sim 3.8$) in which normal vortex shedding occurs behind the upstream cylinder, and the convected vortices periodically impinge on the downstream cylinder. Bokaian and Geoola (1984) investigated wake-induced galloping of two interfering cylinders using a setup with a fixed upstream cylinder and a downstream cylinder free to oscillate laterally supported by

linear springs. The downstream cylinder exhibited vortex-resonance, galloping, or a combination of both, depending on the distance between cylinders and the structural damping. Similar to the works of Bokaian and Geoola (1984), Brika and Laneville (1999) performed experiments with a fixed upstream and oscillating downstream cylinder, at cylinder spacing $7 \leq L^* \leq 25$ and $5 \times 10^3 \leq Re \leq 27 \times 10^3$. The onset of lock-in for the downstream cylinder occurred at a higher reduced velocity, U_r , than that of a single cylinder, and the lock-in range was wider. Kim et al. (2009) investigated flow-induced vibrations of tandem cylinders for three different setups; fixed upstream and transverse vibrating downstream cylinder, fixed downstream and transverse vibrating upstream cylinder, and both cylinders allowed to vibrate. They classified five different vibration regimes based on vibration characteristics. In Regime V ($L^* \geq 2.7$) vortices are observed in the flow region between the cylinders. Both cylinders are vibrating in this regime, with the downstream cylinder vibrating at a significantly higher amplitude. Assi et al. (2006, 2010, 2013) performed various experiments with vibrating tandem cylinders, investigating flow-induced interference, vortex interaction excitation mechanism, and wake stiffness effect. Assi et al. (2006) visualized the flow at $3 \times 10^3 \leq Re \leq 13 \times 10^3$ and $U_r \leq 12$ using PIV. With fixed upstream and vibrating downstream cylinder, galloping effects were observed on the trailing cylinder for $2 \leq L^* \leq 5.6$. In Assi et al. (2010) wake-induced vibrations (WIV) is characterized as a build-up of amplitude persisting to high reduced velocities, differing from VIV which occurs at a limited resonance range. It was suggested that WIV of the trailing cylinder was excited by the unsteady interactions between upstream cylinder vortices and downstream cylinder. In Assi et al. (2013) the concept of wake stiffness was introduced as a parameter that can be approximated to a linear spring with stiffness proportional to Reynolds number and lift force. It was concluded that the wake stiffness parameter could be used to characterize the WIV response. Wang et al. (2013) investigated the influence of wall proximity on the flow around fixed tandem cylinders. Experimental parameters were $Re = 6.3 \times 10^3$, $1.5 \leq L^* \leq 6$ and $0.15 \leq G^* \leq 2$, and flow fields and dynamic forces were captured using PIV and load cells, respectively. Vortex shedding suppression was observed for $G^* < 0.3$. In the $0.3 \leq G^* \leq 1$ range vortex shedding occurs but is asymmetric due to the influence of wall proximity. At larger gaps ($G^* > 1$) wall influence was considered negligible. Three regimes based on the distance between the cylinders were identified, namely the extended-body regime ($1 \leq L^* \leq 2$), the reattachment regime ($2 < L^* \leq 4$) and the impinging regime ($L^* > 4$).

1.3.2 Numerical studies

Ong et al. (2010) applied a standard high Reynolds number $k - \epsilon$ turbulence model to numerically simulate flow around a fixed circular cylinder close to a flat seabed. Gap ratio, G^* , boundary layer thickness, δ , and seabed roughness, z_w , at very high Reynolds number ($Re = 3.6 \times 10^6$), were investigated. For small G^* , the time-averaged drag coefficient (\bar{C}_D) was increasing with an increasing gap ratio. \bar{C}_D approached a maximum value at a certain G^* , and then decreased towards a constant value. For very small gap ratio ($G^* = 0.1$), the positive zone of the pressure coefficient, C_p , was skewed upstream, yielding upward lift. The onset of vortex shedding occurred at $G^* = 0.25$, at which suction at the gap became large, and the cylinder experienced negative lift. At larger gaps, C_p became symmetric and mean lift approached zero. Chung (2016) simulated transverse vibrations at $Re = 100$, and studied responses at $G^* = 0.06, 0.30$. Chung (2016) found an increasing lock-in range and decreasing maximum vibration amplitudes with decreasing gap ratio. Vibration amplitude peaks occurred at higher U_r for smaller gap ratios. Two-degree-of-freedom (2DoF) VIV simulations were conducted by Zhao and Cheng (2011) and Tham et al. (2015). The former study revealed vortex-induced vibrations for gap ratio as low as $G^* = 0.002$ using a $k - \epsilon$ turbulence model. The latter 2DoF study was conducted with $Re_D = 100$, and $Re_L = 2900$ (where Re_D and Re_L denote Reynolds numbers based on cylinder diameter and upstream distance, respectively) for gap ratios $0.5 \leq G^* \leq 10$, and reduced velocities $2 \leq U_r \leq 10$. Decreasing G^* revealed an increasing lock-in region. Vibration frequency in the lock-in range was decreasing with decreasing G^* . Both initial and lower amplitude branches were observed for $G^* \geq 0.75$, whilst for $G^* \leq 0.6$ a third amplitude branch – the upper branch, was developed. For cases with $G^* > 5$ the effect of wall proximity disappeared. Enhanced streamwise oscillations near the wall were explained based on phase difference curves between drag force and streamwise displacement that yielded a net power transfer in the in-line direction.

There are very few experimental studies investigating tandem cylinders in wall proximity. However, several numerical works have been devoted to this subject. Bhattacharyya and Dhinakaran (2008) investigated vortex shedding for tandem square cylinders near a plane wall. Rao et al. (2013) investigated the wake stability behind tandem cylinders sliding along a wall at $20 \leq Re \leq 200$ and separation distances of $0.1 \leq L^* \leq 10$. Tang et al. (2015) numerically investigated flow past fixed tandem cylinders in close-wall proximity at $Re = 200$, for $0.25 \leq G^* \leq 2.0$ and $1 \leq L^* \leq 4$. For $G^* < 0.25$ suppression of vortex shedding was observed, and

RMS values of drag and lift for both cylinders were almost zero. With sufficient separation distance, vortex shedding occurred for both cylinders. Drag coefficient increased with G^* for values of $G^* \leq 1.5$. At $G^* = 1.5$ and 2.0 , mean drag values were similar in magnitude, suggesting negligible wall proximity effects for further increasing gaps. Downstream cylinder experienced negative drag coefficient for small L^* , and positive for large L^* . The change in sign of $\overline{C_D}$ occurred somewhere between $2 < L^* < 2.5$, depending on G^* . Abrahamsen Prsič et al. (2015) performed large eddy simulations (LES) of fixed tandem cylinders at $Re = 1.31 \times 10^4$, $G^* = 1$ and $L^* = 2$ and 5 . Abrahamsen Prsič et al. found the smaller separation length to be within the reattachment regime, and the larger to be within the co-shedding regime. At $L^* = 2$, wall proximity effects were potent, and the development of a von Kármán vortex street for either cylinder was inhibited. In D'Souza et al. (2016) the wall under the tandem cylinders was translating with the current, in an effort to remove wall boundary layer interactions. For $Re = 200$ and $G^* = 0.5$, an early transition from reattachment to co-shedding regime was observed. At gaps of $G^* \geq 1.5$ force coefficients approached their free-stream equivalents, with a negligible wall influence at around $G^* \geq 5$. An extension of the work of Abrahamsen Prsič et al. (2015) was performed by Li et al. (2018), at gaps ratios of $G^* = 0.1, 0.3$ and 0.5 . Findings included decreasing drag coefficient, $\overline{C_D}$, for upstream cylinder with decreasing gap ratio; negative drag coefficient for downstream cylinder at $L^* = 2$; a cavity-like flow between the cylinders at $L^* = 2$; and a recirculation zone in the wake of the downstream cylinder at $G^* = 0.1$.

Few studies have been conducted at very high Reynolds numbers. Catalano et al. (2004) used large-eddy simulations to observe the flow around a cylinder at $Re = 5 \times 10^5$ and 10^6 . Comparing with Reynolds-averaged Navier-Stokes (RANS) solutions and available experimental data, Catalano et al. (2004) found LES to be more accurate. However, less accurate results were documented with an increasing Reynolds number. Singh and Mittal (2005) investigated the possible relationship between the sudden drop of drag at $Re \sim 2 \times 10^5$ – known as the drag crisis – and separated shear layer instability in the flow past an isolated circular cylinder. Singh and Mittal (2005) performed LES at Reynolds numbers ranging from $Re = 100$ to $Re = 10^7$. Two-dimensional unsteady RANS (URANS) equations with a standard $k - \epsilon$ turbulence model was used to investigate the flow around a smooth cylinder at $Re = 1 \times 10^6, 2 \times 10^6$ and 3.6×10^6 in Ong et al. (2009). The study revealed that the $k - \epsilon$ model yields satisfactory results for engineering purposes at $Re > 10^6$.

Janocha (2018) investigated 2DoF near-wall VIV for piggyback cylinders at $Re = 200$ and $Re = 3.6 \times 10^6$ using the $k - \omega$ SST turbulence model with a wall function. For $Re = 3.6 \times 10^6$, a very good agreement with similar numerical studies was found for mean drag and pressure coefficient. However, RMS of lift coefficient and Strouhal number values were found to fall in the upper limit of the uncertainty band of experimental data. Lock-in range was observed for $3 \leq U_r \leq 8$, with a maximum transverse response at $U_r = 6$.

2 FLOW AROUND CYLINDERS AND VORTEX-INDUCED VIBRATIONS

The present chapter introduces the theoretical background of viscous flow around cylindrical structures and the mechanics and characteristic parameters of vortex-induced vibrations.

2.1 Flow regimes

When investigating the flow around cylinders, two flow regions are considered; the wake and the boundary layer (Figure 2.1). The boundary layer thickness (δ) is small compared to the cylinder diameter (D), which results in large velocity-gradient and significant shear stress. The wake starts at the separation point and extends over a distance downstream of the cylinder.

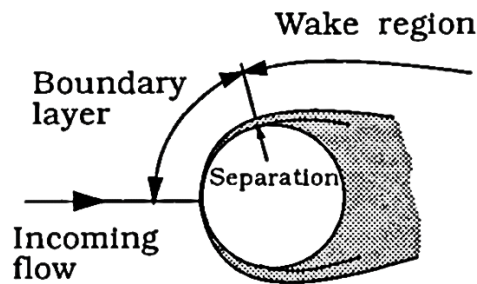


Figure 2.1: Flow around a cylinder (Sumer and Fredsøe, 2006, pp.3)





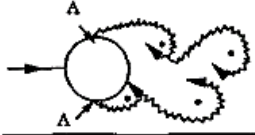
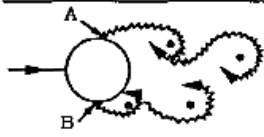
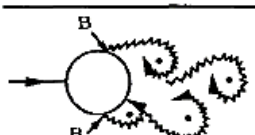
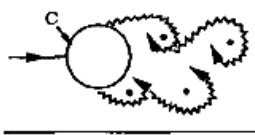

The flow behavior around an immersed cylinder is largely dependent on a dimensionless parameter known as the Reynolds number (Re), defined as:

$$Re = \frac{DU}{\nu} \quad (2.1)$$

where D is the characteristic length (for a cylinder this is the diameter), U is the flow velocity and $\nu = \mu/\rho$ is the kinematic viscosity of the fluid (μ [Ns/m^2] is the dynamic viscosity, and ρ [kg/m^3] is the density). Table 1 (Sumer and Fredsøe, 2006) summarizes different regimes with respect to Reynolds number. For very low Reynolds number ($Re < 5$) there is no separation of the flow – the flow is *creeping*. In the $5 < Re < 40$ range, two symmetric vortices start to form in the cylinder wake as a result of flow separation. A further increase of Reynolds number ($40 < Re < 200$) introduces a phenomenon known as *vortex shedding*. The vortices are being shed from alternating cylinder poles and form the laminar vortex street. A transition to turbulent vortices occurs in the $200 < Re < 300$ region. As Re increases,

turbulence transition occurs closer to the cylinder, with $Re = 400$ being the threshold for completely turbulent vortices. The next range is known as the *subcritical regime* and covers a large range of Reynolds number ($300 < Re < 3 \times 10^5$) in which the boundary layer remains laminar. Transition to turbulent boundary layer occurs for $3 \times 10^5 < Re < 3.5 \times 10^5$.

Table 2.1: Flow regimes around a cylinder in steady current (Sumer and Fredsøe, 2006, pp.2).

a)		No separation. Creeping flow	$Re < 5$
b)		A fixed pair of symmetric vortices	$5 < Re < 40$
c)		Laminar vortex street	$40 < Re < 200$
d)		Transition to turbulence in the wake	$200 < Re < 300$
e)		Wake completely turbulent. A: Laminar boundary layer separation	$300 < Re < 3 \times 10^5$ Subcritical
f)		A: Laminar boundary layer separation B: Turbulent boundary layer separation; but boundary layer laminar	$3 \times 10^5 < Re < 3.5 \times 10^5$ Critical (Lower transition)
g)		B: Turbulent boundary layer separation; the boundary layer partly laminar partly turbulent	$3.5 \times 10^5 < Re < 1.5 \times 10^6$ Supercritical
h)		C: Boundary layer com- pletely turbulent at one side	$1.5 \times 10^6 < Re < 4 \times 10^6$ Upper transition
i)		C: Boundary layer comple- tely turbulent at two sides	$4 \times 10^6 < Re$ Transcritical

The transition begins at the separation point and moves upstream towards the stagnation point with increasing Re . However, this only occurs on one side of the cylinder, occasionally switching to the other side, causing flow asymmetry and non-zero lift of the cylinder (Schewe,

1983). This is known as the critical flow regime. The critical regime is followed by the supercritical regime ($3.5 \times 10^5 < Re < 1.5 \times 10^6$) in which boundary layer separation is turbulent on both sides but has not yet transitioned fully upstream to the stagnation point. Similar to the critical flow regime, at $1.5 \times 10^6 < Re < 3.5 \times 10^6$, fully turbulent boundary layers are observed in this upper transitional regime, but only for one side of the cylinder. Finally, at $Re > 3.5 \times 10^6$ the boundary layer is fully turbulent across the surface of the cylinder. This is the transcritical regime.

2.2 Boundary layer concept

A well-known phenomenon of fluid flow is the *no-slip* condition – that is, at a solid surface the relative velocity between a fluid particle and the wall is zero. Prandtl (Çengel and Cimbala, 2017) hypothesized that by this adhesion of fluid to the wall, there exists a small transitional flow layer in which viscous effects has a strong influence on the flow velocity. This transitional layer from zero velocity, to the full magnitude at a distance δ from the wall, is known as the *boundary layer*. A consequence of non-negligible viscous effects is the inapplicability of potential flow equations, such as Euler and Bernoulli's. Prandtl's boundary layer equations for steady, two-dimensional flow (White, 2006) are:

$$\frac{\partial u}{\partial x} + \frac{\partial v}{\partial y} = 0 \quad (2.2)$$

$$u \frac{\partial u}{\partial x} + v \frac{\partial u}{\partial y} = U \frac{dU}{dx} + \nu \frac{\partial^2 u}{\partial y^2} \quad (2.3)$$

following the conditions that $u(x, 0) = v(x, 0) = 0$ and $u(x, \infty) = U(x)$, where u is the horizontal velocity component, v is the vertical velocity component and U is the freestream velocity. It should be noted that these equations are parabolic, meaning no flow information is passed from down- to upstream. Because of this, we do not need to specify any downstream boundary conditions – the downstream flow is governed by the boundary layer equations. These partial differential equations can be solved numerically using finite-difference techniques. Blasius a student of Ludwig Prandtl, showed that the equations can be reduced to ordinary differential equations by the use of similarity transformation (Çengel and Cimbala, 2017). By convention, the thickness of the boundary layer is defined as the distance from the wall surface to the point at which the velocity component parallel to the wall is 99% of freestream velocity. Blasius' solution for flow over a flat plate reads:

$$\frac{\delta_{99\%}}{x} = \frac{5.0}{\sqrt{Re_x}} \quad (2.4)$$

where δ is boundary layer thickness, x is position along the plate surface, and $Re_x = \rho Ux/\mu$ is the local Reynolds number.

From Equation 2.4 it is obvious that the boundary layer thickness for a flat plate decreases with increasing Re . However, this only holds true for a certain range of Reynolds number. Equations 2.2 and 2.3 apply to the *laminar* boundary layer. However, at a certain threshold value of local Re_x , small turbulent disturbances begin to occur in the flow, initiating a transition process towards a *turbulent* boundary layer. For a smooth flat plate, the transition phase begins at a critical Reynolds number, $Re_{x,critical} \cong 1 \times 10^5$, and reaches a fully turbulent boundary layer at $Re_{x,transition} \cong 3 \times 10^6$ (Çengel and Cimbala, 2017). In real-life applications, the turbulent transitions typically occur at lower Reynolds number values due to effects such as surface roughness, wall curvature, and free-stream disturbances.

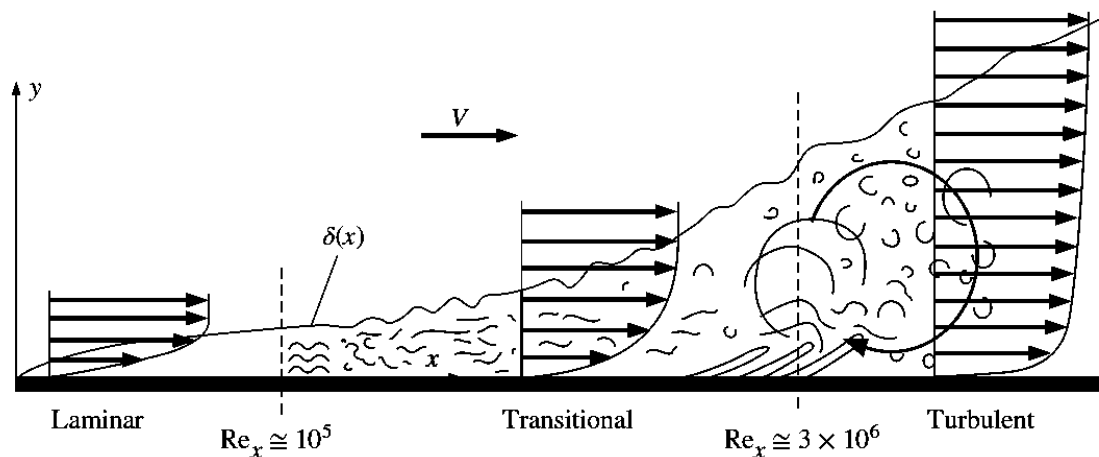


Figure 2.2: Transition from laminar to turbulent boundary layer (Çengel and Cimbala, 2017, pp. 562).

An engineering critical Reynolds number ($Re_{x,cr} = 5 \times 10^5$) is often employed as a predictive measure to whether the boundary layer is turbulent ($Re_x > Re_{x,cr}$) or laminar ($Re_x < Re_{x,cr}$). An illustration of the transition to turbulent boundary layer is shown in Figure 2.2. The transition notably increases the height of the boundary layer. The increasing δ at high Reynolds number contradicts Equation 2.4, and thus Blasius' equation is not applicable at $Re > Re_{x,critical}$.

2.2.1 Flow separation

In the case of flow around a cylinder, the boundary layer profile changes depending on its position (x) on the surface. At the back of the cylinder, the boundary layer may no longer stay attached to the surface. This is known as *flow separation*. The point at which flow separation takes place is known as the *separation point*. In laminar steady flow, the separation point is identified by zero shear stress ($\partial u/\partial y = 0$) and is a consequence of adverse (positive) pressure gradient. According to Bernoulli's momentum equations, adverse pressure gradient necessitates decreasing velocity;

$$U \frac{\partial U}{\partial x} = -\frac{1}{\rho} \frac{dp}{dx} \quad (2.5)$$

for steady, incompressible flow. Although it is not possible to postulate a general definition of when and where the separation point will occur, it is probable that separation will happen if positive pressure gradient acts long enough (Panton, 2013). We evaluate the boundary layer equation at the surface ($y = 0, u = v = 0$) and recognize the velocity term from Bernoulli's so that Equation 2.3 reduces to;

$$\frac{dp}{dx} = \mu \left. \frac{\partial^2 u}{\partial y^2} \right|_{wall} \quad (2.6)$$

For adverse pressure gradient, $\partial u/\partial y$ is positive. If $\tau \approx \partial u/\partial y$ is increasing outward from the surface, then it follows that there must exist a maximum value somewhere within the flow, since $\tau(y = \infty) \approx 0$. Furthermore, for the velocity profile, there will exist an inflection point at the position of maximum τ . As a result, there will be an area with reversed flow near the wall. At this stage, the flow is no longer governed by only upstream flow conditions and the boundary layer equations are no longer applicable, thus requiring the full Navier-Stokes equations (Section 3.3.3) to solve the field. It is noted that the separation point marks the location at which the boundary layer equations become inadequate.

2.2.2 Turbulent boundary layer equations

Special considerations are required when evaluating turbulent boundary layers. These layers exhibit different behavior depending on the distance from the wall, which can be described by implementing a composite understanding of the layer. An *inner layer* constitutes about 10 –

20% of the entire boundary layer thickness, while the *outer layer* contains the remaining 80 – 90%. Dimensionless variables are used in the analysis of turbulent boundary layers. The inner region, also known as the linear or viscous sub-layer, has a velocity profile that is linearly dependent on the non-dimensional wall distance;

$$U^+ = y^+ \quad (2.7)$$

where $U^+ = U/u_\tau$ is the non-dimensional velocity, and $y^+ = u_\tau y/\nu$ is the non-dimensional wall distance at length scale y from the wall, $u_\tau = \sqrt{\tau_w/\rho}$ is the shear velocity and $\tau_w = \mu \frac{\partial u}{\partial y}$ the shear stress at the wall. The viscous sublayer range is approximately $0 < y^+ < 5$. The layer outside the viscous sublayer is known as the log-law layer ($30 < y^+ < 500$). In this layer, both viscous and turbulent effects are of importance. If we assume the flow to be inviscid, U^+ logarithmic profile;

$$U^+ = \frac{1}{\kappa} \ln(y^+) + c \quad (2.8)$$

where $\kappa = 0.41$ is the von Kármán constant, and $c \approx 5.1$ is a function of roughness Reynolds number and roughness geometry. In the $5 < y^+ < 30$ range neither Equation 2.7 or Equation 2.8 are applicable. This range is of particular importance when modelling in CFD using turbulent wall functions. A comparison of velocity profiles and experimental data is presented in Figure 2.3.

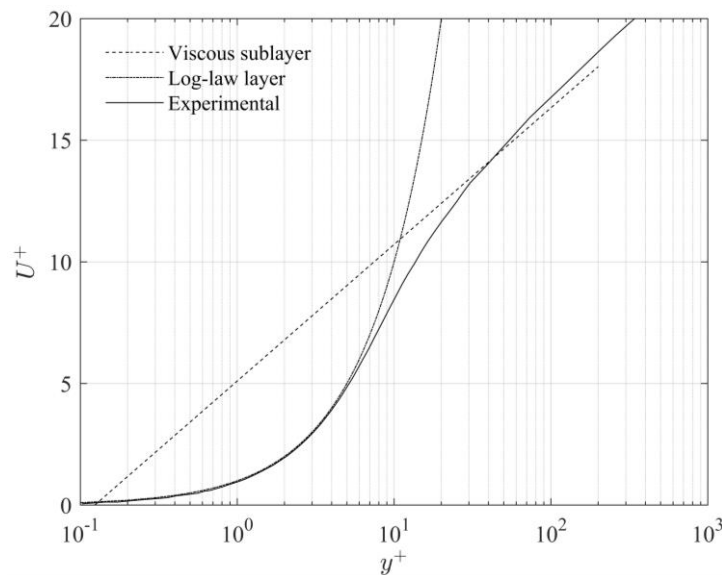


Figure 2.3: Comparison of viscous sublayer, log-law layer and experimental velocity profiles.

2.3 Turbulent flow

Turbulent flow is inherently chaotic. It is difficult to properly define, so in order to understand it, we will investigate the characteristic features that turbulent flows exhibit. Tennekes and Lumley (1972) listed the seven most important turbulence characteristics:

1. Irregularity. Turbulent flow is irregular, random and chaotic. Motions span across a range of different length-, velocity- and timescales. The largest motions are known as large eddies and contain some resemblance of a coherent structure. The region containing the large eddy may also contain smaller eddies. The largest eddies are bounded by the flow geometry and the smallest by viscosity. The irregularity of turbulent flow makes it difficult to accurately predict its motion, which is why we typically apply statistical models to simulate turbulent flow.
2. Diffusivity. Fluid elements in turbulent flow experience three-dimensional, random convection due to the nature of the eddies, and thus allow for several magnitudes faster mixing of momentum and energy than its laminar counterpart.
3. Instability at large Re . At a certain threshold Reynolds number, the flow becomes turbulent. Physically, this occurs when the timescale for viscous damping of a velocity fluctuation is much larger than the timescale for convective transport (Andersson et al., 2012).
4. Three-dimensionality. Turbulence is inherently three dimensional, as vortex stretching and tilting cannot occur in 2D.
5. Turbulent energy dissipation. Known as an energy cascade, there exists an energy flux from the larger to the smaller eddies. The hierarchical flux eventually results in kinetic energy dissipation into the flow in the form of heat due to viscous stresses. Therefore, turbulence is rapidly decaying without sufficient energy supply.
6. Continuum. The smallest turbulent scales are much larger than a molecular scale, and thus abides by mass and momentum conservation laws.
7. All fluids can be turbulent given a sufficient Reynolds number.

2.4 Vortex shedding

Vortex shedding is a phenomenon that occurs for fluid flow around a circular cylinder for $Re > 40$. At this Re , the wake behind the cylinder becomes unstable, and vortices will be shed

alternately from each side of the cylinder. The separated boundary layers contain high vorticity which will transfer to the shear layer downstream of the separation point,

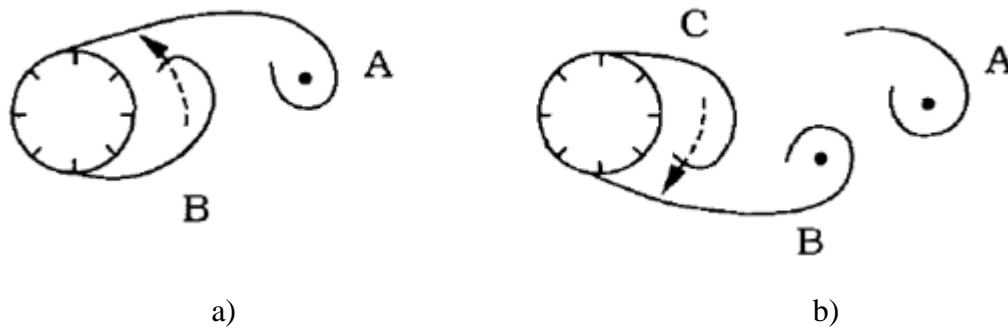


Figure 2.4: Vortex shedding principle (Sumer and Fredsøe, 2006, pp8).

The initial vortex will grow in size and draw in the newly formed vortex across the back end of the cylinder (Figure 2.4 a)), thus effectively canceling out any vorticity, leading to a cut-off of the initial vortex, which is convected downstream. The secondary vortex will now grow in size, and the shedding cycle repeats itself Figure 2.4 b).

2.4.1 Vortex shedding frequency

Vortex shedding frequency (f_v) is usually normalized with flow velocity (U) and cylinder diameter (D) so that it can be expressed as a function of Re :

$$St = St(Re) \quad (2.9)$$

where

$$St = \frac{f_v D}{U} \quad (2.10)$$

St is the dimensionless Strouhal number. With the onset of vortex shedding at $Re = 40$, St has an initial value of approximately 0.1, increasing to 0.2 at about $Re = 300$. From this point, the Strouhal number remains practically constant throughout the subcritical regime, as can be observed in Figure 2.5. In the transition to the critical regime, St suddenly jumps to about $St = 0.45$. At this Reynolds number ($3.5 \times 10^5 < Re < 1.5 \times 10^6$) the boundary layer is turbulent at the separation points. This results in a delayed flow separation, which pushes the two separation points downstream on the cylinder back surface. The separation points are now in closer to each other, decreasing the time of vortex interaction, thus increasing shedding frequency. In the upper transition regime, one of the boundary layers becomes completely

turbulent, creating asymmetric shedding in the wake. Shedding frequency exhibits a broadband power spectrum in this regime. At transcritical Reynolds number ($Re > 4.5 \times 10^6$) normal narrow-band power spectrum of shedding frequency returns as symmetry is restored in the boundary layers. The Strouhal number is larger ($0.25 < St < 0.3$) than in the subcritical regime.

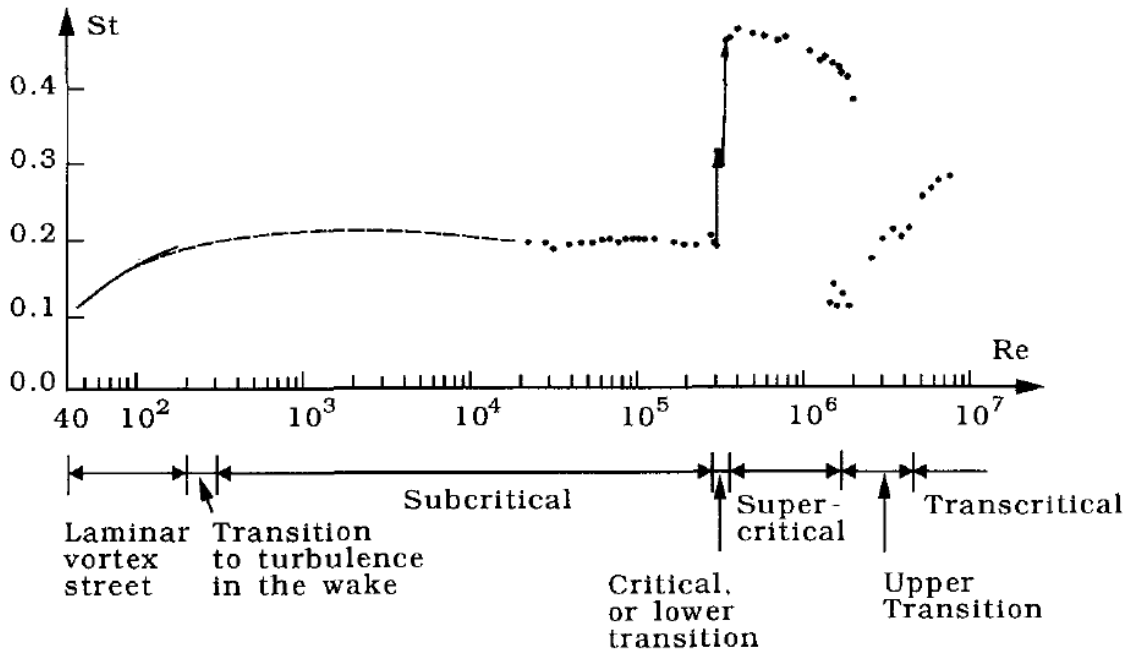
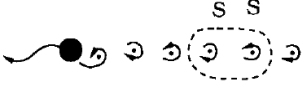
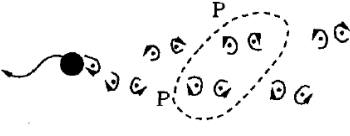
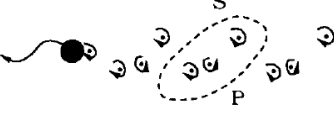
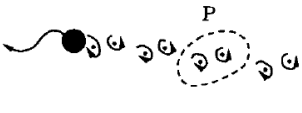
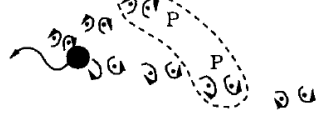
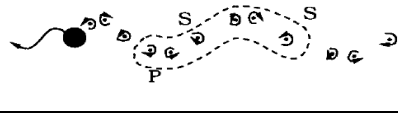


Figure 2.5: Strouhal number at different Reynolds number (Sumer and Fredsøe, 2006, pp.10).

2.4.2 Vortex shedding pattern

Several different patterns of vortex shedding can be observed in the wake of a cylinder. Intuitively, one would imagine a pattern in which a single vortex is being shed on alternating sides of the cylinder, and the wake taking the form of the well-known von Kármán street. However, it turns out there are many different patterns in which vortices can be shed. They can shed in singles, multiples, or uneven numbers of times from one side of the cylinder before alternating. A summary of the most frequently encountered patterns by Williamson and Roshko (1988) is given in Table 2.2. The authors note that the most common patterns found near lock-in (ref. chapter 2.10.4) region is 2S, 2P and P+S.

Table 2.2: Some different vortex shedding patterns (Williamson and Roshko, 1988).

Pattern	Name	Description
	2S	One vortex is shed every half cycle from opposite cylinder side in alternating fashion.
	2P	Vortex pairs are shed and convected laterally outwards.
	P+S	Single vortex shed on one side, and pair of vortices on the other side.
	P	Similar to 2P, but all pairs are convected in the same direction in the wake.
	2P*	As with 2P, only one pair is convected away from in front of the body.
	2P+2S	Two vortex pairs as with 2P, with single vortices in between.

2.5 Tandem cylinders

In the case of two equal diameter cylinders in tandem, the flow pattern depends on the cylinder spacing ($L^* = L/D$), where L is the gap distance between the cylinders. Zdravkovich (1987) classified three characteristic flow regimes; a single bluff-body regime at $1 < L^* < 1.2 \sim 1.8$ in which the von Kármán street is only observed in the wake of the downstream cylinder. A reattachment regime ($1.2 \sim 1.8 < L^* < 3.4 \sim 3.8$) where free shear layers emanating from the upstream cylinder reattach to the downstream cylinder, still featuring only a single von Kármán street. Finally, an impingement regime ($L^* > 3.4 \sim 3.8$) in which normal vortex shedding occurs behind the upstream cylinders, and the convected vortices periodically impinge on the downstream. A further two-part separation of the reattachment regime is suggested by Zhou and You (2006) depending on the reattachment position of the shear layers on the downstream cylinder. In the $2 < L^* < 3$ regime, the reattachment occurs on the leading end, whilst for $3 < L^* < 5$ the reattach position is on the trailing end.

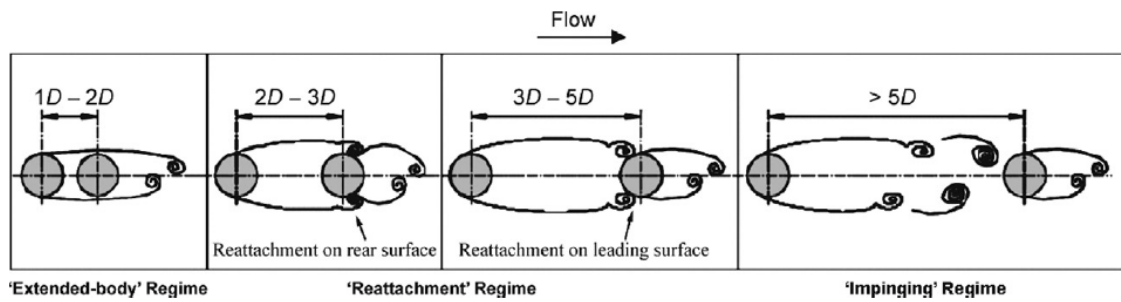


Figure 2.6: Tandem flow regimes (Zhou and Yiu, 2006, pp. 19, modified by Wang et al 2015).

2.6 Surface roughness

Figure 2.7 displays the effect of cylinder surface roughness on the Strouhal number. It is apparent that cylinder roughness plays a significant role in vortex shedding frequency for Reynolds number in the critical regime.

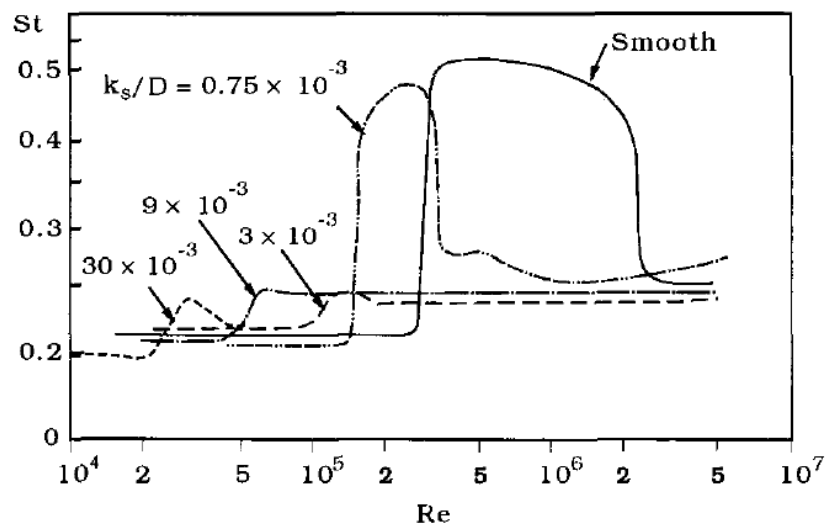


Figure 2.7: Strouhal number at different Reynolds for different surface roughness parameters (Achenbach and Heineke, 1981, pp. 247).

Achenbach and Heinecke (1981) performed wind-tunnel experiments on cylinders with different relative roughness parameters ($k_s/D = 0.75 \times 10^{-3}, 3 \times 10^{-3}, 9 \times 10^{-3}, 30 \times 10^{-3}$), and found that the wake behind very smooth cylinders exhibited a very chaotic and disorganized behavior, with St as high as 0.5. k_s is the Nikuradse's equivalent sand roughness of the cylinder surface. Smaller relative roughness parameter exhibits much narrower spectra

with elevated Strouhal number and can be explained by the earlier turbulence transition for flow over rough surfaces.

2.7 Wall proximity

The interaction between opposing vortices implies that vortex shedding can be suppressed should the shedding sequence be interrupted or impinged in some way. An extensive review of different vortex shedding suppression methods has been performed by Rashidi et al. (2016). In the present study, interest falls on wall proximity. Vortex shedding can be suppressed on the cylinder surface facing the wall if the distance to the wall is sufficiently small. A typical case in which wall proximity can affect the cylinder is a subsea pipeline experiencing scour. This process can result in areas with free spanning pipelines close to the seabed. Proximity has been subject to numerous experimental and numerical studies, but the general consensus, as summarized by Sumer and Fredsøe (2006), is that

- At gap ratio smaller than 0.3 ($G^* < 0.3$) vortex shedding is completely suppressed for static cylinders. For vibrating cylinders, shedding has been observed at much smaller gaps (e.g., at $G^* = 0.002$ (Zhao and Cheng (2011))).
- As a result of asymmetry in the pressure distribution, the stagnation point will move to a position on the cylinder surface closer to the wall.
- The freestream separation point will move upstream, whilst the separation point on the opposite side of the cylinder will move downstream.
- Suction is larger on the freestream side of the cylinder, which causes a non-zero mean lift.

Because vortices increase in size on the freestream side and decrease on the wall side, the interaction between the two is largely inhibited and eventually results in shedding suppression. The pressure distribution with respect to wall proximity can be seen in Figure 2.8. Horizontal pressure is reduced with decreasing gap ratio, thus making it apparent that the drag force also decreases with decreasing gap ratio.

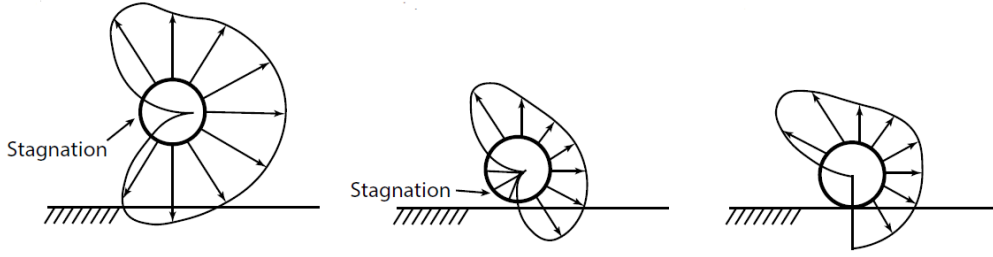


Figure 2.8: Pressure distribution at different wall gap ratios (Sumer and Fredsøe, 2006, pp. 58).

2.8 Hydrodynamic force

The resultant hydrodynamic force exerted by the flow on the cylinder, is the integral sum of time averaged pressure (\bar{p}) and time averaged wall shear stress ($\bar{\tau}$) over the cylinder surface.

$$\bar{F}_p = \int_0^{2\pi} \bar{p} \cos(\phi) r_0 d\phi \quad (2.11)$$

$$\bar{F}_f = \int_0^{2\pi} \bar{\tau}_0 \sin(\phi) r_0 d\phi \quad (2.12)$$

where \bar{F}_p is the mean pressure force, \bar{F}_f is the mean friction force, ϕ is the angle from stagnation to separation point and r_0 is the radius of the cylinder.

The total force is acting in two directions, in-line (IL) and cross-flow (CF) as illustrated in Figure 2.9. The mean in-line force is called drag force (\bar{F}_D), and mean cross-flow is called lift (\bar{F}_L):

$$\bar{F}_D = \bar{F}_{p,IL} + \bar{F}_{f,IL} \quad (2.13)$$

$$\bar{F}_L = \bar{F}_{p,CF} + \bar{F}_{f,CF} \quad (2.14)$$

In the case of a cylinder in free-flow, the mean lift will be zero due to flow symmetry. However, if Reynolds is sufficient to induce vortex shedding, then the instantaneous cross-flow force will be non-zero.

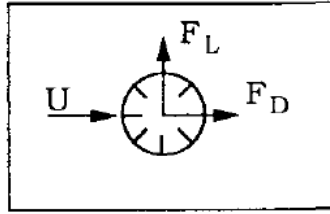


Figure 2.9: Drag and lift force of a cylinder in flow (Sumer and Fredsøe, 2006, pp.39).

Due to vortices being shed on alternating cylinder poles, pressure distribution – and thus also force component – exhibit a periodic variation. Pressure field and force distribution over a shedding cycle can be seen in Figure 2.10. As a vortex is shed from the top surface of a cylinder velocity and pressure is peaking in this area. The resultant force is acting upwards into the wake. Now a vortex begins to form at the bottom and pressure distribution shifts downward. During this transition, there will be a period with zero lift and reduced drag before another pressure and force peak is reached at the bottom surface.

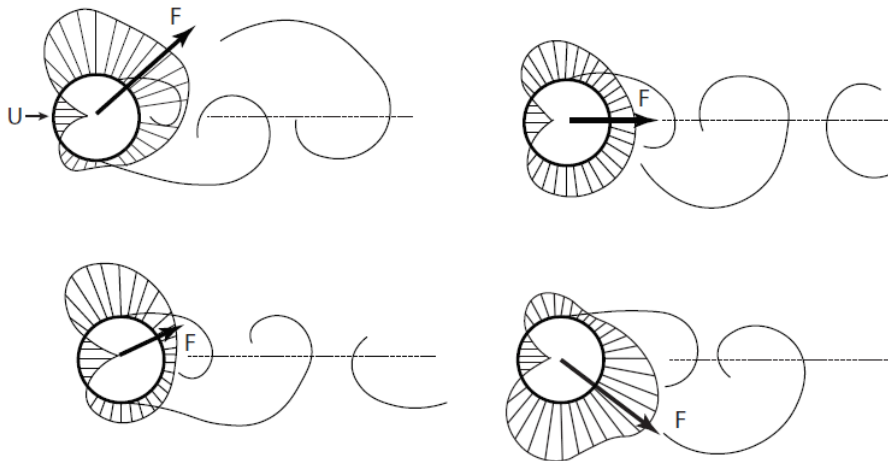


Figure 2.10: Pressure distribution on cylinder surface for a cycle of vortex shedding. (Sumer and Fredsøe, 2006, pp.26).

2.8.1 Drag and lift coefficients

Equation 2.13 can be re-written in the following form:

$$\frac{\overline{F_D}}{\frac{1}{2}\rho DU^2} = \int_0^{2\pi} \left[\left(\frac{\overline{p} - p_0}{\rho U^2} \right) \cos(\phi) + \left(\frac{\overline{\tau}_0}{\rho U^2} \right) \sin(\phi) \right] d\phi \quad (2.15)$$

where ρ is the density of the fluid, D is the diameter of the cylinder ($= 2r_0$), and U is the flow velocity. The right-hand side of this equation is a function of the Reynolds number and can be re-written as:

$$\frac{\overline{F_D}}{\frac{1}{2}\rho DU^2} = \overline{C_D} \quad (2.16)$$

where $\overline{C_D}$ is the dimensionless drag coefficient. Equivalently the lift coefficient, $\overline{C_L}$, is defined as:

$$\frac{\overline{F_L}}{\frac{1}{2}\rho DU^2} = \overline{C_L} \quad (2.17)$$

Thus drag and lift coefficients can be expressed as functions of Re .

2.9 Equation of motion

The motion of a single cylinder free to oscillate in a single degree-of-freedom is governed by

$$m\ddot{x}(t) + c\dot{x}(t) + kx(t) = 0 \quad (2.18)$$

where m is the mass of the system, c is the damping coefficient, k is the spring stiffness, $\ddot{x}(t)$ is the acceleration, $\dot{x}(t)$ is the velocity and $x(t)$ is the displacement (Chakrabarti, 1987). Assuming a solution of Equation 2.18 the form:

$$x = Xe^{qt} \quad (2.19)$$

where X and q are unknown constants. Substituting into Equation 2.18 yields:

$$X(mq^2 + cq + k)e^{qt} = 0 \quad (2.20)$$

which must be satisfied for all t . Thus

$$mq^2 + cq + k = 0 \quad (2.21)$$

provides two values of q , expressed as

$$q_{1,2} = -\frac{c}{2m} \pm \sqrt{\left(\frac{c}{2m}\right)^2 - \left(\frac{k}{m}\right)} \quad (2.22)$$

If the terms under the root are equal to zero, there will only be one solution of q . This is known as the critical damping condition, and the corresponding critical damping coefficient is defined by

$$c_{cr} = 2m\omega_n = 2\sqrt{km} \quad (2.23)$$

where $\omega_n = \sqrt{k/m}$ is the undamped natural frequency. The nondimensional damping ratio can now be defined as

$$\zeta = \frac{c}{c_{cr}} = \frac{c}{2\sqrt{km}} \quad (2.24)$$

A system is underdamped for $0 < \zeta < 1$, overdamped for $\zeta > 1$ and critically damped when $\zeta = 1$.

2.9.1 Two-degree-of-freedom system

When introducing external forces (lift and drag fluctuate as a consequence of vortex shedding) and allowing a second degree-of-freedom, the dynamic system is governed by the equations of motion on the following form:

$$(m + m_a)\ddot{x}(t) + c\dot{x}(t) + kx(t) = F_x(t) \quad (2.25)$$

$$(m + m_a)\ddot{y}(t) + c\dot{y}(t) + ky(t) = F_y(t) \quad (2.26)$$

where m_a is the hydrodynamic added mass, and $F_x(t)$ and $F_y(t)$ are forces induced by vortex shedding in x and y directions, respectively.

2.10 Vortex-induced vibrations

A submerged cylinder in fluid flow characterized by Reynolds number larger than 40 will experience vortex shedding. This implies that in most of the offshore engineering applications the cylinder will experience fluctuating drag and lift forces. These fluctuating forces will excite the structural vibrations. This is known as *vortex-induced vibration*. Several parameters are used to characterize the VIV process. The most important governing parameters of VIV are the previously discussed Strouhal and Reynolds numbers, reduced velocity, U_r , mass ratio, m^* , and displacement amplitude ratio, A^* .

2.10.1 Reduced velocity

The ratio of flow velocity to vibration frequency, U/f_n describes the vibration path length of a body. The reduced velocity is defined as the ratio of flow velocity to vibration frequency normalized with the characteristic length of the body:

$$U_r = \frac{U}{f_n D} \quad (2.27)$$

where U is the freestream flow velocity, f_n is the natural frequency of the cylinder, and D is the characteristic length (diameter in the case of a cylinder).

2.10.2 Mass ratio

Mass ratio is the ratio of mass per unit length to mass of displaced fluid. For a cylinder, it is given by:

$$m^* = \frac{m}{\rho \pi \frac{D^2}{4} L} \quad (2.28)$$

Low mass ratio implies a lightweight structure which is typically more susceptible to flow-induced vibrations. This dimensionless parameter expresses the relative importance of buoyancy and added mass effects.

2.10.3 Displacement amplitude ratio

The ratio of displacement caused by vibrations to the diameter of the cylinder is known as the displacement amplitude ratio:

$$\frac{A_i}{D} \quad (2.29)$$

where $i = X$ for transverse displacement and $i = Y$ for in-line displacement.

2.10.4 Lock-in phenomenon

Lock-in (also known as synchronization) is the alignment of the vortex shedding frequency, f_v , and the natural frequency, f_n , of the system. When the two frequencies approach a common frequency (i.e., $\frac{f_{vs}}{f_n} \approx 1$), the cylinder will experience VIV at oscillation frequency, f_{osc} . The

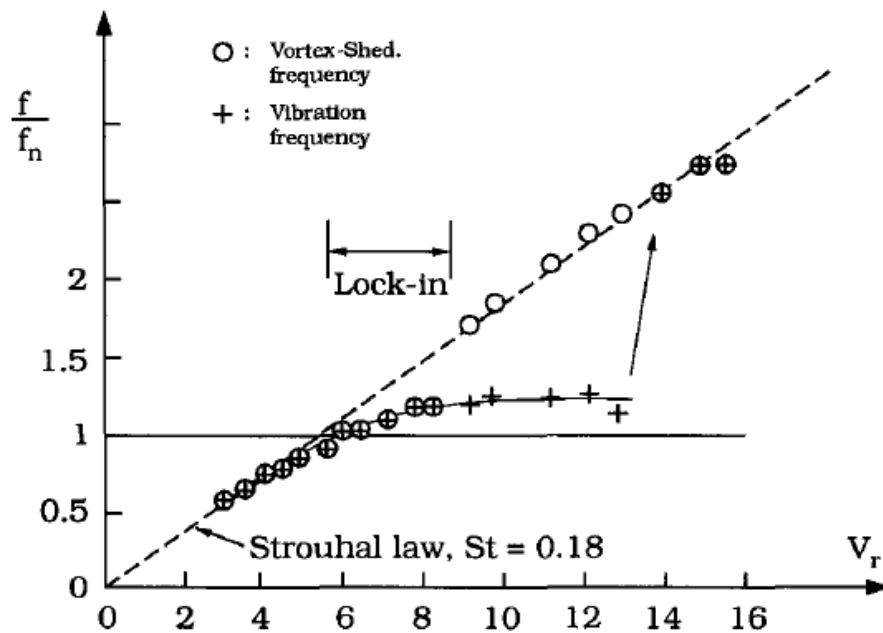


Figure 2.11: Crossflow response of a submerged cylinder (Sumer and Fredsøe, 2006, pp. 359).

vortex shedding remains locked onto the oscillation frequency for a range of reduced velocities (Figure 2.11). At these resonant conditions, displacement amplitudes will increase dramatically. Initially, an increasing U_r will provide energy to the system, until an energy balance is met in the lock-in region, and A_{max}/D is reached. Further increase in U_r will desynchronize the natural frequency, f_n , from f_{osc} and lock-in dissipates. The magnitude of displacement ratio is related to the reduced velocity, as can be seen in Figure 2.12. In this specific case, vibrations begin at around $U_r = 4$. Somewhere between $U_r = 5$ to $U_r = 6$ a sudden jump in displacement amplitude occurs. For $6 < U_r < 7 \sim 8$ a sudden decrease can be seen, at which point displacement amplitudes will remain slightly decreasing before experiencing yet a sudden decrease at around $U_r = 9$.

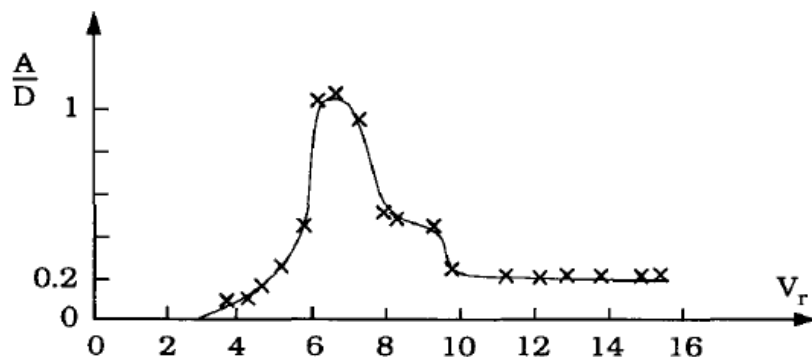


Figure 2.12: Dependence between displacement amplitude ratio and reduced velocity for a submerged cylinder (Sumer and Fridsøe, 2006, pp. 359).

These three ranges of reduced velocity are known as the initial-, upper-, and lower branches. Govardhan and Williamson (2000) conducted studies on the displacement amplitude for low damped systems and explained that there exists a hysteric jump from initial to upper branch, and an intermittent jump from upper to lower branch (Figure 2.13). During these branch jumps, there will also be jumps in the phase between transverse force and cylinder displacement.

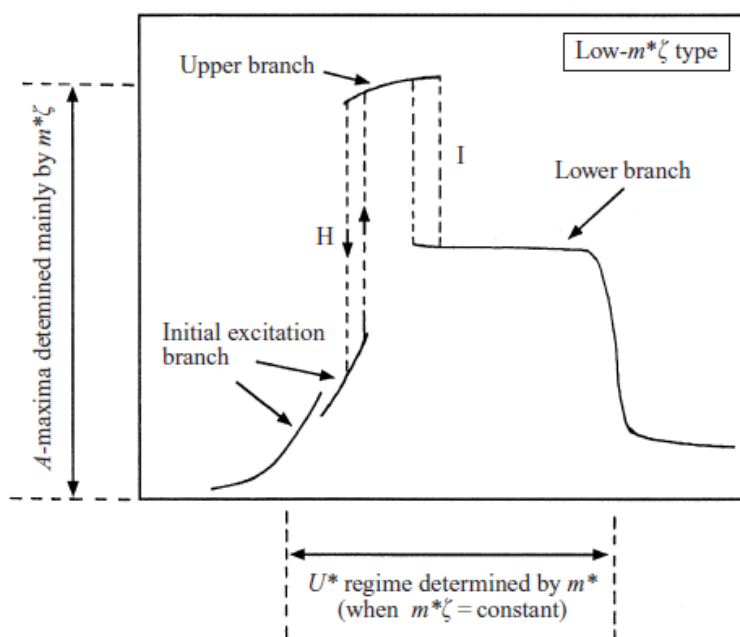


Figure 2.13: Low mass system amplitude response diagram (Williamson and Govardhan, 2004, pp. 426).

It should be underlined that this diagram is applicable for low mass-damping type systems. Higher mass-damping systems only exhibit initial and lower branches. For very low damped systems ($m^* < 6$) Jauvits and Williamson (2003) discovered an additional response branch in which large peak amplitudes ($A_y/D \sim 1.5$) were observed. This branch was defined as the

“super-upper” branch, in which a characteristic vortex shedding pattern of a pair of triplets (2T) can be observed.

3 COMPUTATIONAL FLUID DYNAMICS

The present chapter introduces the basic concepts of CFD. The methodology of the OpenFOAM code is explained, specifically the governing equations, the Finite Volume Method and turbulence modelling.

3.1 Introduction

According to Versteeg and Malalasekera (2007), all CFD codes contain three elements: a *pre-processor*, a *solver* and a *post-processor*. The pre-processing is the initial setup of inputs that are required for the solver. These activities include setting up the computational domain, grid generation, selecting phenomena and fluid properties to be modeled and specifying appropriate boundary conditions. It is estimated that 50 % of the time devoted to a CFD project is spent on defining domain geometry and grid generation. The *solver* is dependent on the software in use. Three different techniques are used for solving the flow fields: finite difference, finite volume, and spectral methods. The focus here will be on the finite volume method. In essence, the finite volume method integrates the governing equations of fluid flow over all the finite control volumes in the domain, applies discretization to the equations, and solves the resulting algebraic system iteratively. *Post-processing* is the analysis and visualization of the results.

3.2 OpenFOAM

OpenFOAM (Open Field Operation And Manipulation) is an open source computational fluid dynamics software, that uses the finite volume method to solve discretized conservation equations over the computational domain. It is a C++ text-file based system with no native global user interface (GUI). OpenFOAM libraries contain a wide range of different numerical solvers written for specific applications like compressible flows, multiphase flows or reacting flows. The software provides applications for pre-processing, solver and post-processing. An overview is provided in Figure 3.1.

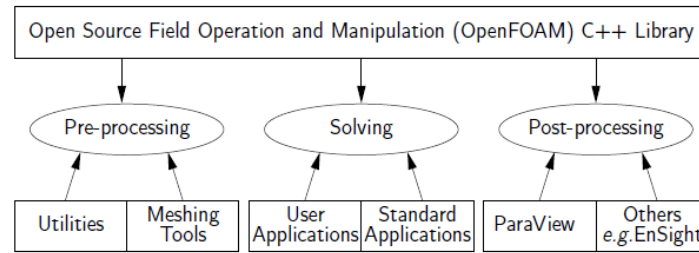


Figure 3.1: Overview of OpenFOAM structure (OpenFOAM User Guide, pp. U-17).

An OpenFOAM case will always contain three directories at minimum. The `system` folder consists of at least three files (Figure 3.2): `fvSolution`, `fvSchemes` and `controlDict`. `fvSolution` determines which solvers will be applied, `fvSchemes` selects the discretization schemes and `controlDict` configures the simulation parameters such as timesteps, runtime and output files. `setFieldsDict` and `topoSetDict` are optional files that are used to define the content and arrangement of cells respectively.

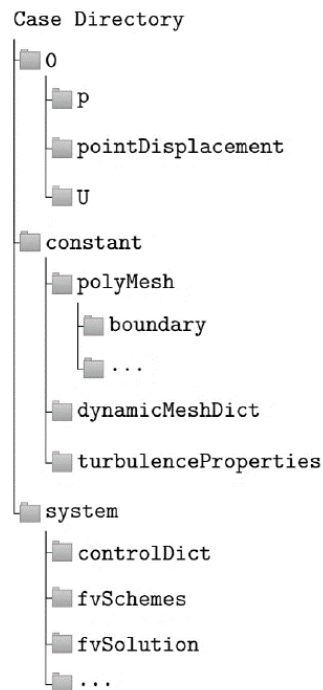


Figure 3.2: Example OpenFOAM directory hierarchy.

The constant directory contains files that do not change during the simulation, such as `turbulenceProperties`, `dynamicMeshDict`, and the grid data files themselves, in the `polyMesh` folder. If the mesh is dynamic, its topology and motion settings are defined in `dynamicMeshDict`. The third main directory is the `0` folder, which contains the initial values of the domain, such as velocity or turbulence parameters.

3.3 Governing equations

The fundamental equations that all CFD models are governed by is the continuity and momentum equations. They are based on the basic physical principles of mass conservation, force equilibrium, and energy conservation.

3.3.1 Continuity

Consider a fluid element dV with sides $\delta x, \delta y, \delta z$ and center in (x, y, z) as seen in Figure 3.3. The mass balance of the element states that the rate of increase of mass has to equal the net rate of flow of mass. The rate of increase of mass in the fluid element is

$$\frac{\partial}{\partial t}(\rho \delta x \delta y \delta z) = \frac{\partial \rho}{\partial t} \delta x \delta y \delta z \quad (3.1)$$

Next consider the mass flow rate across a face of the element, as shown in Figure 3.3. Equaling the terms with Equation 3.1 and sorting yields

$$\frac{\partial \rho}{\partial t} + \frac{\partial(\rho u)}{\partial t} + \frac{\partial(\rho v)}{\partial t} + \frac{\partial(\rho w)}{\partial t} = \rho \frac{Du}{Dt} = 0 \quad (3.2)$$

This is the mass conservation, or *continuity equation* for an unsteady, three-dimensional, compressible fluid. For an incompressible fluid, the equation reduces to:

$$\frac{\partial u}{\partial t} + \frac{\partial v}{\partial t} + \frac{\partial w}{\partial t} = 0 \quad (3.3)$$

Equation 3.3 is the continuity equation for an unsteady, three-dimensional, *incompressible*, fluid.

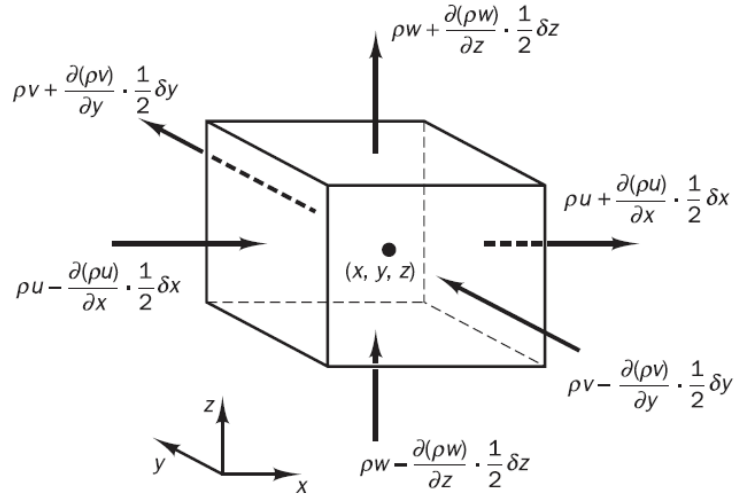


Figure 3.3: Mass-flow in and out of fluid element (Versteeg and Malalasekera, 2007, pp. 11).

3.3.2 Momentum

The principle of force equilibrium – Newton’s second law – is applied to the fluid particle. The rate of increase of momentum of that particle is equal to the sum of forces affecting it. These forces are separated into surface (e.g. pressure, viscous) forces, and body (e.g. electromagnetic, centrifugal) forces. The momentum equations in three dimensions are expressed by:

Momentum in x -direction

$$\rho \frac{Du}{Dt} = \frac{\partial(-p + \tau_{xx})}{\partial x} + \frac{\partial\tau_{yx}}{\partial y} + \frac{\partial\tau_{xz}}{\partial z} + S_{Mx} \quad (3.4)$$

Momentum in y -direction

$$\rho \frac{Dv}{Dt} = \frac{\partial\tau_{xy}}{\partial x} + \frac{\partial(-p + \tau_{yy})}{\partial y} + \frac{\partial\tau_{zy}}{\partial z} + S_{My} \quad (3.5)$$

Momentum in z -direction

$$\rho \frac{Dw}{Dt} = \frac{\partial\tau_{xz}}{\partial x} + \frac{\partial\tau_{yz}}{\partial y} + \frac{\partial(-p + \tau_{zz})}{\partial z} + S_{Mz} \quad (3.6)$$

Where surface forces are accounted for explicitly (p for pressure, and τ for viscous), and body forces are included in the source terms S_{Mx} , S_{My} , S_{Mz} .

3.3.3 Navier-Stokes equations

A general assumption made throughout this thesis is that the fluid considered in the simulations is Newtonian. Newton's law of viscosity in three dimensions includes nine viscous stress components, of which six are independent. By substituting these into the momentum equations, the Navier-Stokes (NS) equations for a three-dimensional, compressible fluid expressed:

NS in x -direction

$$\rho \frac{Du}{Dt} = -\frac{\partial p}{\partial x} + \left(\frac{\partial \tau_{xx}}{\partial x} + \frac{\partial \tau_{yx}}{\partial y} + \frac{\partial \tau_{zx}}{\partial z} \right) + S_{Mx} \quad (3.7)$$

NS in y -direction

$$\rho \frac{Dv}{Dt} = -\frac{\partial p}{\partial y} + \left(\frac{\partial \tau_{xy}}{\partial x} + \frac{\partial \tau_{yy}}{\partial y} + \frac{\partial \tau_{zy}}{\partial z} \right) + S_{My} \quad (3.8)$$

NS in z -direction

$$\rho \frac{Dw}{Dt} = -\frac{\partial p}{\partial z} + \left(\frac{\partial \tau_{xz}}{\partial x} + \frac{\partial \tau_{yz}}{\partial y} + \frac{\partial \tau_{zz}}{\partial z} \right) + S_{Mz} \quad (3.9)$$

The 2D Navier-Stokes equations are commonly shortened using index notation:

$$\frac{\partial u_i}{\partial x_i} = 0 \quad (3.10)$$

$$\frac{\partial u_i}{\partial t} + u_j \frac{\partial u_i}{\partial x_j} = -\frac{1}{\rho} \frac{\partial p}{\partial x_i} + \nu \frac{\partial^2 u_i}{\partial x_j^2} \quad (3.11)$$

where $i, j = 1, 2$, u_i and u_j are velocity components, t is time, and x_i and x_j are cartesian direction components (i.e., x and y).

3.4 Finite Volume Method

The finite volume method (FVM) is based on the discretization of the integral forms of the conservation equations. The flow field is separated into non-overlapping cells that cover the entirety of the domain and conservation laws are applied at discrete points within the cells, such as cell-centers or vertices, and interpolated across the cell volume. The generic integral form of the conservation equations is given as

$$\frac{\partial}{\partial t} \iiint_V \phi dV + \iint_A \mathbf{F} d\mathbf{A} = \iiint_V V_V dV + \iint_A V_A dA \quad (3.12)$$

Where ϕ is the unknown quantity, A is the control surface, V is the control volume, V_A and V_V are possible sources of ϕ on the surface and inside volume respectively, and \mathbf{F} is the flux associated with ϕ .

3.4.1 Spatial discretization

As implied by its name, the *volumetric* discretization is paramount in the finite volume method. The spatial domain is separated into discrete control volumes (CVs). The CVs have flat faces which are shared with only one neighboring volume unless they are boundary faces. An example CV can be seen in Figure 3.4. P is the centroid of the cell, N is the centroid of the neighboring cell, f is the center of the face and \underline{S} is the face-area vector.

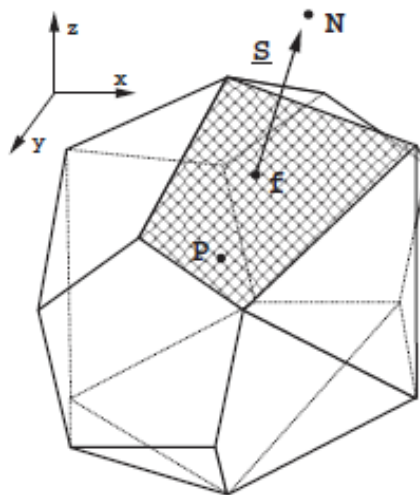


Figure 3.4: Example control volume (Jasak, 1996, pp. 75).

The CV can have any amount of faces – a polyhedral. A generalized spatial discretization equation can be written on the form (Jasak, 1996):

$$\int_{V_P} (\mathbf{x} - \mathbf{x}_P) dV = \mathbf{0} \quad (3.13)$$

where P is the centroid of the CV and V_P is the volume of the CV. This discretization method is applicable to any arbitrary polyhedral control volume, which allows for geometrically complex meshes. Calculated values are stored in the cell center, a method that known as a

collocated grid. In order to express the values at a cell face, interpolation of the cell centers is required. The examples presented here will cover linear interpolation, but other interpolation schemes are available. The interpolation expression for a scalar variable, ϕ , is given by

$$\phi_f = f_x \phi_P + (1 - f_x) \phi_N \quad (3.14)$$

in which f_x is the linear interpolation factor:

$$f_x = \frac{|x_f - x_N|}{|x_f - x_N| + |x_f - x_P|} \quad (3.15)$$

where the terms follow the nomenclature of the example CV provided in Figure 3.4.

Generally, grids are either structured or unstructured. Examples of both variants are shown in Figure 3.5. Structured meshes are typically constructed using quadrilateral elements in 2D, and hexahedra in 3D. Indexing and locating neighboring cells is easy, and so structured meshes often require less computational resources whilst providing very good grid control. An unstructured mesh can be built using many different element shapes (e.g., triangular or quadrilateral for 2D, tetrahedra, hexahedra, pyramids for 3D). This allows for more complex geometry to be meshed, as well as the creation of refinement zones in areas where higher accuracy is desired.

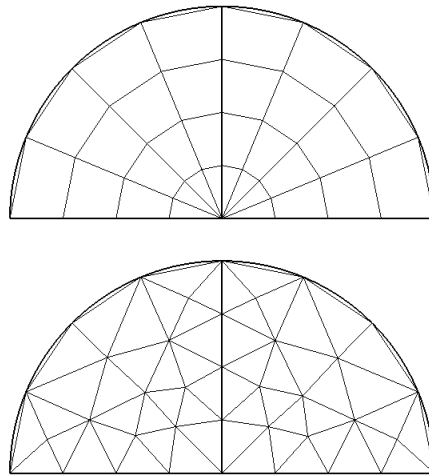


Figure 3.5: Structured (top) and unstructured (bottom) meshes.

3.4.2 Temporal discretization

As with interpolation schemes, there are several ways of discretizing the temporal domain. The following method is the Crank-Nicolson method, which uses the trapezoidal rule (Figure 3.6)

for numerical integration. The scheme expresses the values in terms of the time average of the explicit and implicit schemes:

$$\phi^{n+1} = \phi^n + \frac{1}{2} [f(t^n, \phi^n) + f(t^{n+1}, \phi^{n+1})] \Delta t \quad (3.16)$$

The method is second-order accurate. Present face values are dependent on both the previous and subsequent cell values, and so an algebraic set of equations is solved for every CV.

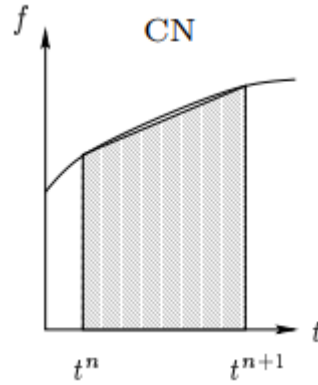


Figure 3.6: Trapezoidal rule applied in Crank-Nicolson numerical integration scheme.

3.4.3 Equation discretization

This section will cover the discretization of the continuity and momentum equations (Equations 3.3, 3.4-3.6). Assuming incompressible fluid, the discretization of the continuity equation is performed in the following way:

$$\int_{V_P} \nabla \cdot \mathbf{u} dV = 0 \quad (3.17)$$

On which Green's theorem can be applied, yielding:

$$\int_{A_P} \mathbf{u} \cdot \mathbf{n} dA = 0 \quad (3.18)$$

where A_P is CV surface, \mathbf{u} is the velocity vector and \mathbf{n} is the vector normal to surface A_P . Recognizing that the spatial domain is separated into a finite number of flat faces, N , with areas, A_n , Equation 3.18 can be written on the following form:

$$\sum_{n=1}^N \int_{A_P} U dA = \sum_{n=1}^N \tilde{U}_n A_n = 0 \quad (3.19)$$

where $U = \mathbf{u} \cdot \mathbf{n}$ is the velocity normal to face N , and \tilde{U} is the face average value of U . Equation 3.19 is the discretized continuity equation.

Applying the integral form of the conservation equation to the momentum equations yields

$$\int_{V_P} \frac{\partial \mathbf{u}}{\partial t} dV + \int_{V_P} \nabla \cdot (\mathbf{u}\mathbf{u}) dV - \int_{V_P} \nabla \cdot (\nu \nabla \mathbf{u}) dV = \int_{V_P} \frac{\nabla p}{\rho} dV \quad (3.20)$$

A similar procedure to that applied to the continuity equation above is used for the discretization of the terms in the momentum equations.

3.5 PIMPLE algorithm

In order to solve the incompressible Navier-Stokes equations, a PIMPLE algorithm is used. PIMPLE is a combination of the SIMPLE (Semi-Implicit Method for Pressure-Linked Equations) and PISO (Pressure-Implicit with Splitting of Operator) algorithms.

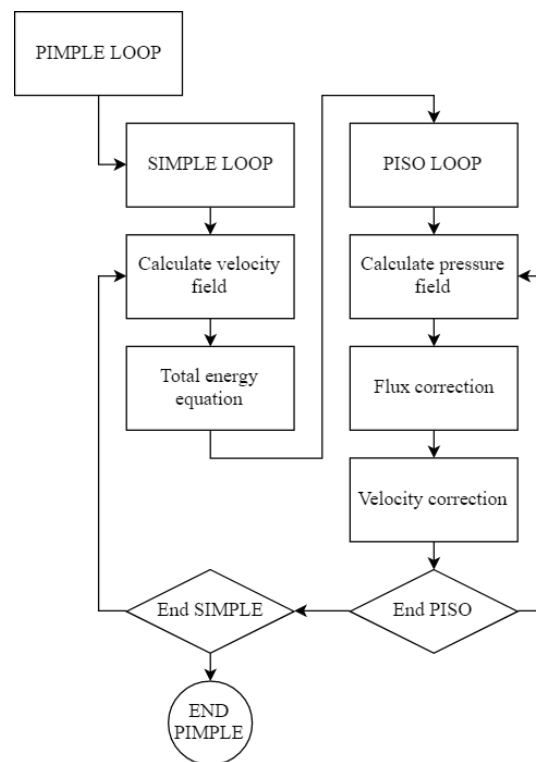


Figure 3.7: Flowchart of PIMPLE solver.

It is implemented in OpenFOAM as `pimpleFoam` (previously `pimpleDyMFoam` – the dynamic meshing option has been included in `pimpleFoam` as of OpenFOAM v18.12). A flowchart of the solution procedure is shown in Figure 3.7.

3.6 Turbulence modelling

Turbulence modelling in CFD is performed with one of three different techniques: Direct numerical simulation (DNS), large eddy simulation (LES) and Reynolds-averaged Navier-Stokes (RANS). These techniques vary in their level of complexity. DNS is the most accurate technique and computes the mean flow by directly solving the NS equations for *all* turbulent length scales and timescales. In order to do so, extremely fine grids and extremely sophisticated computer hardware is required. Even for industrial use with supercomputers, the long simulation time renders this technique unpractical for most flow simulations. A less demanding solution is to perform LES. In LES the smallest eddies are modelled, rather than calculated, and assumed to be isotropic. By this assumption, simulation time is drastically reduced compared to DNS, but still not sufficient to warrant the use of LES for most common applications. The last technique is RANS, in which *all* unsteady, turbulent eddies are modeled mathematically. Unsteady RANS (URANS) is the turbulence modelling approach in the present thesis and will be further described in the following sections.

3.6.1 Unsteady Reynolds-averaged Navier-Stokes (URANS)

As flow velocity increases beyond a limiting Reynolds number, it becomes unstable and chaotic, and turbulence occurs. In order to describe fluid motion in this regime, a Reynolds decomposition (Figure 3.8) is applied. Following the notation used in the shortened NS equations (Equations 3.10, 3.11) u_i , is decomposed into an average value, U_i , with a fluctuating value, u_i' , superimposed on it, in such a way that the turbulent fluctuations can be described with $u_i = U_i + u_i'$. By taking the average of u_i and noting that the commutative property of the operations, it can be shown that

$$\frac{\partial \bar{u}_i}{\partial x_i} = 0 \quad (3.21)$$

which is the continuity equation for the mean flow. Similarly, when the time-averaging is applied to the momentum equations it reads (Wilcox, 2006):

$$\frac{\partial \bar{u}_i}{\partial t} + \bar{u}_j \frac{\partial \bar{u}_i}{\partial x_j} = -\frac{1}{\rho} \frac{\partial p}{\partial x_i} + \nu \frac{\partial^2 \bar{u}_i}{\partial x_j^2} - \frac{\partial \overline{u_i' u_j'}}{\partial x_j} \quad (3.22)$$

This introduces a new term, $\overline{u_i' u_j'}$ which is known as the Reynolds stress tensor, and is expressed as:

$$\overline{u_i' u_j'} = \tau_{ij} = \nu_t \left(\frac{\partial \bar{u}_i}{\partial x_j} + \frac{\partial \bar{u}_j}{\partial x_i} \right) - \frac{2}{3} k \delta_{ij} \quad (3.23)$$

where ν_t is the turbulent viscosity, k is the turbulent kinetic energy and δ_{ij} is the Kronecker's delta. Many different models are developed in order to solve the resulting system of equations. The $k - \omega$ SST (shear stress transport) model is discussed in the following section. Equations 3.21 and 3.22 are the unsteady Reynolds-averaged Navier-Stokes (URANS). The difference between URANS and RANS is the absence of the transient term $\frac{\partial \bar{u}_i}{\partial t}$ in steady-state RANS.

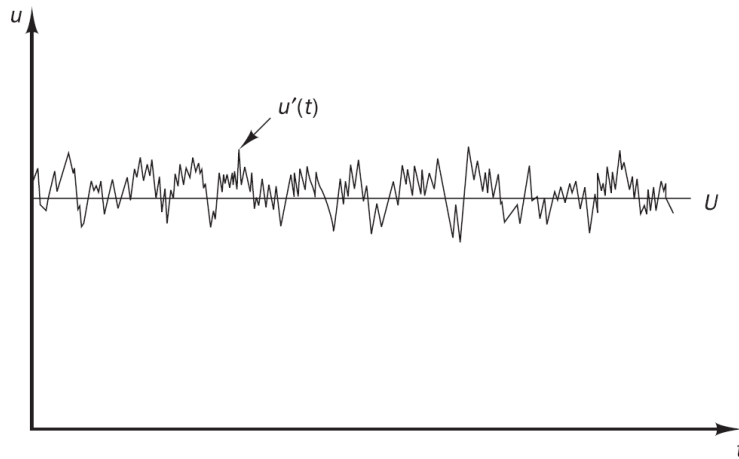


Figure 3.8: Reynolds decomposition of a turbulent velocity signal.

3.6.2 $k - \omega$ SST Turbulence Model

The $k - \omega$ SST turbulence model is a two-equation eddy-viscosity model which is a combination of $k - \epsilon$ and $k - \omega$ models. k is the turbulent kinetic energy, ϵ is turbulent dissipation rate and ω is the specific dissipation rate. $k - \omega$ SST model yields good results in flows with adverse pressure gradient and separated boundary layers. Expressions for k and ω are given by:

$$\frac{D\rho k}{Dt} = \tau_{ij} \frac{\partial u_i}{\partial x_j} - \beta^* \rho \omega k + \frac{\partial}{\partial x_j} \left[(\mu + \sigma_k \mu_t) \frac{\partial k}{\partial x_j} \right] \quad (3.24)$$

$$\frac{D\rho\omega}{Dt} = \frac{\gamma}{\nu_t} \tau_{ij} \frac{\partial u_i}{\partial x_j} - \beta\rho\omega^2 + \frac{\partial}{\partial x_j} \left[(\mu + \sigma_\omega \mu_t) \frac{\partial \omega}{\partial x_j} \right] + 2(1 - F_1)\rho\sigma_\omega^2 \frac{1}{\omega} \frac{\partial k}{\partial x_j} \frac{\partial \omega}{\partial x_j} \quad (3.25)$$

where F_1 is a blending function used to determine if either $k - \epsilon$ or $k - \omega$ model should be applied:

$$\phi = F_1\phi_1 + (1 - F_1)\phi_2 \quad (3.26)$$

Constants and further definitions of Equations 3.24, 3.25, 3.26 can be found in Menter (1994). It is important to understand that the omega model is applied in the viscous layers near a boundary, while the epsilon model is used in free-stream regions.

3.6.3 Blended wall function

The present dynamic simulations employ a dynamic mesh morphing algorithm in which the mesh is deformed to account for the body motion induced by the fluid. Furthermore, in contrast to static case, the moving boundary velocity will change relative to the fluid velocity depending on the phase of the oscillatory motion. This considerably increases the variability in the mesh cell size and flow velocity next to the moving wall. A consequence of this are fluctuations in y^+ values which can be outside the range of applicability of wall functions (Section 2.2.2). To account for this, an additional blending function is applied to smoothly transition between using wall-function and integration to the surface using a low Reynolds number formulation (Menter et al., 2003). Blending of ω based on y^+ can be expressed as follows:

$$\omega(y^+) = \sqrt{\omega_{vis}^2(y^+) + \omega_{log}^2(y^+)} \quad (3.27)$$

where ω_{vis} and ω_{log} are contributions from the viscous- ($y^+ \leq 1$) and logarithmic ($30 < y^+ < 500$) sublayers, respectively. For further explanation, the reader is referred to Menter et al. (2003).

4 STATIC CYLINDER IN WALL PROXIMITY

The following chapter will present the process of creating a numerical model of a static single cylinder in wall proximity. The aim is to establish a model that accurately represents physical phenomena without excessive computational cost. When the static model is validated, it will be further developed for VIV assessment. The benefit of initially performing a static study is two-fold; (1) static simulations require significantly less computational resources, (2) available model validation data for dynamic cases is scarce in comparison to static.

4.1 Grid generation

A fully structured hexahedral mesh is generated using GMSH, which is a meshing software distributed under a GNU General Public License. The mesh is highly refined in areas where large gradients are expected – namely in the proximity of the cylinder – and coarsened in the far-field to decrease computational cost, as seen in Figure 4.1. A parametric grid approach using a scaling factor is applied. This ensures equal mesh density regions as total cell count is increased for the convergence study. The mesh is significantly more dense in areas where large gradients are expected and near cylinder and wall surfaces, as illustrated in Figure 4.1 and Figure 4.2. Special care is taken to ensure an acceptable y^+ value for the use of turbulent wall functions; an initial cell height of approximately $0.0005D$ is found to yield y^+ values of roughly $30 \sim 60$ for the cylinder surface, whilst a slightly higher initial layer is applied to the bottom wall where flow velocity is lower as a consequence of the logarithmic inlet flow profile.

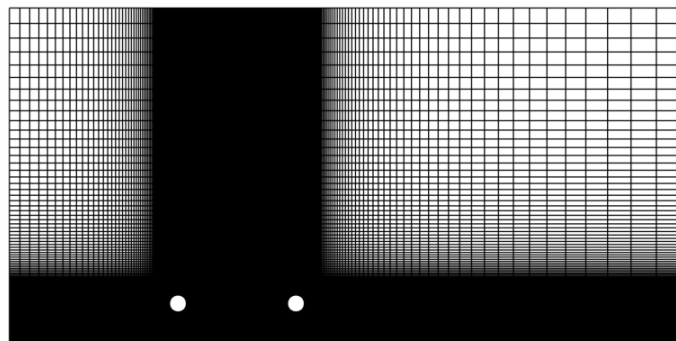


Figure 4.1: Mesh of tandem cylinders.

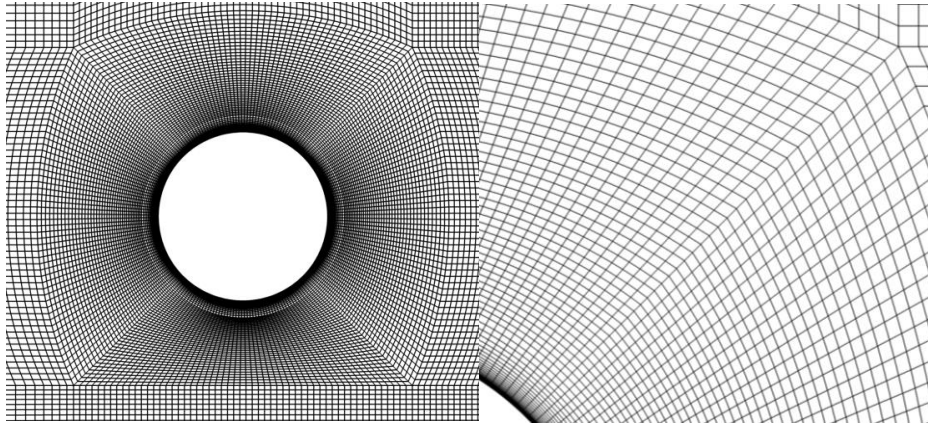


Figure 4.2: Upstream cylinder and close-up of radial cell distribution.

4.2 Model description

A schematic of the computational domain is provided in Figure 4.3. Partial derivatives with respect to n indicate the direction normal to the boundary. The domain is a two-dimensional rectangular shaped box of size $40D \times 20D$, where D is the diameter of the cylinder.

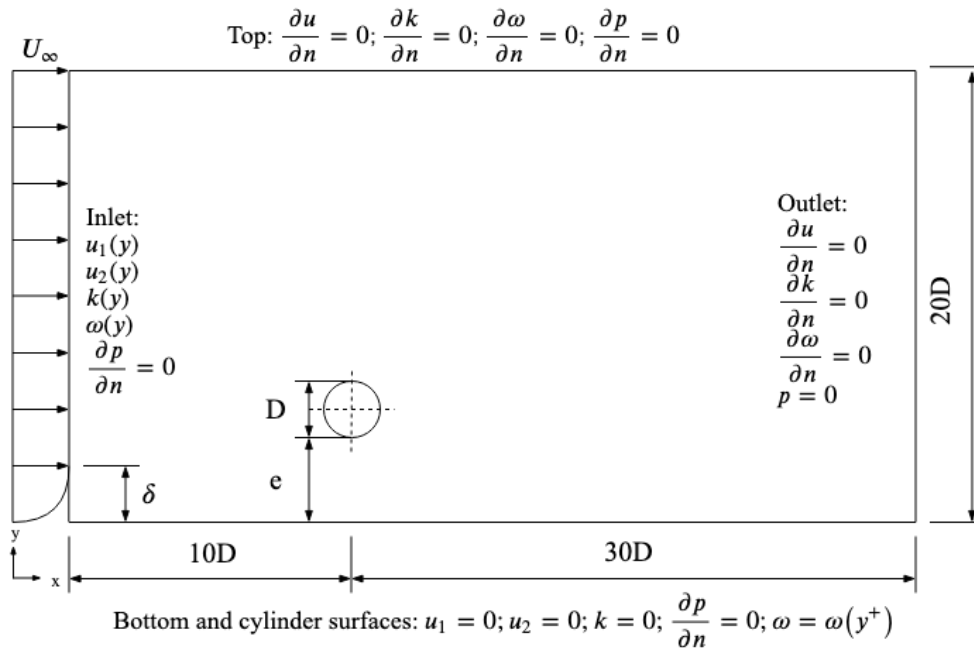


Figure 4.3: Schematic of computational domain for single static cylinder, given in terms of cylindrical diameter, D .

Flow direction is from left to right. The cylinder is positioned $10D$ downstream from the inlet and $30D$ upstream from the outlet, at a vertical gap e from the fixed bottom wall. The domain width is similar to that of numerical studies for tandem which has been proven sufficiently

large to minimize the effects of the boundaries. Bhattacharyya and Dhinkaran (2008) used a domain of $48D$ streamwise and $10D$ crossflow, with upstream cylinder positioned at distance $8D$ from the inlet. Harichandan and Roy (2012) used a domain of $40D$ streamwise and $15D$ crossflow, and Abrahamsen Prsic et al (2015) $40D \times 11.5D$. The latter two studies both had upstream cylinders positioned at $10D$ downstream of the inlet.

Boundary conditions can be summarized as follows:

- (i) The inflow at the inlet follows a logarithmic flow profile with boundary layer thickness $\delta/D = 0.48$, and is specified using the following expressions for k , u and ω :

$$u_1(y) = \min \left\{ \frac{u_*}{k} \ln \left(\frac{y}{z_w} \right), U_\infty \right\} \quad (4.1)$$

$$u_2(y) = 0 \quad (4.2)$$

$$k(y) = \max \left\{ C_\mu^{-\frac{1}{2}} \left(1 - \frac{y}{\delta} \right)^2 u_*^2, 0.0001 U_\infty^2 \right\} \quad (4.3)$$

$$\omega(y) = \frac{k(y)^{\frac{1}{2}}}{\beta^{*\frac{1}{4}} \ell(y)} \quad (4.4)$$

$$\ell(y) = \min \left\{ \kappa y \left(1 + 3.5 \frac{y}{\delta} \right)^{-1}, C_\mu \delta \right\} \quad (4.5)$$

where y is the direction normal to the bottom wall; $u_* = \kappa U_\infty / \ln(\delta/z_w)$ is the friction velocity in which $\kappa = 0.41$ is the von Kármán constant and $z_w = 1 \times 10^{-6}$ is the surface roughness; ℓ is an estimate of the turbulent length scale; $C_\mu = 0.09$ is a turbulence model constant, and U_∞ is the freestream velocity.

- (ii) The downstream outlet is prescribed a “zero-gradient” condition for u_1 , u_2 , k , and ω , meaning fluxes and normal stresses (partial derivatives) are set to zero. The pressure at the outlet is assigned a constant value of zero.
- (iii) The cylinder surface and the fixed bottom wall are assigned the no-slip condition; $u_1 = u_2 = 0$.
- (iv) The top boundary is set to “symmetry”, meaning normal components of u , k and ω are set to zero.

- (v) k-omega SST turbulence wall functions are applied to k and ω near the bottom and the cylinder surface;

$$k = \frac{u_*^2}{C_\mu^{\frac{1}{2}}} \quad (4.6)$$

$$\omega = \frac{1}{C_\mu^{\frac{4}{3}} \kappa h_p} \quad (4.7)$$

where h_p is the distance to the center of the first cell away from the wall, and u_* is the wall-friction velocity obtained from the log-law:

$$\frac{u_{tan}}{u_*} = \frac{1}{\kappa} \ln\left(\frac{h_p}{z_w}\right) \quad (4.8)$$

in which u_{tan} is the flow velocity tangent to the wall.

4.3 Convergence study

A convergence study is carried out to determine if the spatial and temporal discretization is sufficient to ensure a mesh independent solution. Investigations are carried out for four meshes of different density, with cell counts increasing by a constant refinement factor of 1.4 ~ 1.5. The geometric similarity of the meshes is preserved through the consecutive refinements. Mesh properties are presented in Table 4.1. The average values of y^+ for both the cylinder surface and the bottom fall within the range of application for turbulent wall functions ($30 \leq y^+ \leq \sim 300$). Time step sensitivity is evaluated via the Courant number. Courant number is defined as $Co = U\Delta T/\Delta x$, with the Courant condition of $Co \leq 1$. The PIMPLE solver can be set to automatically adjust timesteps to a maximum allowable value whilst still making sure the condition is met. In the study of Janocha (2018), a maximum Courant of $Co_{max} = 0.5$ was shown to be sufficient for 2DoF VIV simulations. This value is adopted with confidence that it yields more than sufficient temporal discretization for a static case.

Table 4.1: Parameters of convergence study meshes for single static cylinder.

Mesh	No. Cells	y_{avg}^+	
		Cylinder	Bottom
CS.S.S1	20 738	63.7	65.7
CS.S.S2	30 681	52.6	48.9
CS.S.S3	43 963	41.3	39.3
CS.S.S4	64 164	34.1	32.2

VIV is a consequence of drag- and lift fluctuations caused by vortex shedding, and as such, drag (C_D) and lift (C_L) coefficients are evaluated for the different meshes. The built-in `forceCoeffs` function is used to continuously extract coefficient data from the cylinder surfaces, and the mean ($\overline{C_D}$, $\overline{C_L}$) and root-mean-square (RMS) values (C_D^{rms} , C_L^{rms}) are obtained by:

$$\overline{C_D} = \frac{1}{n} \sum_{i=1}^n C_{D,i} \quad (4.9)$$

$$\overline{C_L} = \frac{1}{n} \sum_{i=1}^n C_{L,i} \quad (4.10)$$

$$C_D^{rms} = \sqrt{\frac{1}{n} \sum_{i=1}^n (C_{D,i} - \overline{C_D})^2} \quad (4.11)$$

$$C_L^{rms} = \sqrt{\frac{1}{n} \sum_{i=1}^n (C_{L,i} - \overline{C_L})^2} \quad (4.12)$$

The resulting hydrodynamic quantities are presented in Table 4.2, with a percentage comparison relative to mesh CS.S.S4. Simulations are run for $\tau = 300$ non-dimensional time, where $\tau = tU/D$. After roughly $\tau = 15$ the oscillating hydrodynamic force coefficients converge, meaning there is a negligible change in minimum, maximum and mean values following this timestep. For all convergence test simulations, the Reynolds number is set to $Re = 3.6 \times 10^6$, with gap ratio and boundary layer thickness at $G^* = 1$ and $\delta = 0.48$, respectively.

Table 4.2: Convergence study: single static cylinder, effects of mesh density. Simulated at Reynolds number 3.6×10^6 and gap ratio $G^* = 1$.

Mesh	$\overline{C_D}$	$\overline{C_L}$	C_L^{rms}	St
CS.S.S1	0.47970 (9.86%)	0.051214 (13.1%)	0.13143 (5.80%)	0.32119 (-9.11%)
CS.S.S2	0.45506 (4.98%)	0.046949 (5.22%)	0.12438 (0.46%)	0.33590 (-4.33%)
CS.S.S3	0.43636 (0.90%)	0.044778 (0.62%)	0.12061 (-2.64%)	0.34593 (-1.31%)
CS.S.S4	0.43240 (-)	0.044498 (-)	0.12380 (-)	0.35045 (-)

Mesh selection is a compromise of accuracy and computational cost, and to this end, mesh CS.S.S3 is selected for further work. Mean drag and lift coefficients show less than 1 % disparity to CS.S.S4. Strouhal number is in acceptable agreement with a relative error of 1.31 %. RMS lift has a slightly higher deviation but is accepted due to the variable being very sensitive to change in mesh density.

4.4 Model validation

The static simulation results are compared with similar studies in the upper transition regime around $Re = 3.6 \times 10^6$. Numerically, Ong et al. (2010) and Janocha (2018) investigated flow around cylinders at $Re = 3.6 \times 10^6$, $G^* = 1$, and $\delta = 0.48$. Ong et al. (2010) used a $k - \epsilon$ model, Janocha (2018) used a $k - \omega$ SST model. Isolated cylinders were investigated using $k - \epsilon$ model by Ong et al. (2009) and URANS LES by Catalano et al. (2003), albeit the former used a slightly higher Reynolds number, at $Re = 4.0 \times 10^6$. The numerical results are summarized in Table 4.3.

Table 4.3: Model validation: numerical results of present study and similar works in the upper transition regime.

Author	Description	Model	$\overline{C_D}$	$\overline{C_L}$	C_L^{rms}	St
Present study	$Re = 3.6 \times 10^6$, $G^* = 1$, $\delta/D = 0.48$	$k - \omega$ SST URANS	0.436	0.0448	0.121	0.356
Janocha (2018)	$Re = 3.6 \times 10^6$, $G^* = 1$, $\delta/D = 0.48$	$k - \omega$ SST URANS	0.461	0.0404	0.169	0.347
Ong et al. (2010)	$Re = 3.6 \times 10^6$, $G^* = 1$, $\delta/D = 0.48$	$k - \epsilon$ URANS	0.4608	0.0364	0.0766	0.3052
Ong et al. (2009)	$Re = 3.6 \times 10^6$; Isolated cylinder.	$k - \epsilon$ URANS	0.4573	-	0.0766	0.3052
Catalano et al. (2004)	$Re = 4.0 \times 10^6$; Isolated cylinder.	LES URANS	0.46	-	-	~ 0.35

The average drag coefficient is slightly underestimated in comparison to other studies, and the average lift coefficient appears to be slightly overestimated. RMS lift value is in between the studies of Ong et al. (2009, 2010) and Janocha (2018). Strouhal number is in a good agreement with Janocha (2018) and Catalano et al. (2004).

5 VORTEX-INDUCED VIBRATIONS OF TANDEM CYLINDERS

The present chapter describes the development process of the single static cylinder case to incorporate 2DoF motions and include a second cylinder. An updated model is described, and a mesh sensitivity is carried out for the modified case setup.

5.1 Grid generation

The mesh layout is similar to that presented in Section 4.2. A second cylinder is introduced at a distance L downstream using the same mesh distribution parameters, and the gap ratio is increased to avoid possible impact with the wall. At very small distances between the cylinder and the bottom wall the results may be compromised due to severe mesh deformations. The maximum expected amplitude of oscillation is approximately $1.2D$. The minimum gap ratio of $G^* = 1.5$ was selected in order to avoid contact with the bottom boundary.

5.2 Model description

A second cylinder is positioned at a distance L downstream of the first cylinder. Both cylinders have equal diameters. Displacement is restricted to in-line and crossflow motion. A schematic of the computational domain is provided in Figure 5.1.

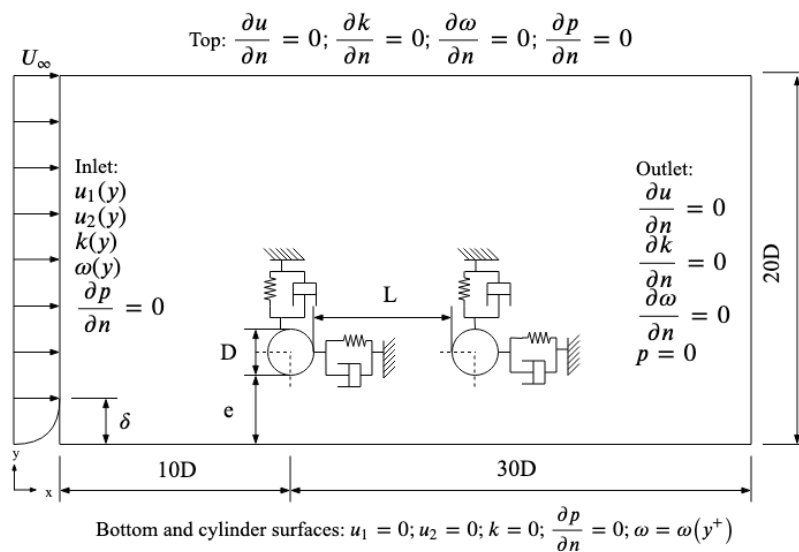


Figure 5.1: Schematic of the computational domain for tandem cylinder setup.

The schematic follows the same nomenclature as the schematic for the single static cylinder (Figure 4.3). The spring stiffness is adjusted to change the natural frequency (f_n) of the cylinders which governs the reduced velocity (U_r). The mass ratio is kept constant for all simulations at $m^* = 10$ and damping ratio $\zeta = c/2\sqrt{km}$ (where c is structural damping and k and m is spring stiffness and mass of cylinder) is set to zero to force large vibration amplitudes. Reynolds number based on diameter, freestream velocity U_∞ and kinematic viscosity ν is constant at $Re = 3.6 \times 10^6$. Inlet, outlet, top and bottom boundary conditions are identical to the static cylinder case.

5.3 Convergence study

The grid sensitivity study is performed at reduced velocity $U_r = 6$. It was found that for $U_r = 4$ and $U_r = 5$ the cylinder vibration is experiencing intermittent switching between the upper and lower branch. This switching mechanism is responsible for the chaotic and random nature of the oscillations and forces. In order to gather the representative statistics for the hydrodynamic quantities of interest the simulation time required for obtaining the statistically steady response was found to be unreasonably long. Instead, the simulations are carried out at $U_r = 6$ corresponding to the lower branch of lock-in, where the vibration amplitudes are still high but the response is more regular compared to that at $U_r = \{4, 5\}$. Gap ratio is increased to $G^* = 2$, and cylinder spacing is set to $L^* = 4$. A summary of the dimensionless parameters is provided in Table 5.1. A summary of the meshes used in the sensitivity test is presented in Table 5.2. Simulation time in non-dimensional time is set to $\tau = 300$ with maximum Courant number $Co_{max} = 0.5$.

Table 5.1: Dimensionless parameters applied for convergence study of VIV for 2DoF tandem cylinders.

Parameter		Value
Reynolds number	Re	3.6×10^6
Gap ratio	G^*	2
Cylinder spacing	L^*	4
Reduced velocity	U_r	6
Normalized boundary layer thickness	δ/D	0.48
Mass ratio	m^*	10

Table 5.2: Parameters of convergence study meshes for 2DoF tandem cylinders.

Mesh	No. cells
CS.T1	40 559
CS.T2	59 946
CS.T3	86 018
CS.T4	125 861

Additional parameters are investigated for the dynamic simulations. The maximum vertical and RMS dimensionless horizontal vibration amplitudes are given as:

$$\frac{(A_y)_{max}}{D} = \frac{1}{2} \frac{|(A_y)_{max} - (A_y)_{min}|}{D} \quad (5.1)$$

$$\frac{(A_x)_{rms}}{D} = \frac{1}{n} \sqrt{\sum_{i=1}^n (A_{x,i} - \bar{A}_x)^2} \quad (5.2)$$

Results for upstream and downstream cylinders are presented in Table 5.3 and Table 5.4, respectively.

Table 5.3: Convergence study: Upstream 2DoF cylinder, effects of mesh density. Simulated at Reynolds number 3.6×10^6 , gap ratio $G^* = 2$, and cylinder spacing $L^* = 4$.

Mesh	\bar{C}_D	C_L^{rms}	$A_{y,max}/D$	$A_{x,rms}/D$	St
CS.T1	1.05561 (8.65%)	0.46088 (29.3%)	1.04687 (-4.50%)	0.31874 (8.34%)	0.15895 (-2.64%)
CS.T2	1.08469 (11.1%)	0.72371 (17.6%)	1.15984 (5.67%)	0.30518 (4.27%)	0.15495 (-5.29%)
CS.T3	0.98282 (1.88%)	0.70101 (15.0%)	1.13866 (3.92%)	0.29486 (0.93%)	0.16475 (0.97%)
CS.T4	0.96429 (-)	0.59598 (-)	1.09398 (-)	0.29213 (-)	0.16315

Table 5.4: Convergence study: Downstream 2DoF cylinder, effects of mesh density. Simulated at Reynolds number 3.6×10^6 , gap ratio $G^* = 2$, and cylinder spacing $L^* = 4$.

Mesh	\bar{C}_D	C_L^{rms}	$A_{y,max}/D$	$A_{x,rms}/D$	St
CS.T1	1.00624 (6.99%)	0.82988 (7.84%)	1.10879 (-0.35%)	0.26706 (4.07%)	0.15785 (3.04%)
CS.T2	1.01009 (7.35%)	0.68306 (-11.9%)	1.13276 (0.18%)	0.29500 (13.2%)	0.15950 (-1.97%)
CS.T3	0.94278 (0.73%)	0.78424 (2.48%)	1.17423 (5.24%)	0.25282 (-1.32%)	0.16105 (-0.99%)
CS.T4	0.93585 (-)	0.76476 (-)	1.11269 (-)	0.25617 (-)	0.16265 (-)

The difference in results for mesh CS.T3 and CS.T4 are low enough to accept CS.T3 for further work. Upstream RMS lift obtained from simulations on mesh CS.T4 differs by 15 % compared to the results obtained on mesh CS.T3. This variable proved to be very sensitive to mesh density changes, as evidenced in Table 4.2, Table 5.3 and Table 5.4. Simulations would require

significantly longer simulation time for C_L^{rms} to reach a statistically steady state, and at that point, nonlinear interactions could still disturb the quantities. The remaining parameters for mesh CS.T3 show variability of approximately ~5 % or less when comparing mesh CS.T3 to the highest density mesh CS.T4. The results from the mesh sensitivity study reaffirm the selection of mesh CS.T3 as appropriate for conducting further numerical simulations.

6 RESULTS AND DISCUSSION

For 2DoF tandem near-wall cylinders, the following parameters are investigated: $G^* = \{1.5, 2\}$, $L^* = \{4, 5, 6\}$ at $U_r = \{4, 5\}$ for Reynolds number $Re = 3.6 \times 10^6$. The mass ratio is kept constant at $m^* = 10$ and the damping ratio is set to $\zeta = 0$. Hydrodynamic coefficients, amplitude ratios, motion trajectories, flow fields, and vibration frequency are all investigated and presented for the different test parameters. Up- and downstream cylinders are denoted with indices UC and DC, respectively.

6.1 Hydrodynamic forces

The mean drag and lift coefficients, $\overline{C_D}$, $\overline{C_L}$, and the RMS lift coefficient C_L^{rms} are calculated for both upstream and downstream cylinders for all the investigated cases. A summary of hydrodynamic coefficients is presented in Table 6.1 and time series with corresponding displacements are provided in Appendix A. Hydrodynamic coefficients for both cylinders at $L^* = 4$ for different reduced velocity and gap ratio is presented in Figure 6.1. The time-averaged drag coefficient in Figure 6.1 a) is lower for the downstream cylinder due to the shielding effect. Additionally, vortices shed from the upstream cylinder create low pressure in the wake, further contributing to a lower drag coefficient. Shielding effects are more prominent with decreasing cylinder spacing. This can be seen in Figure 6.2. $\overline{C_{D,DC}}$ is smaller than the $\overline{C_{D,UC}}$ for all investigated configurations (Table 6.1) except for $U_r = 5, G^* = 1.5, L^* = 6$ where $\overline{C_{D,DC}}$

Table 6.1: Mean drag and RMS lift coefficients for $U_r = \{4, 5\}$, $G^* = \{1.5, 2\}$ and $L^* = \{4, 5, 6\}$.

Reduced velocity	Gap ratio	Cylinder spacing	Upstream cylinder			Downstream cylinder		
			$\overline{C_D}$	$\overline{C_L}$	C_L^{rms}	$\overline{C_D}$	$\overline{C_L}$	C_L^{rms}
$U_r = 4$	$G^* = 1.5$	$L^* = 4$	1.36961	0.16945	1.33365	1.11580	0.24715	1.61438
		$L^* = 5$	1.39758	-0.18949	1.60750	1.23995	0.13602	1.32352
		$L^* = 6$	1.32702	-0.34188	1.52448	1.15627	0.07422	1.63637
	$G^* = 2$	$L^* = 4$	1.29778	-0.04350	1.50032	1.22378	0.04939	1.60593
		$L^* = 5$	1.28972	-0.21225	1.67592	1.21673	0.02566	1.54802
		$L^* = 6$	1.29913	-0.35640	1.63266	1.24288	-0.18823	1.57252
$U_r = 5$	$G^* = 1.5$	$L^* = 4$	1.12053	-0.21682	0.95575	0.87471	0.09540	1.18682
		$L^* = 5$	1.15541	-0.27448	1.01543	1.01856	0.42386	1.17858
		$L^* = 6$	1.11137	-0.27987	1.04630	1.14427	0.06735	1.01378
	$G^* = 2$	$L^* = 4$	1.25040	-0.07793	0.95575	0.87471	-0.13917	0.83363
		$L^* = 5$	1.11780	-0.26861	0.97480	0.99270	0.41802	1.00002
		$L^* = 6$	1.13117	-0.27541	1.04858	1.05133	0.27702	0.93934

is slightly larger than upstream. $\overline{C_D}$ is decreasing with increasing U_r for all considered configurations. Gap ratio does not have a significant effect on $\overline{C_D}$, as can be seen in Table 6.1 and Figure 6.2. Negligible change in $\overline{C_D}$ from wall effects at $G^* = \{1.5, 2\}$ is also observed in Tang et al. (2015) and Sumer and Fredsøe (2006). In Figure 6.1 b) it can be seen that C_L^{rms} for $L^* = 4$ is decreasing with increasing U_r . The same is true for $L^* = 5$ and $L^* = 6$. When the cylinders are closer to the bottom boundary, the shear layers of the cylinder are interfering with the bottom wall boundary layer and therefore the separated shear layers from the cylinder exhibit reduced vorticity magnitudes. This effect results in non-zero mean lift $\overline{C_L}$. Negative values indicate that the force is acting in the direction of the bottom wall, which is the case for all upstream cylinders except for $U_r = 4, G^* = 1.5, L^* = 4$. Generally little difference is found in $\overline{C_{L,UC}}$ between the configurations at gap ratios $G^* = 1.5$ and $G^* = 2$, except for the case where $L^* = 4$, as shown in Figure 6.3. $\overline{C_{L,DC}}$ is strongly influenced by the wake of the upstream cylinder as is evidenced by $\overline{C_{L,UC}}$ values summarized in Table 6.1.

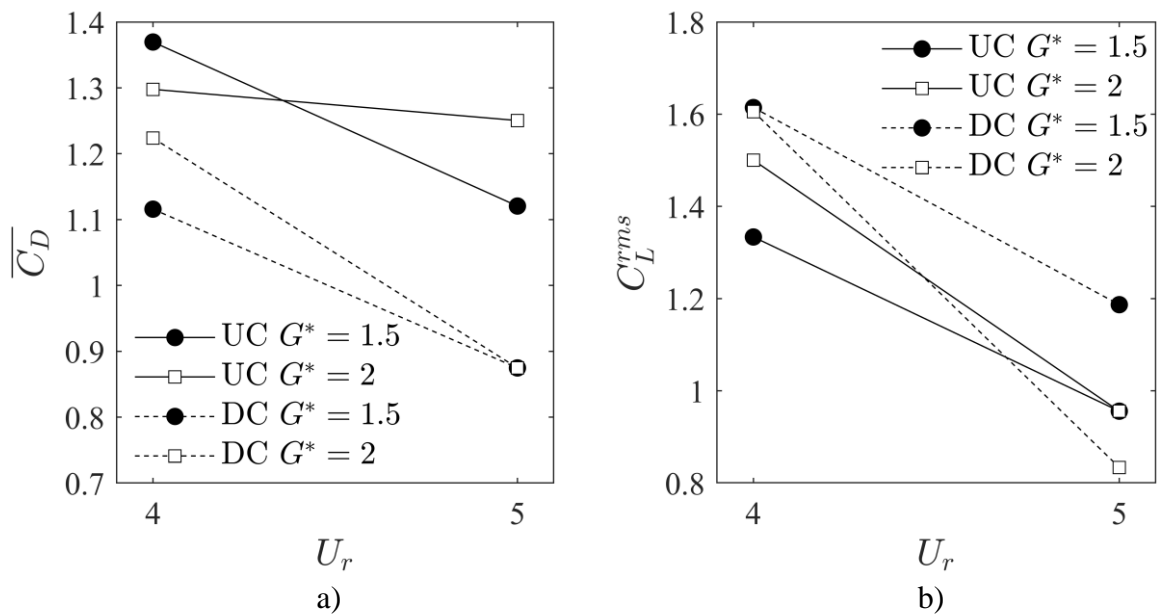


Figure 6.1: a) $\overline{C_D}$ and b) C_L^{rms} for up- and downstream cylinders at $G^* = \{1.5, 2\}$ and $U_r = \{4, 5\}$ for cylinder spacing $L^* = 4$.

The time series of the hydrodynamic coefficients are irregular for the investigated range of reduced velocity. Beating oscillations of C_L are observed in all investigated cases. They are characterized by a gradual buildup of C_L amplitude, followed by a sharp decrease, and then a new cycle starts. Time series of hydrodynamic coefficients and normalized transverse (y/D) and streamwise (x/D) displacements are presented in Figure 6.4 and Figure 6.5 for the upstream cylinder at $U_r = 5, G^* = 1.5, L^* = 4$.

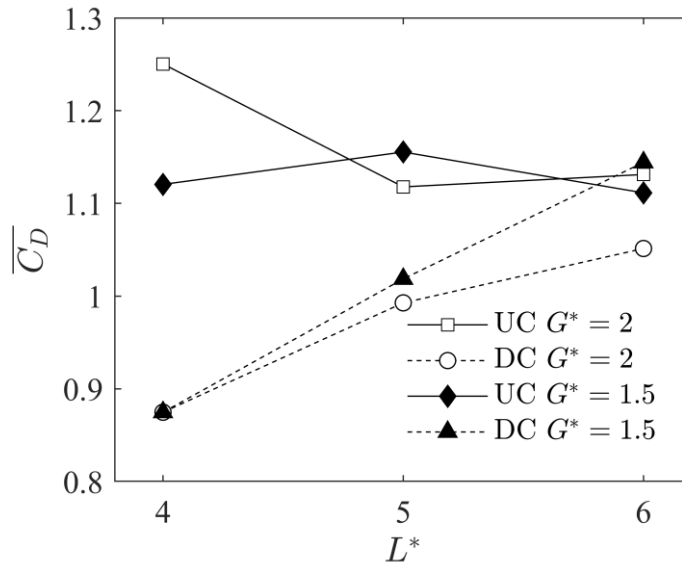


Figure 6.2: $\overline{C_D}$ at $U_r = 5$ for up- and downstream cylinders at different cylinder spacing and gap ratio.

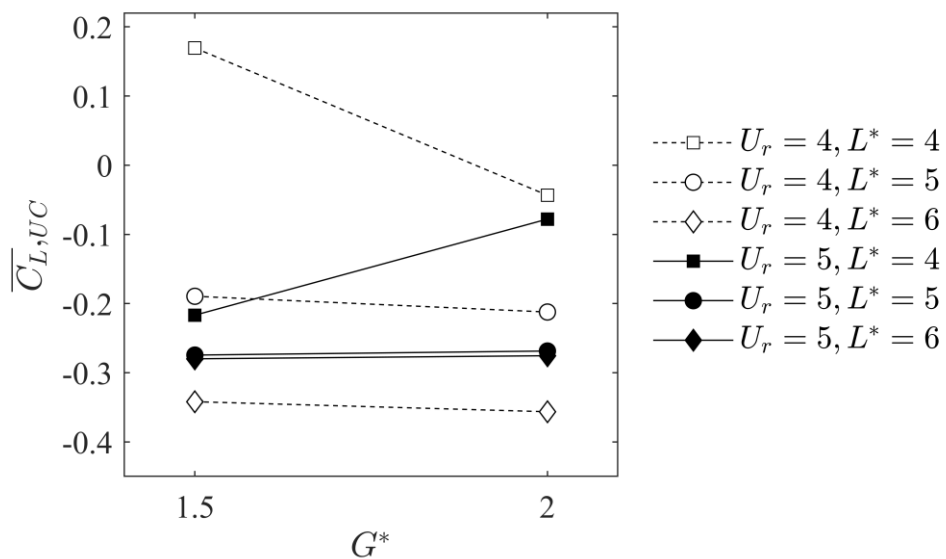


Figure 6.3: $\overline{C_{L,UC}}$ for different gap ratios.

In Figure 6.4, periods with large C_L spikes are observed at $\tau = \sim 75, \sim 125, \sim 225, \sim 290$, as indicated by dashed squares. The corresponding streamwise oscillation magnitudes are approaching a local minima following these time instances. In Figure 6.5 the same configuration is plotted with a shorter timespan ($\tau = [100, 170]$) to provide a better look at the

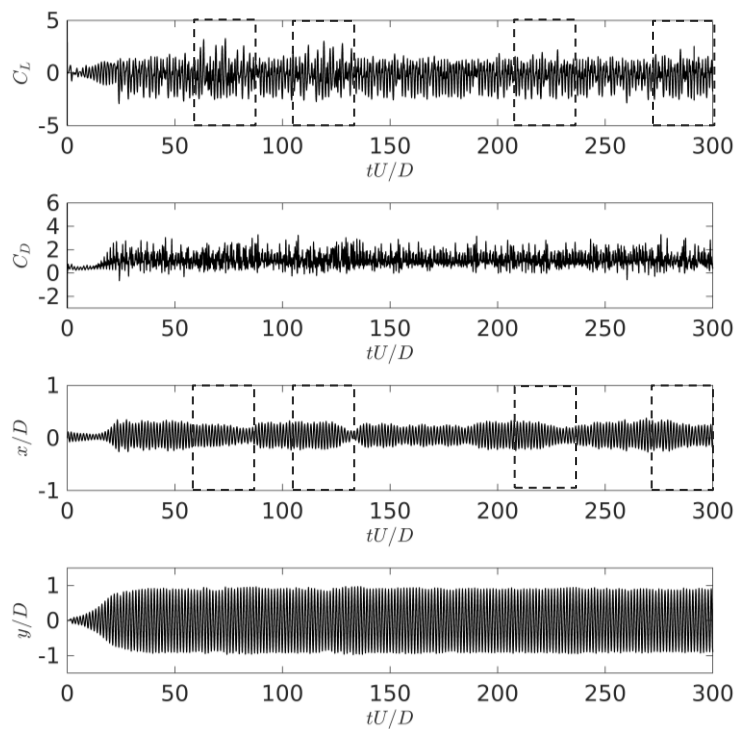


Figure 6.4: Hydrodynamic coefficients and displacements for upstream cylinder at $\tau = [0,300]$, $U_r = 5$, $G^* = 1.5$, $L^* = 4$. Periods of large C_L spikes are highlighted.

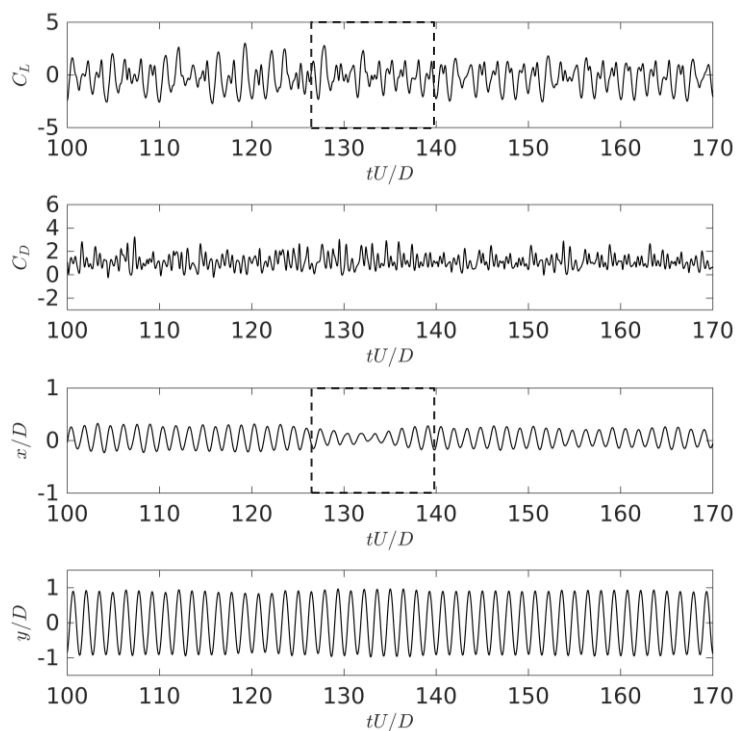


Figure 6.5: Hydrodynamic coefficients and displacements for upstream cylinder at $\tau = [100,170]$, $U_r = 5$, $G^* = 1.5$, $L^* = 4$. Transition from large spikes in C_L to a more regular pattern and corresponding reset of streamwise oscillation amplitude.

variations in $C_{L,UC}$ and x_{UC}/D . The fluctuations in lift are changing from a highly irregular pattern before streamwise oscillation magnitudes reach a minimum, to a more stable pattern when the vibration amplitudes are restored.

6.2 Response amplitudes

Maximum response amplitudes in streamwise ($A_{X,max}/D$) and transverse ($A_{Y,max}/D$) directions as well as RMS of streamwise amplitudes ($A_{X,rms}/D$) are recorded during simulations and are summarized in Table 6.2. The highest values of $A_{Y,max}/D$ for upstream and downstream cylinders are $A_{Y,max}^{UC}/D = 0.9891$ and $A_{Y,max}^{DC}/D = 1.1078$, and they are observed for the case at $U_r = 5$, $G^* = 1.5$, and $L^* = 6$. The highest recorded streamwise values are $A_{X,max}^{UC}/D = 0.509$ at $U_r = 5$, $G^* = 2$, $L^* = 4$ and $A_{X,max}^{DC}/D = 0.775$ at $U_r = 4$, $G^* = 2$, $L^* = 6$. The effect of gap ratio on transverse vibration amplitude is presented in Figure 6.6 a) and b) for up- and downstream cylinders, respectively. Figure 6.6 a) shows that simulations at $U_r = 5$ have higher $A_{Y,max}^{UC}/D$ than at $U_r = 4$. In all but one case ($U_r = 5$, $L^* = 6$) $A_{Y,max}^{UC}/D$ is increasing with increasing gap ratio, which is in agreement with the studies of Jacobsen et al. (1984) and Tang et al. (2015). The relative increase with gap ratio is larger for $U_r = 4$. Figure 6.6 shows that $A_{Y,max}^{DC}/D$ is also larger for higher reduced velocity. In contrast to the upstream cylinder, $A_{Y,max}^{DC}/D$ is decreasing with increasing G^* for all cases except $U_r = 4$, $L^* = 6$.

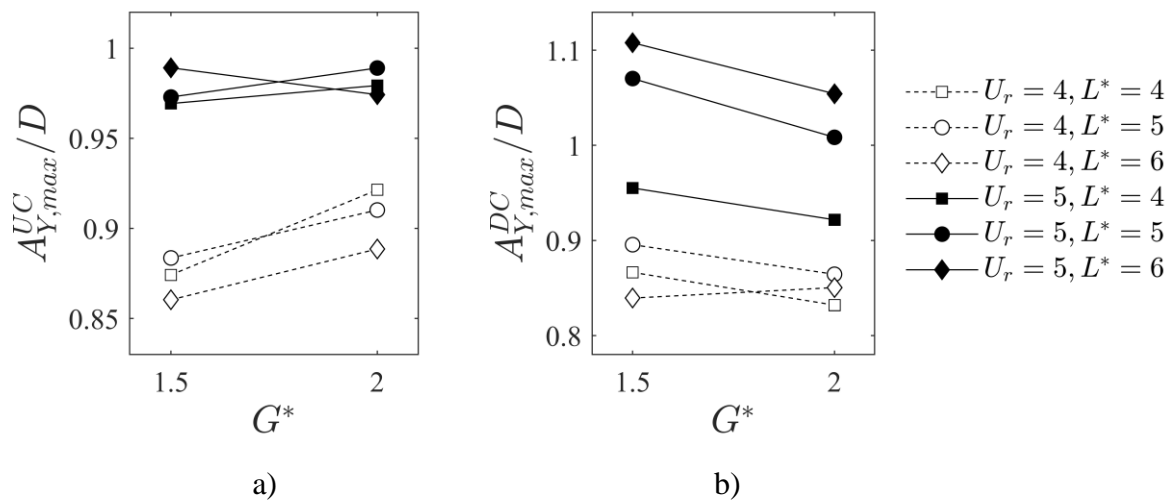


Figure 6.6: a) $A_{Y,max}^{UC}/D$ and b) $A_{Y,max}^{DC}/D$ for different gap ratios.

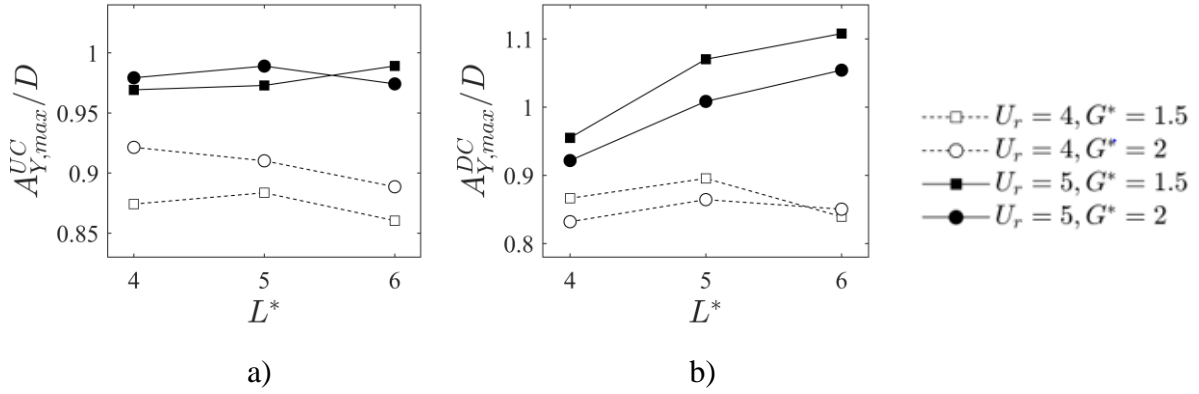


Figure 6.7: a) $A_{Y,max}^{UC}/D$ and b) $A_{Y,max}^{DC}/D$ with respect to cylinder spacing, L^* .

Figure 6.7 shows the effect of cylinder spacing on $A_{Y,max}/D$ for a) upstream cylinder and b) downstream cylinder. The maximum amplitudes for the upstream cylinder are not sensitive to changing the cylinder spacing and remain approximately constant for given U_r and G^* . The downstream cylinder $A_{Y,max}/D$ at $U_r = 5$ is characterized by a trend of increasing $A_{Y,max}/D$ with increasing cylinder spacing. Figure 6.8 present the maximum in-line vibration amplitudes for upstream ($A_{X,max}^{UC}/D$) and downstream ($A_{X,max}^{DC}/D$) cylinders with respect to G^* . A trend of increasing $A_{X,max}^{UC}/D$ with increasing G^* is observed for $U_r = 5$, whilst the remaining configurations do not exhibit much change with different G^* . The vibration amplitude magnitudes are larger for the downstream cylinders. This is in line with the findings of Kim et al. (2009) for tandem vibrating cylinders at $L^* \geq 2.7$. The reason for larger downstream magnitudes is the wake-induced effects caused by the vortices shed from the upstream cylinder which periodically impinges the downstream cylinder, increasing its in-line response. The increase in $A_{X,max}^{UC}/D$ with gap ratio is larger for $U_r = 5$ than for $U_r = 4$. A similar observation is made for $A_{X,max}^{DC}/D$, except for $U_r = 5, L^* = 4$. In Figure 6.9 $A_{X,max}/D$ is presented for different U_r values. $A_{X,max}^{UC}/D$ is increasing with U_r for $G^* = 2$, but decreasing with U_r for $G^* = 1.5$. As expected, cylinder spacing does not exhibit a distinct correlation with $A_{X,max}^{UC}/D$ magnitudes. $A_{X,max}^{DC}/D$ values are decreasing with increasing U_r except for $G^* = 1.5, L^* = 4$.

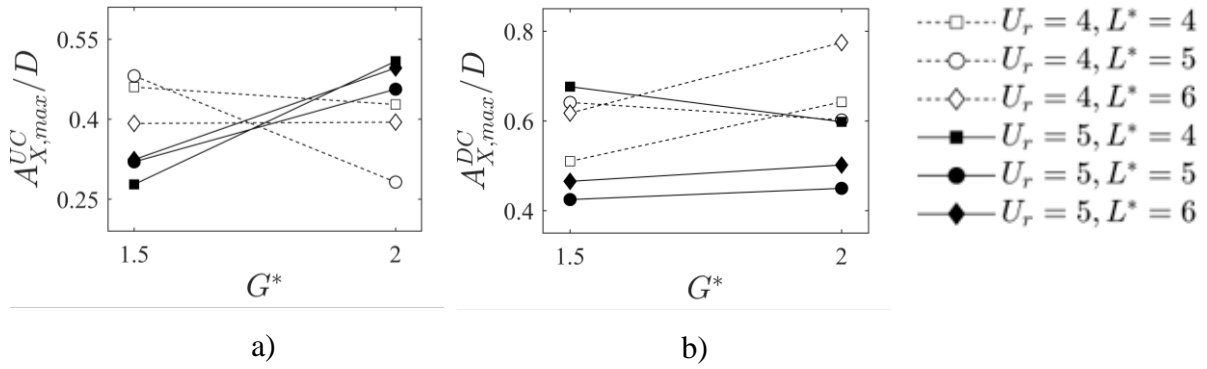
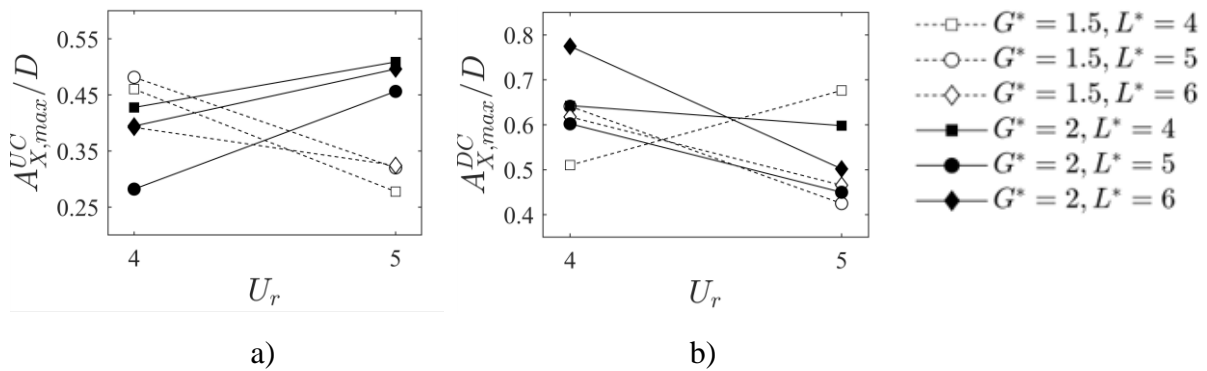

 Figure 6.8: a) $A_{X,max}^{UC}/D$ and b) $A_{X,max}^{DC}/D$ for different gap ratios.

 Figure 6.9: a) $A_{X,max}^{UC}/D$ and b) $A_{X,max}^{DC}/D$ for different reduced velocity.

 Table 6.2: Maximum response amplitudes for both transverse ($A_{Y,max}/D$) and streamwise ($A_{X,max}/D$) vibrations and inline RMS response ($A_{X,rms}/D$).

	$U_r = 4$				$U_r = 5$			
	$G^* = 1.5$		$G^* = 2$		$G^* = 1.5$		$G^* = 2$	
	Upst.	Downst.	Upst.	Downst.	Upst.	Downst.	Upst.	Downst.
Transverse ($A_{Y,max}/D$)								
$L^* = 4$	0.8742	0.8664	0.9214	0.8320	0.9693	0.9551	0.9793	0.9217
$L^* = 5$	0.8836	0.8955	0.9102	0.8644	0.9729	1.0702	0.9890	1.0084
$L^* = 6$	0.8604	0.8394	0.8886	0.8504	0.9891	1.1078	0.9742	1.0542
Streamwise ($A_{X,max}/D$)								
$L^* = 4$	0.4603	0.5101	0.4277	0.6426	0.2777	0.6764	0.5088	0.5982
$L^* = 5$	0.4814	0.6412	0.2821	0.6022	0.3201	0.4249	0.4563	0.4499
$L^* = 6$	0.3921	0.6176	0.3945	0.7748	0.3243	0.4655	0.4962	0.5019
Streamwise RMS ($A_{X,rms}/D$)								
$L^* = 4$	0.1999	0.2133	0.1614	0.3120	0.1506	0.3128	0.2959	0.2936
$L^* = 5$	0.1772	0.2776	0.1317	0.3163	0.1702	0.1992	0.2296	0.2320
$L^* = 6$	0.1454	0.3126	0.1611	0.3893	0.1683	0.2128	0.2660	0.2629

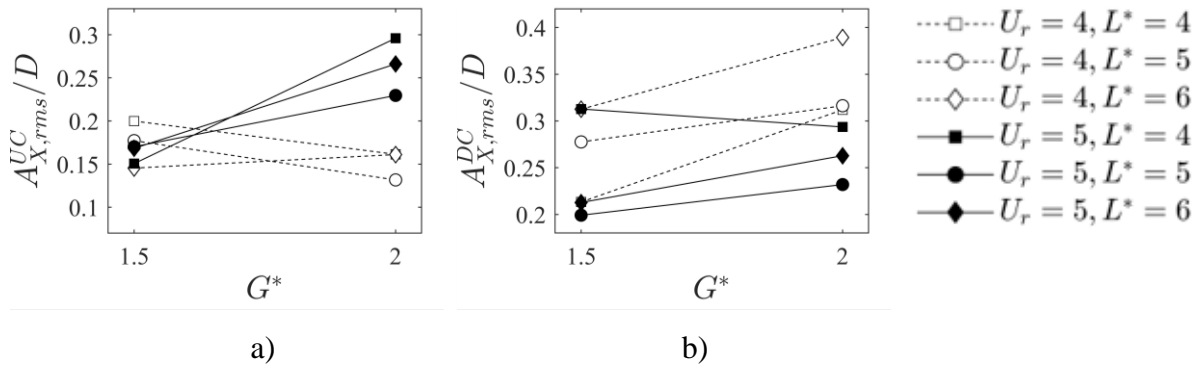


Figure 6.10: a) $A_{X,rms}^{UC}/D$ and b) $A_{X,rms}^{DC}/D$ for different gap ratios.

The RMS of streamwise vibration is presented in Figure 6.10. This value is of particular interest when considering the fatigue state of the cylinders. $A_{X,rms}^{UC}/D$ is increasing with increasing G^* for $U_r = 5$, but does not change with increasing G^* for $U_r = 4$. At $G^* = 1.5$ the upstream RMS amplitudes are closely clustered, but when gap ratio is increased, they branch out depending on the reduced velocity. Figure 6.11 presents $A_{X,rms}^{DC}/D$ for different L^* . $A_{X,rms}^{DC}/D$ appears to increase with cylinder spacing at $U_r = 4$, and remain somewhat stable at $U_r = 5$, suggesting that the downstream cylinder is more affected by the vortices in the wake of the upstream cylinder at the lower U_r . Maximum $A_{X,rms}^{UC}/D$ values are measured at the largest gap, $G^* = 2$.

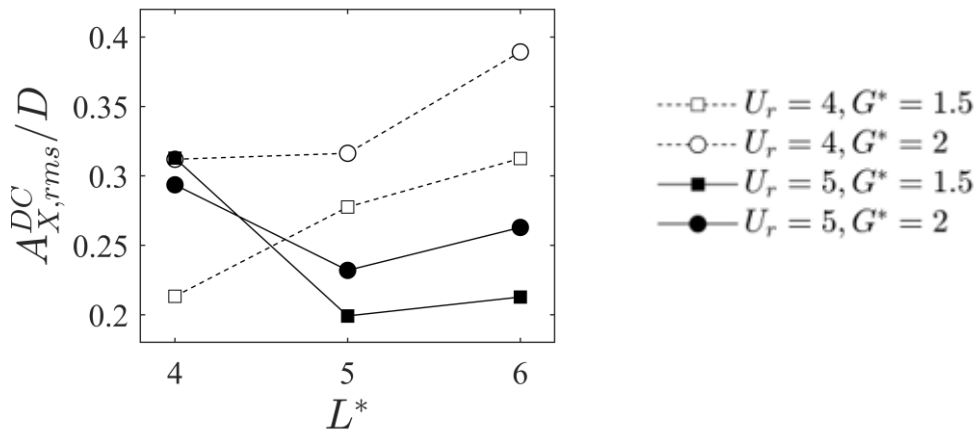


Figure 6.11: $A_{X,rms}^{DC}/D$ for different cylinder spacing.

6.3 Motion trajectories

The following subsection is dedicated to the analysis of the oscillation trajectories plotted on the $X - Y$ plane and phase pictures of lift coefficient C_L against transverse displacements Y/D . Appendix B presents motion trajectories for all investigated configurations. A cylinder exposed to a uniform current and free to vibrate in 2DoF will exhibit a characteristic motion trajectory

of a figure of eight. Due to the wall proximity effects, for the near-wall oscillating cylinder, this trajectory will be replaced by an oval trajectory. The reason of this change is the streamwise vibration lock-in. Therefore, the dominant frequency of vibration in crossflow and streamwise directions is approximately the same. Representative trajectories at different cylinder spacing for a period of $\tau = [50,150]$, $G^* = 2$, at reduced velocities $U_r = 4$ and $U_r = 5$ are shown in Figure 6.13 and Figure 6.14, respectively. Figure 6.13 shows very irregular motion trajectories for both up- and downstream cylinders at $L^* = 4$. A probability density plot of cylinder positions is presented in Figure 6.12 to emphasize the most frequent trajectories. Red color indicates that the cylinder frequently occupies this position, and blue color means it is less frequent. The remaining cylinders show a skewed oval trajectory which is typical for near-wall vibrating cylinders. The upstream cylinders in Figure 6.13 take on a more narrow trajectory than the downstream cylinders. This is because vortices are convected in the wake and intersect the downstream cylinder which enhances streamwise displacement. The most stable trajectories at $U_r = 4$, $G^* = 2$ are found at $L^* = 6$ for upstream, and $L^* = 5$ for downstream. When increasing reduced velocity to $U_r = 5$, the trajectories change significantly, as shown in Figure 6.14. The upstream cylinders take on a more oval shape because the streamwise vibration amplitudes are larger with increasing U_r , as presented in Figure 6.9 a) and Figure 6.10 a). The wake induced effects on the downstream cylinders are creating very irregular motions with some trajectories being closer to a circular pattern than the skewed oval. The most stable trajectory for $U_r = 5$ and $G^* = 2$ is found for $L^* = 4$ for both cylinders. A probability density plot of cylinder positions is provided in Figure 6.15 for downstream cylinders at $L^* = 5$ and $L^* = 6$.

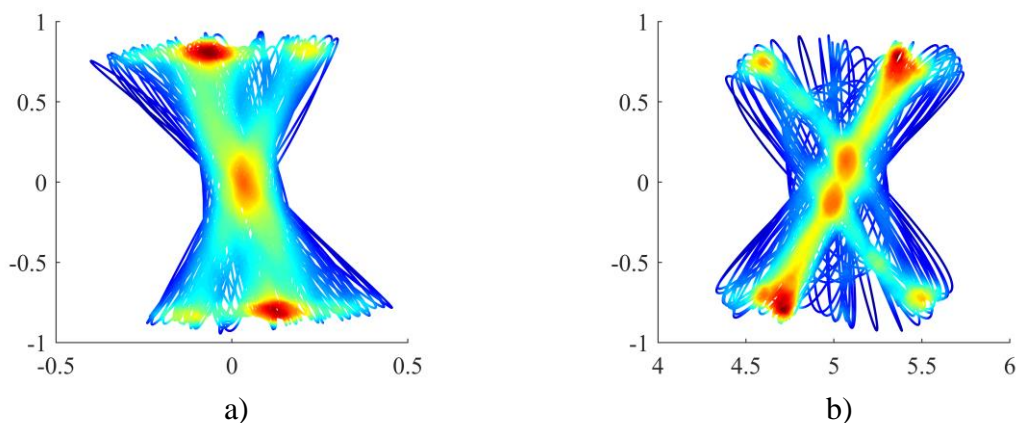


Figure 6.12: Probability density plots of cylinder positions at $U_r = 4$, $G^* = 2$, $L^* = 4$ for a) upstream cylinder, and b) downstream cylinder.

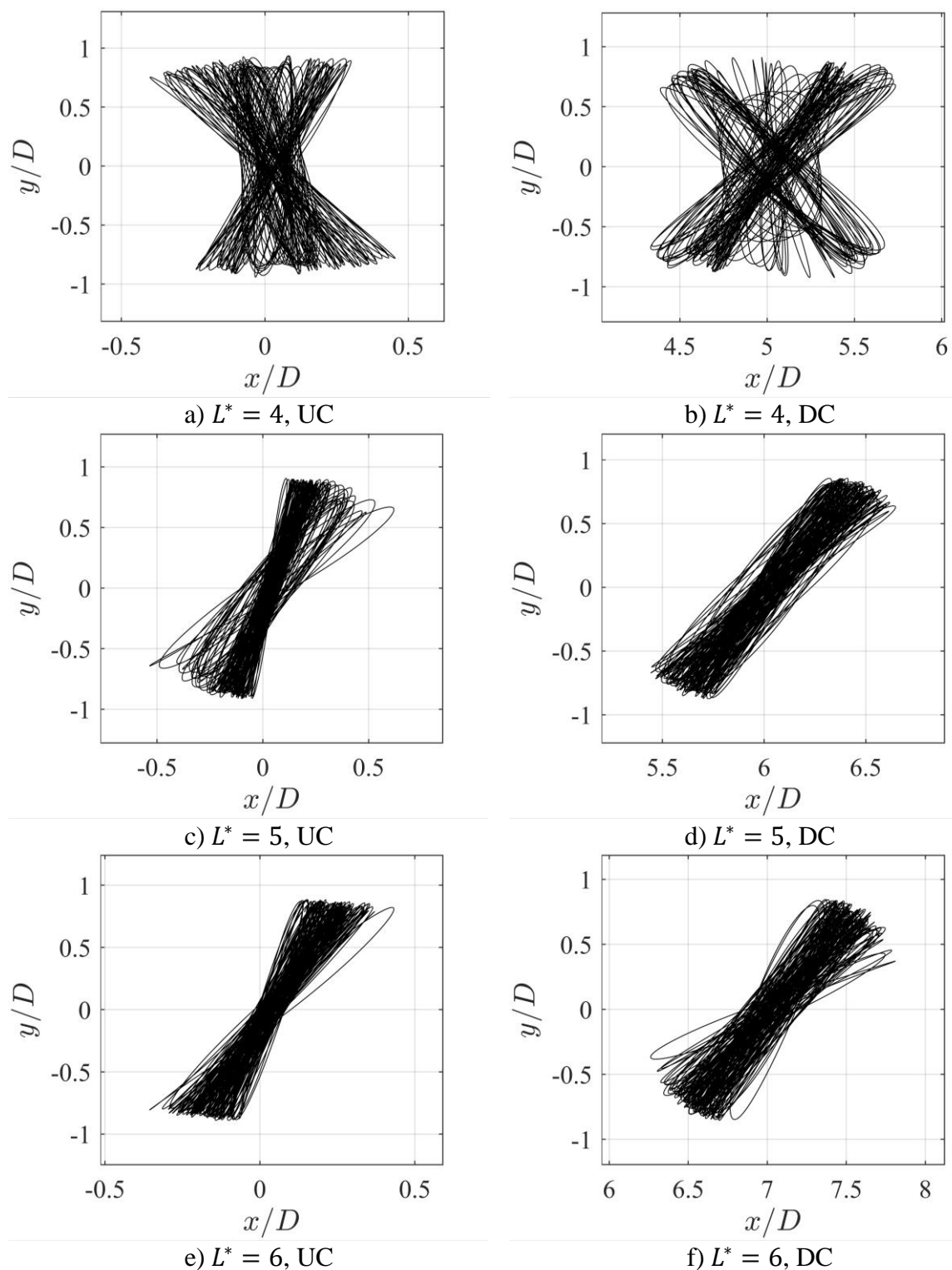


Figure 6.13: Motion trajectories in the $X - Y$ plane for cylinder spacing $L^* = [4, 5, 6]$ at $\tau = [50, 150]$ for $U_r = 4$, $G^* = 2$.

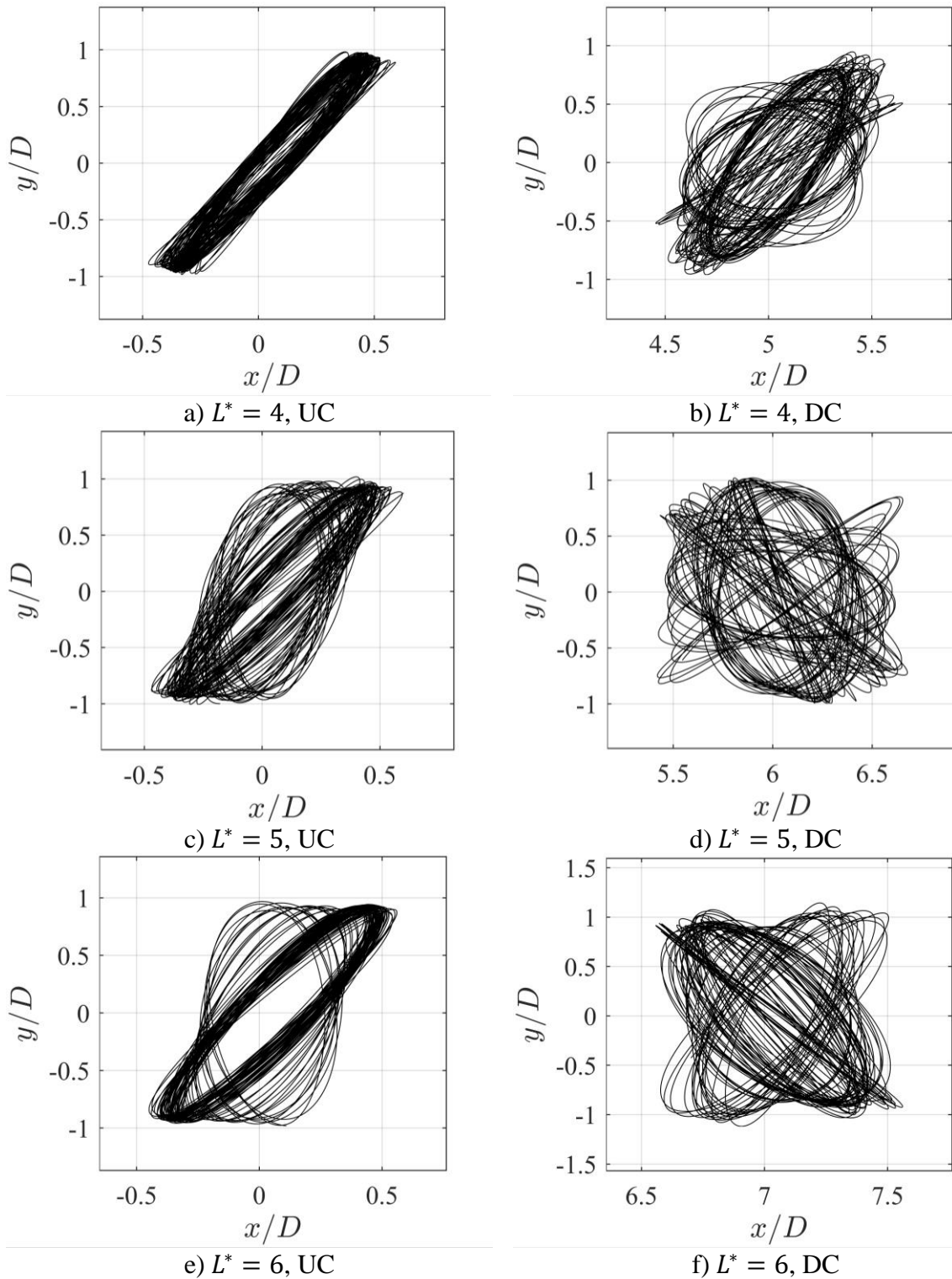


Figure 6.14: Motion trajectories in the $X - Y$ plane for cylinder spacing $L^* = [4, 5, 6]$ at $\tau = [50, 150]$ for $U_r = 5$, $G^* = 2$.

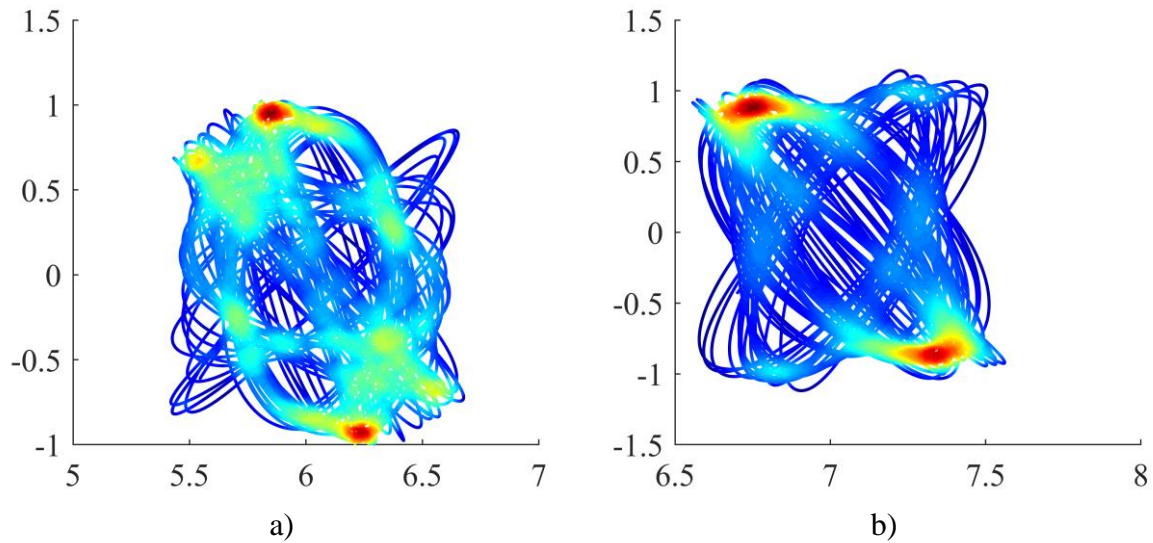


Figure 6.15: Probability density plots of cylinder positions for a) $U_r = 5, G^* = 2, L^* = 5$ and b) $U_r = 5, G^* = 2, L^* = 6$.

6.4 Flow fields

Vorticity and pressure contours are used to analyze the flow around the cylinders during one full vibration cycle. The evolution of vorticity and pressure at reduced velocity $U_r = 4, G^* = 1.5$ is presented in Figure 6.16. The phase difference between the transverse displacements is approximately π . The vortex shedding mode of the upstream cylinder is a 2P mode, in which a pair of vortices with opposing vorticity is shed at peak transverse vibration amplitudes. The top pair is convected laterally downstream past the freestream side of the second cylinder. The bottom pair impacts the wall which leaves a negative vorticity vortex hanging behind, effectively creating a zone of opposing vorticity around a newly formed positive vorticity vortex. This situation forces the positive vortex in an upwards direction and into the path of the cylinder downstream. The downstream cylinder also exhibits 2P shedding, however, the vortices are merging with inbound vortices from the upstream wake, and a single pair of two large vortices with opposing vorticity are seen in the wake of the tandem configuration. Figure 6.17 presents a cycle of vortex shedding at $U_r = 4$, gap ratio $G^* = 2$ and $L^* = 6$. The corresponding hydrodynamic coefficients and response amplitudes are shown in Figure 6.18 and Figure 6.19 for up- and downstream cylinders, respectively. Transverse displacements are in-phase. In this configuration triplets of vortices, characterized as 2T vortex shedding (Jauvits and Williamson, 2003), are being shed from the upstream cylinder. Figure 6.17 c) and d) show

that the downstream cylinder is being impinged by vortices from the upstream wake. The effect of the impingement is confirmed by the small transverse vibration amplitude of the downstream cylinder as presented in Figure 6.19. The downstream wake contains two large vortices of opposing sign, convected in the longitudinal direction and two smaller vortices convected laterally outwards. Figure 6.20 presents a shedding cycle at $U_r = 4, G^* = 2, L^* = 5$ in which upstream cylinder phase is shifted by approximately $\pi/2$. Vortices shed from the upstream cylinder can be classified as S+T, in which a single strong vortex is shed near the wall, and triplets are shed on the freestream side. At this phase difference, the near-wall single vortex is convected past the downstream cylinder and passes into the tandem wake without much interference. Similar observations are made for the triplets; the trajectory of the downstream cylinder is such that it avoids any serious impingements. Because the upstream vortices pass by the downstream cylinder relatively unhindered, the tandem wake is very chaotic, with several smaller vortices surrounding a pair or larger opposing vortices. Visual observations of all configurations confirm that the flow is in the impingement regime, classified as $L^* > 3.4 \sim 3.8$ by Zdravkovich (1987).

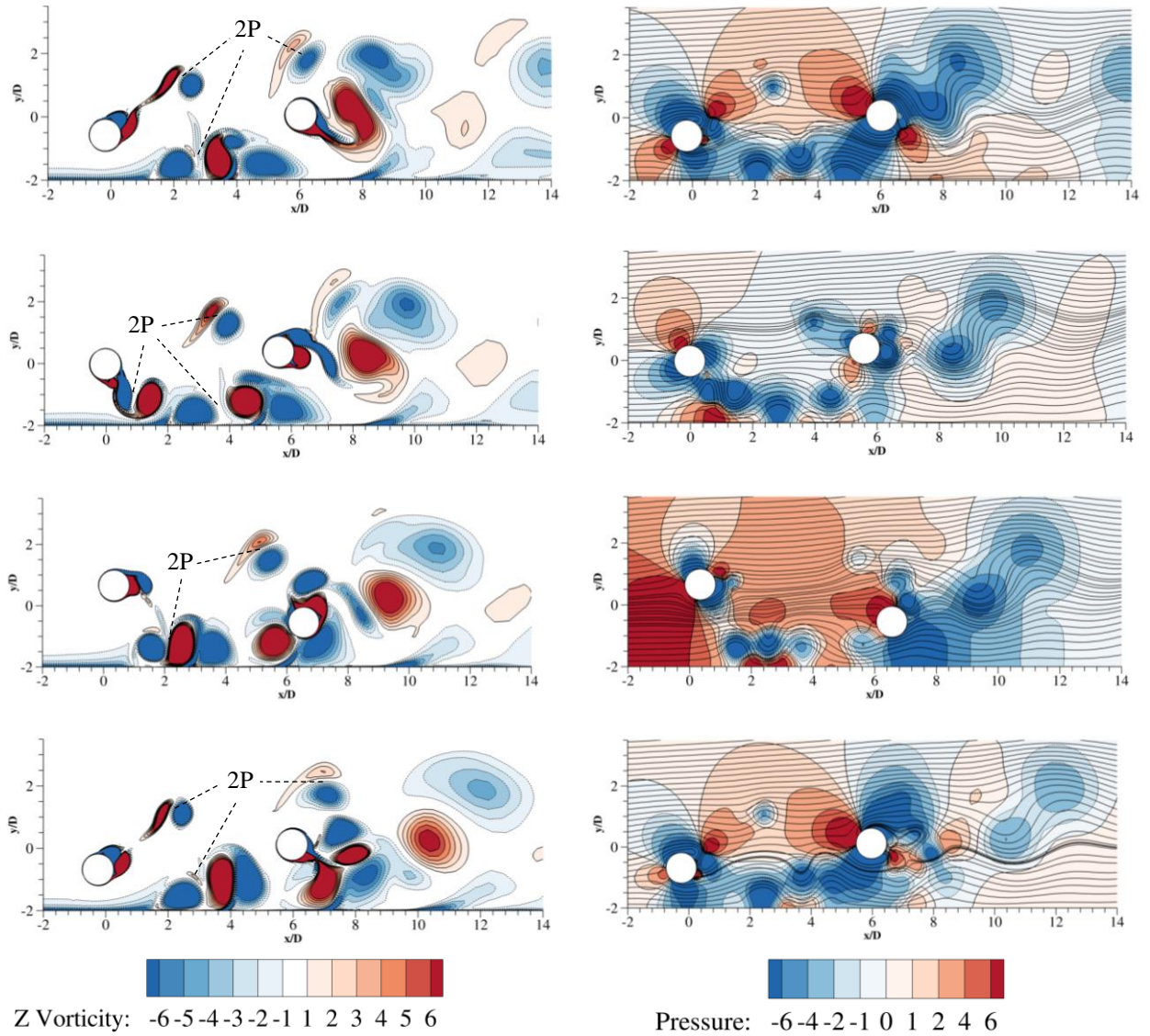


Figure 6.16: Vorticity and pressure contour plots for a vortex shedding cycle at $U_r = 4$, $G^* = 1.5$ and $L^* = 5$. Upstream cylinder is approximately π ahead in phase.

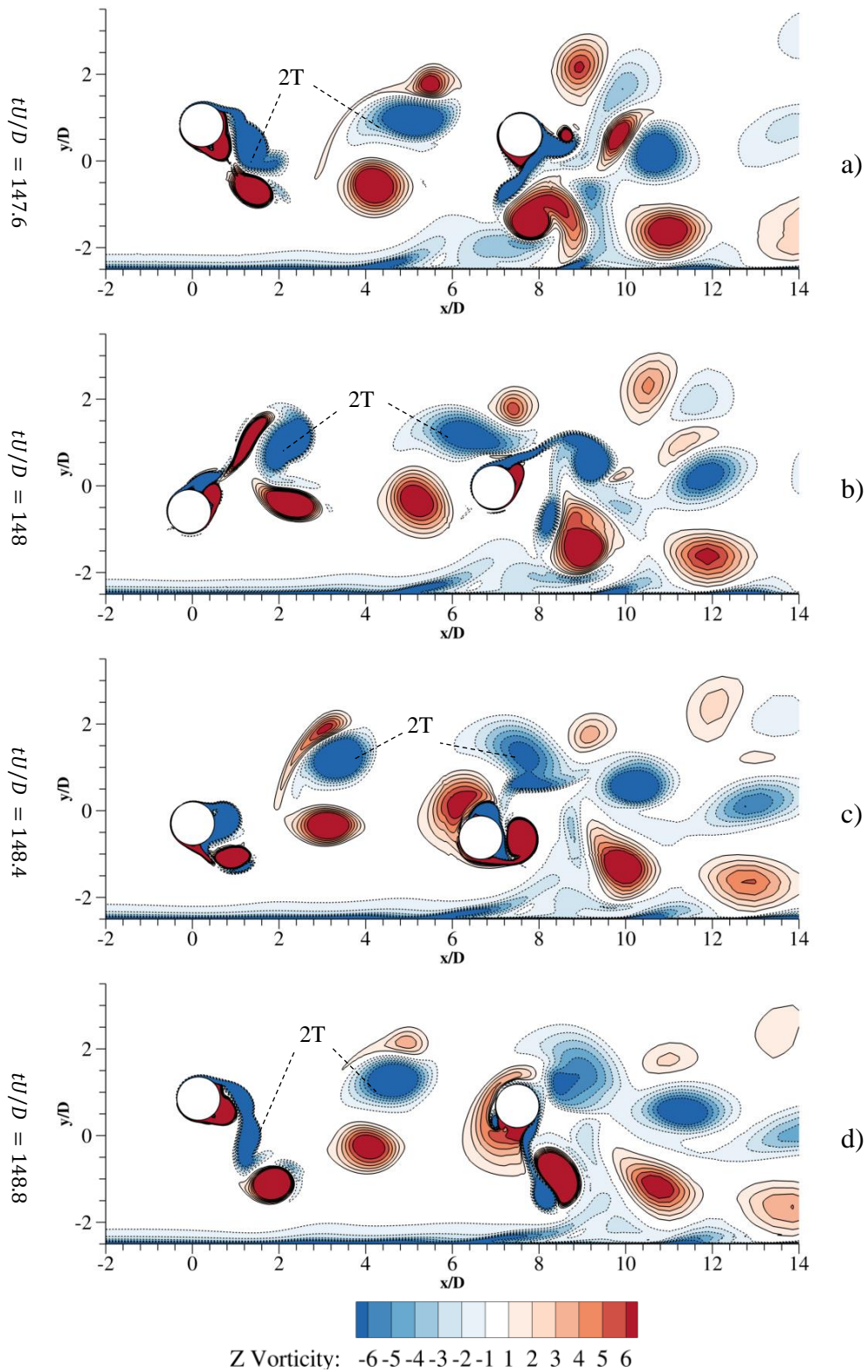


Figure 6.17: Vorticity contour plots at $U_r = 4$, $G^* = 2$ and $L^* = 6$ in which vortices shed upstream impinge the downstream cylinder. Cylinders are in-phase.

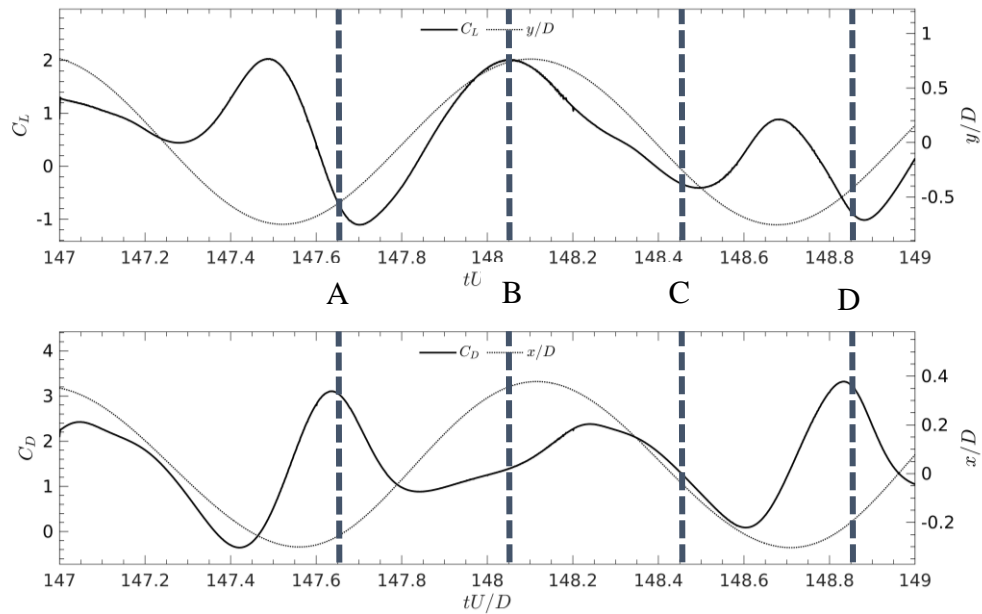


Figure 6.18: Upstream hydrodynamic coefficients and response amplitudes for a period of vortex shedding. Vertical dotted lines A-D are timesteps corresponding to Figure 6.17.

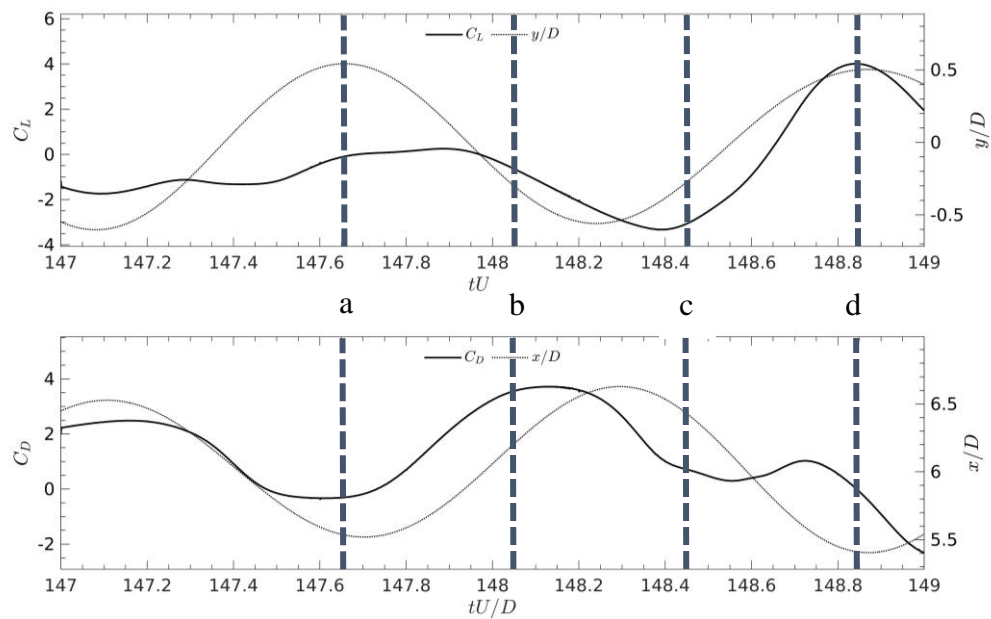


Figure 6.19: Downstream hydrodynamic coefficients and response amplitudes for a period of vortex shedding. Vertical dotted lines a-d are timesteps corresponding to Figure 6.17.

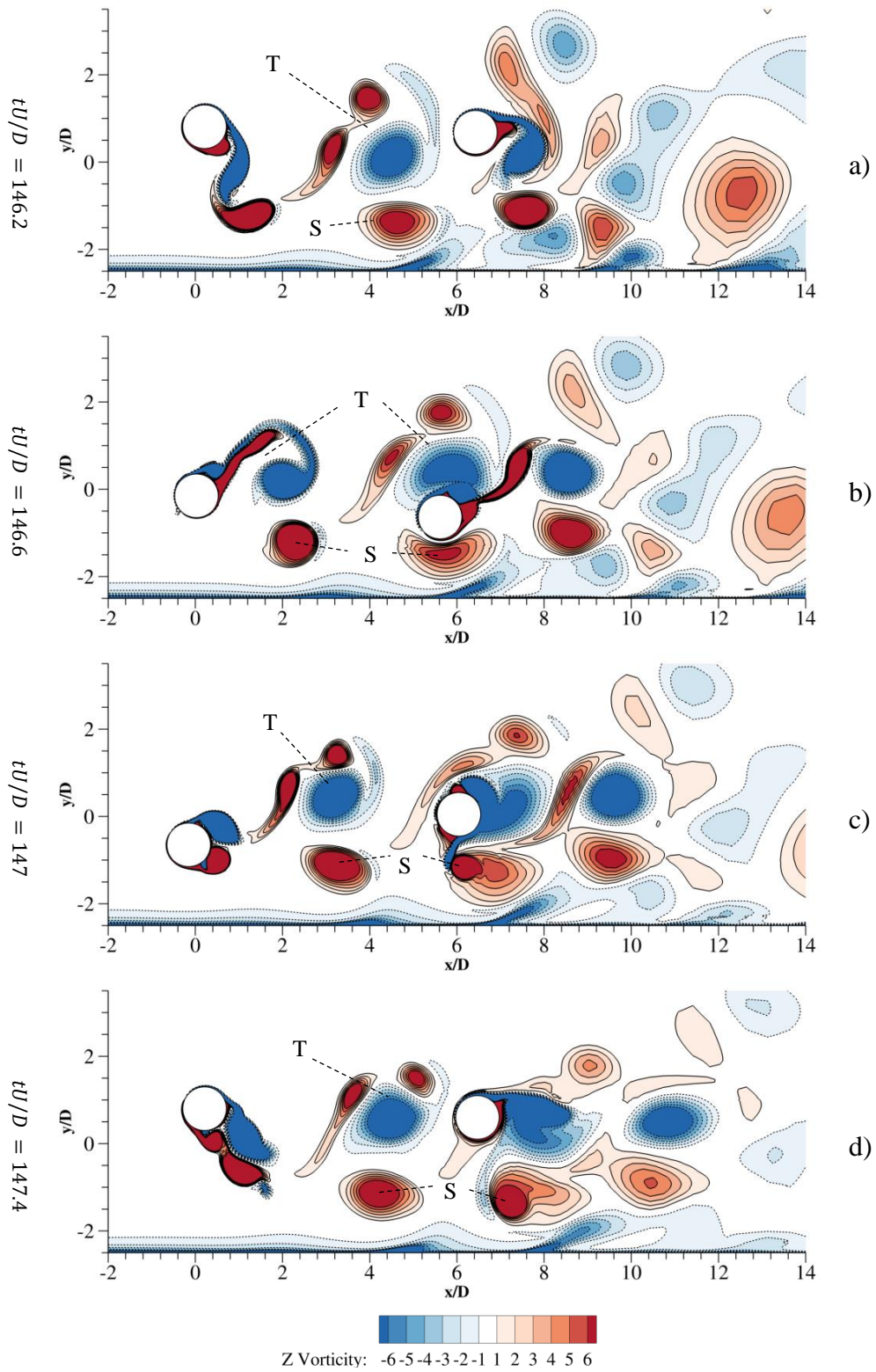


Figure 6.20: Vorticity contour plots at $U_r = 4$, $G^* = 2$ and $L^* = 5$. The upstream cylinder displacement phase is lagging by approximately $\pi/2$.

6.5 Vibration frequency

Fast Fourier Transform (FFT) is applied to compute and analyze the frequency power spectra of both hydrodynamic coefficients and in-line and transverse displacements. Spectra for all simulations are provided in Appendix C. Figure 6.21 presents the spectra for upstream (Figure 6.21 a), b)) and downstream (Figure 6.21 c), d)) cylinders at reduced velocity $U_r = 5$, gap ratio $G^* = 1.5$ and cylinder spacing $L^* = 5$ against non-dimensional frequency fD/U . The time series used for sampling is $\tau = [100, 150]$.

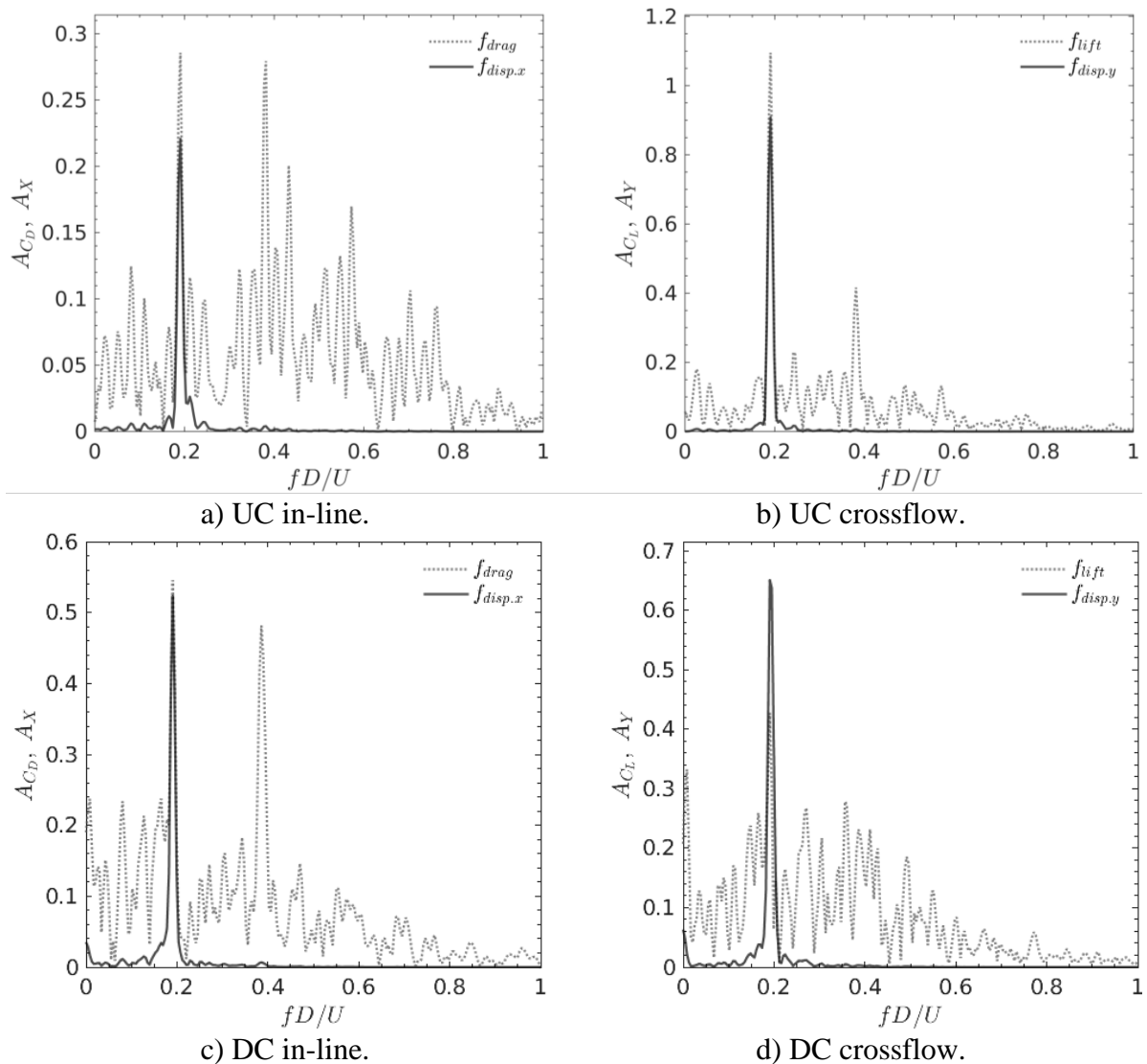


Figure 6.21: Frequency power spectra of hydrodynamic coefficients and displacements for upstream (a) and downstream (b) cylinder at $U_r = 5$, $G^* = 1.5$ and $L^* = 5$.

Dominant non-dimensional frequencies of both in-line and transverse displacements are equal at $fD/U = 0.191$. This value remains constant for all simulations at the given reduced velocity. Equal frequency of displacement in both directions is reflected in the skewed oval

and circular motion trajectories presented earlier in Figure 6.14. The drag coefficient for the upstream cylinder (Figure 6.21 a)) has two peaks in power spectral density at vibration frequency and twice vibration frequency. A third and fourth harmonic at three and four times vibration frequency is observed. Lift coefficient has a dominant frequency at transverse vibration frequency, with second and third harmonics at two- and threefold vibration frequency. This is very similar to what is found in Tham et al. (2015) for investigations at $U_r = 5, G^* = 1.5, m^* = 10$ at low Reynolds number. Power spectra for $U_r = 4, G^* = 1.5, L^* = 5$ are presented in Figure 6.22. Dominant inline and transverse displacement frequencies are equal at $fD/U = 0.235$ for all investigated configurations at $U_r = 4$, which is higher in magnitude than for $U_r = 5$. Displacement frequency ratio of unity ($f_{disp,x}/f_{disp,y} = 1$) was also found at $U_r = 4$ and $U_r = 5$ in Li et al. (2016) for 2DoF near-wall ($G^* = 0.9$) single cylinder at $Re = 200$. The drag coefficient frequency spectrum is broad-banded for the upstream cylinder (Figure 6.22 a)) whilst downstream frequency has clear spectral peaks (Figure 6.22 c)). This indicates that there is a strong correlation with the upstream wake and the downstream drag.

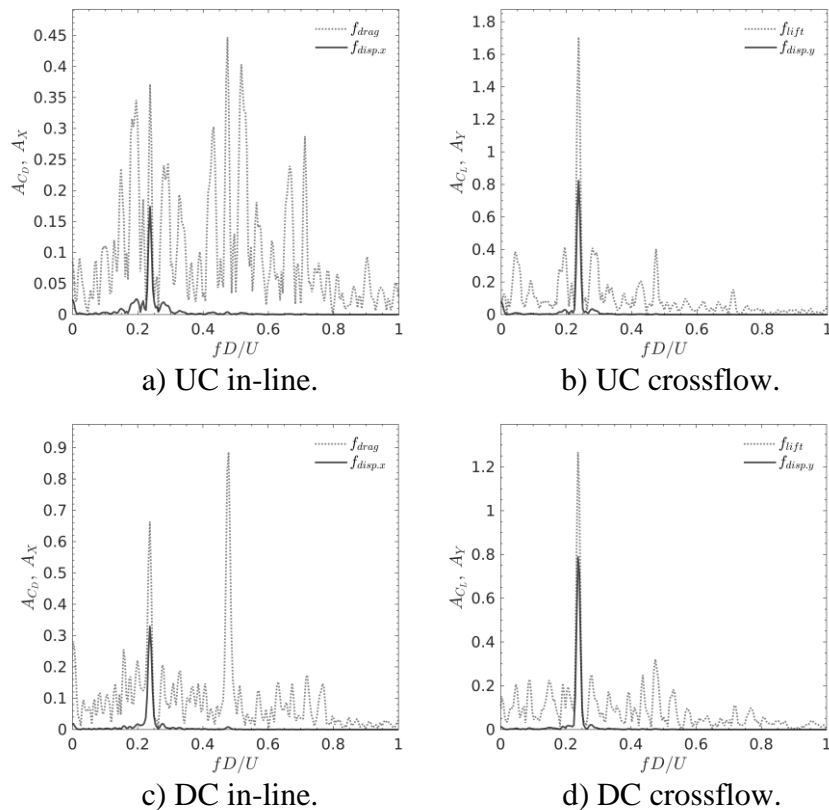


Figure 6.22: Frequency power spectra of hydrodynamic coefficients and displacements for upstream (a) and downstream (b)) cylinder at $U_r = 4, G^* = 1.5$ and $L^* = 5$.

7 CONCLUSIONS AND RECOMMENDATIONS

In the present thesis, a 2D numerical study investigating vortex-induced vibrations (VIV) of 2-degrees-of-freedom (2DoF) tandem cylinders in wall proximity is performed using the CFD package OpenFOAM. Flow fields are simulated, and hydrodynamic forces recorded at very high Reynolds number, $Re = 3.6 \times 10^6$. The present model is using unsteady Reynolds-Averaged Navier-Stokes (URANS) with a $k - \omega$ SST turbulence model. The parameters under investigation are reduced velocity, $U_r = \{4, 5\}$, wall gap-ratio, $G^* = \{1.5, 2\}$ and cylinder spacing $L^* = \{4, 5, 6\}$.

7.1 Conclusions

The following conclusions are drawn from the results presented in Chapters 4, Chapters 5 and Chapters 6.

- Two sets of meshes with different cell densities are created. One for the single static cylinder case and one for the tandem vibrating cylinders case. The static cylinder mesh variant, CS.S.S3, with 44 000 cells is chosen for further work. A mesh sensitivity study shows less than 3 % change in computed hydrodynamic quantities between mesh variant CS.S.S3 and a finer mesh. A model validation study shows a good agreement with similar numerical studies. The CS.S.S3 mesh is modified to include a second cylinder and used for simulations with vibrating cylinders. A second sensitivity study is performed, and a mesh variant CS.T3, with 86 000 cells, is chosen for further simulations. $\overline{C_D}$, $A_{Y,max}/D$, $A_{X,max}/D$ and Strouhal number obtained on mesh CS.T3 show less than 5 % relative change when comparing to the finer CS.T4 mesh. Although the relative change of C_L^{rms} is close to 15 %, it is observed that this variable shows random and chaotic fluctuations in the reasonable sampling period.
- Hydrodynamic coefficients are recorded during the simulations. Mean drag coefficient, $\overline{C_D}$ is smaller for the downstream cylinder compared to the upstream cylinder due to shielding effects and low-pressure zones in the wake of the upstream cylinder. It is shown that $\overline{C_{D,DC}}$ is smaller for smaller cylinder spacing. $\overline{C_D}$ and C_L^{rms} magnitudes are decreasing with increasing reduced velocity for all gap ratios. Beating oscillations of C_L are observed in all investigated cases.

- The maximum measured response amplitudes for transverse displacement are $A_{Y,max}^{UC}/D = 0.9891$ and $A_{Y,max}^{DC}/D = 1.1078$. Both maxima are observed during simulations for $U_r = 5, G^* = 1.5$ and $L^* = 6$ case. The maximum inline response is $A_{X,max}^{UC}/D = 0.509$ at $U_r = 5, G^* = 2, L^* = 4$ and $A_{X,max}^{DC}/D = 0.775$ at $U_r = 4, G^* = 2, L^* = 6$. Simulations show that transverse response amplitudes are larger for $U_r = 5$ than $U_r = 4$. $A_{Y,max}^{UC}$ is increasing with increasing gap ratio, which is in line with similar studies (e.g., Tang et al. (2015)). The in-line maximum response amplitudes are larger for downstream cylinders due to wake interactions. RMS inline responses are increasing with increasing gap ratio. $A_{X,rms}^{DC}/D$ is increasing with L^* at $U_r = 4$, but remains stable with L^* at $U_r = 5$, suggesting weaker vortex impingement at the latter configuration.
- Trajectory plots reveal the irregularity in the motion of vibrating cylinders. At $U_r = 4$ the trajectories are more stable than those at $U_r = 5$ and display a diagonally skewed path. When U_r is increased from $U_r = 4$ to $U_r = 5$, a more oval trajectory is observed. The change in U_r affects the downstream cylinders more than the upstream, resulting in very chaotic downstream cylinder trajectories.
- Flow fields are examined when the cylinders are oscillating in distinct modes identified in the study. When the phase difference in transverse vibration is approximately π , 2P shedding mode is observed for both cylinders. The pair shed on the freestream side upstream is convected laterally upwards in the wake and passes the downstream cylinder without impinging. When the cylinders are oscillating in phase a 2T shedding mode is observed. Impingement of the downstream cylinder is confirmed by examination of vorticity contour plots and by small transverse oscillation amplitudes. At $\pi/2$ phase, a S+T vortex shedding mode is observed. A single strong vortex is shed along the wall, and triplets form on the freestream side.
- Frequency power spectra show the frequency lock-in of both in-line and transverse oscillations. The spectral peaks in the drag and lift force signals are coinciding with the spectral peaks of the in-line and transverse displacements for all the investigated cases. The power spectra of lift coefficient of the downstream cylinder are broad-banded. This

indicates other forcing mechanisms than vortex-induced vibrations alone. It is observed that the additional frequency components can be attributed to the interaction with the wake of the upstream cylinder. The lift coefficient spectra of the upstream cylinders show a clear dominant peak frequency.

7.2 Further work

The following are recommendations for further work:

- Extend the U_r range. Typically for VIV studies, the entire lock-in regime of reduced velocities is considered. In the present study, only $U_r = 4$ and $U_r = 5$ are investigated, which yields very irregular results. It would be interesting to see if simulations would achieve a steady state at some other U_r .
- Extend the L^* range. All of the investigated cylinder spacings fall within the impingement regime. It could be interesting to observe how tandem VIV cylinders behave in the extended-body and reattachment regimes, especially if the L^* regime ranges that are commonly used for static cylinders
- Consider a different motion solver. `pimpleFoam` is very limited at large displacements, especially when the cylinder is very close to the wall. A possible alternative would be the use of an overset mesh and the `overPimpleFoam` solver. Although it may be possible to run simulations at lower gap ratios, there is still some uncertainty in the interpolation between overset and background mesh cells.

REFERENCES

- Abrahamsen Prsič, M., Ong, M. C., Pettersen, B. and Myrhaug, D. (2015). *Large eddy simulations of flow around tandem cylinders close to a horizontal wall*. Int. J. Offshore Polar Eng., 25:161-169.
- Achenbach, E. and Heinecke, E. (1981). *On vortex shedding from smooth and rough cylinders in the range of Reynolds numbers 6×10^3 to 5×10^6* . J. Fluid Mech., 109:239-251.
- Anand, N. M. and Tørum, A. (1985). *Free span vibrations of submarine pipelines in steady flows – effect of free-stream turbulence on mean drag coefficients*. ASME J. Energy Resour. Technol., 107(4):415-420.
- Andersson, B., Andersson, R., Håkansson, L., Mortensen, M., Sudiyo, R., van Wachem, B. and Hellström, L. (2012) *Computational Fluid Dynamics for Engineers*. Cambridge University Press.
- Assi, G. R. S., Meneghini, J. R., Aranha, J., Bearman, P. W. and Casaprima, E. (2006). *Experimental investigation of flow-induced vibration interference between two circular cylinders*. J. Fluids Struct., 22:819-827.
- Assi, G. R. S., Bearman, P. W. and Meneghini, J. R. (2010). *On the wake-induced vibration of tandem circular cylinders: the vortex interaction excitation mechanism*. J. Fluid Mech., 661:365-401.
- Assi, G. R. S., Bearman, P. W., Carmo, B. S., Meneghini, J. R., Sherwin, S. J. and Willden, R. H. J. (2013). *The role of wake stiffness on the wake-induced vibration of the downstream cylinder of a tandem pair*. J. Fluid Mech., 718:21-245.
- Bearman, P. W. and Zdravkovich, M. M. (1978). *Flow around a circular cylinder near a plane boundary*. J. Fluid Mech., 89:33-47.
- Bearman, P. W. (2011). *Circular cylinder wakes and vortex-induced vibrations*. J. Fluids Struct., 27:648-658
- Bhattacharyya, S. and Dhinakaran, S. (2008). *Vortex shedding in shear flow past tandem square cylinders in the vicinity of a plane wall*. J. Fluids Struct., 24:400-417.

- Blevins, R. D. (1990). *Flow-induced Vibration*. Van Nostrand Reinhold.
- Bokaian, A. and Geoola, F. (1984). *Wake-induced galloping of two interfering circular cylinders*. J. Fluid Mech., 146:383-415.
- Brika, D. and Laneville, A. (1999). *The flow interaction between a stationary cylinder and a downstream flexible cylinder*. J. Fluids Struct., 13:579-606.
- Catalano, P., Wang, M., Iccarino, G. and Moin, P. (2003). *Numerical simulation of the flow around a circular cylinder at high Reynolds number*. Int. J. Heat and Fluid Flow, 24:463-469.
- Çengel, Y. A. and Cimbala, J. M. (2017). *Fluid Mechanics*. Mc-Graw Hill Higher Education.
- Chakrabarti, S. K. (1987). *Hydrodynamics of Offshore Structures*. Springer, 1st edition.
- Chung, M. H. (2016). *Transverse vortex-induced vibrations of spring-supported circular cylinder translating near a plane wall*. Eur. J. Mech. B/Fluids, 55:88-103.
- Daneshvar, S. and Morton, C. (2017). *Vortex-induced vibration of a circular cylinder with low mass ratio near a plane wall*. ASME 2017 Fluids Eng. Div. Summer Meeting.
- DNV GL (2017). *Free Spanning Pipelines – Recommended Practice*. Standard, DNV GL, Oslo, Norway.
- D'Souza, J. E., Jaiman, R. K. and Mak, C. K. (2016). *Dynamics of tandem cylinders in the vicinity of a plane moving wall*. Comput. and Fluids, 124:117-135.
- Feng, C. C. (1968). *The measurement of vortex-induced effects in flow past stationary and oscillating circular and D-section cylinders*. Master's thesis. Univ. BC., Vancouver, Can.
- Fredsøe, J., Sumer, B. M., Andersen, J. and Hansen, E. (1987). *Transverse vibrations of a cylinder very close to a plane wall*. ASME J. Offshore Mech. Arct. Eng., 109(1):52-60.
- Fu, S., Xu, Y. and Chen, Y. (2014). *Seabed effects on the hydrodynamics of a circular cylinder undergoing vortex-induced vibrations at high Reynolds number*. Ocean Eng., 140(3):1-12.
- Govardhan R. and Williamson, C. H. K. (2000). *Modes of vortex formation and frequency response for a freely vibrating cylinder*. J. Fluid. Mech., 420:85-130.
- Greenshields, C. J. (2018). *OpenFOAM User Guide, version 6*. OpenFOAM Foundation.
- Harichandan, A. B. and Roy, B. (2012). *Numerical investigation of flow past single and tandem cylindrical bodies in the vicinity of a plane wall*. Phys. Fluids, A(3):1760-1765.

- Igarashi, T. (1982). *Characteristics of a flow around two circular cylinders of different diameters arranged in tandem*. Bulletin of JSME, 25(201):349-357.
- Jacobsen, V., Bryndum, M. B., Nielsen, R. and Fines, S. (1984). *Cross-flow vibrations of a pipe close to a rigid boundary*. ASME J. Energy Resour. Technol. 106(4):451-457.
- Janocha, M. J. (2018). *CFD Simulations of vortex-induced vibrations of a subsea pipeline near a horizontal plane wall*. Master's thesis. Univ. Stavanger, Stavanger, Nor.
- Jasak, H. (1996). *Error Analysis and Estimation for Finite Volume Method with Applications to Fluid Flow*. Ph. D. thesis, Imperial College, University of London.
- Jauvits, N. and Williamson, C. H. K. (2003). *Vortex-induced vibration of a cylinder with two degrees of freedom*. J. Fluids Struct., 17:1035-1042.
- Kim, S., Alam, M. M., Sakamoto, H. and Zhou, Y. (2009). *Flow-induced vibrations of two circular cylinders in tandem arrangement; Part 1*. J. Wind Eng. Ind. Aerodyn., 97(5-6):304-311.
- Lei, C., Cheng, L. and Kavanagh, K. (1999). *Re-examining of the effect of a plane boundary on forces and vortex shedding of a circular cylinder*. J. Wind Eng. Ind. Aerodyn., 80(3):263-286.
- Li, Z., Abrahamsen Prsič, M., Ong, M. C. and Khoo, B. C. (2018). *Large Eddy Simulations of flow around two circular cylinders in tandem in the vicinity of a plane wall at small gap ratios*. J. Fluids Struct. 76:251-271.
- Menter, F. (1994). *Two-equation eddy-viscosity turbulence models for engineering applications*. AIAA Journal, 32:1598-1605.
- Menter, F., Ferreira, J. C., Esch, T. and Konno, B. (2003). *The SST turbulence model with improved wall treatment for heat transfer predictions in gas turbines*. Gas Turbine Congress, Int. Congress Proc. (Tokyo, 2003), pp.1-7.
- Moe, G. and Wu, Z.-J. (1990). *The lift force on a cylinder vibrating in a current*. J. Offshore Mech. Arct. Eng., 112(4):297-303.
- Ong, M. C., Utnes, T., Holmedal, L. E., Myrhaug, D. and Pettersen, B. (2009). *Numerical simulation of flow around a smooth circular cylinder at very high Reynolds numbers*. Marine Struct., 22:142-153.

Ong, M. C., Utnes, T., Holmedal, L. E., Myrhaug, D. and Pettersen, B. (2010). *Numerical simulation of flow around a circular cylinder close to a flat seabed at high Reynolds number using a $k - \epsilon$ model*. *Coast. Eng.*, 57:931-947.

Panton, R. L. (2013). *Incompressible Flow*. Wiley.

Rao, A., Thompson, M. C., Leweke, T. and Hourigan, K. (2013). *Dynamics and stability of the wake behind tandem cylinders sliding along a wall*. *J. Fluid Mech.*, 772:291-316.

Rashidi, S., Hayatdavoodi, M. and Esfahani, J. A. (2016). *Vortex Shedding Suppression and Wake Control: A Review*. *Ocean Engineering*, 126:57-80.

Sarpkaya, T. (1995). *Hydrodynamic damping, flow-induced oscillations, and biharmonic response*. *J. Offshore Mech. Arct. Eng.*, 117:232-238

Sarpkaya, T. (2004). *A critical review of the intrinsic nature of vortex-induced vibrations*. *J. Fluids Struct.*, 19:389-447

Sarpkaya, T. (2010). *Wave forces on offshore structures*. Cambridge University Press.

Schewe, G. (1983). *On the force fluctuations acting on a circular cylinder in crossflow from subcritical up to transcritical Reynolds numbers*. *J. Fluid Mech.*, 133:265-285.

Singh, S. P. and Mittal, S. (2005). *Flow past a cylinder: shear layer instability and drag crisis*. *Int. J. Numer. Meth. Fluids*, 47:75-98.

Sumer, B. M. and Fredsøe, J. (2006). *Hydrodynamics around cylindrical structures*. World Scientific, Singapore.

Tang, G. Q., Chen, C. Q., Zhao, M. and Lu, L. (2015). *Numerical simulation of flow past twin near-wall circular cylinders in tandem arrangement at low Reynolds number*. *Water Sci. Eng.*, 8(4):315-325.

Tennekes, H. and Lumley, J. L. (1972). *A first course in Turbulence*. Cambridge, MA: MIT Press.

Tham, D. M. Y., Gurugubelli, P. S., Li, Z. and Jaiman, R. K. (2015). *Freely vibrating circular cylinder in the vicinity of a stationary wall*. *J. Fluids Struct.*, 59:103-128.

Versteeg, H., and Malalasekera W. (2007). *An Introduction to Computational Fluid Dynamics: The Finite Volume Method*. Pearson Education, 2nd Edition.

-
- Wang, X. K., Hao, Z. and Tan, S. K. (2013). *Vortex-induced vibrations of a neutrally buoyant circular cylinder near a plane wall*. J. Fluids Struct., 39:188-204.
- Wang, X. K., Zhang, J.-X., Hao, Z., Zhou, B. and Tan, S. K. (2015). *Influence of wall proximity on flow around two tandem circular cylinders*. Ocean Eng., 94:36-50.
- White, F. M. (2006). *Viscous Fluid Flow*. Mc-Graw Hill Higher Education.
- Wilcox, D. (2006). *Turbulence modeling for CFD*. DCW Industries.
- Williamson, C. H. K. and Govardhan, R. (2004). *Vortex-Induced Vibrations*. Annu. Rev. Fluid Mech., 36:413-455.
- Williamson, C. H. K. and Govardhan, R. (2008). *A brief review of recent results in vortex-induced vibrations*. J. Wind Eng. Ind. Aerodyn. 96:713-735.
- Williamson, C. H. K. and Roshko, A. (1988). *Vortex formation in the wake of an oscillating cylinder*. J. Fluids Struct., 2:355-381.
- Yang, B., Gao, F., Jeng, D.-S. and Wu, Y. (2009). *Experimental study of vortex-induced vibrations of a cylinder near a rigid plane boundary in steady flow*. Acta Mech. Sin., 25:51-63.
- Zdravkovich, M. M. (1977). *Review of flow interference between two circular cylinders in various arrangements*. J. Fluids Eng., 99(4):618-633.
- Zdravkovich, M. M. (1985). *Forces on a circular cylinder near a plane wall*. Appl. Ocean Res., 7(4):197-201.
- Zdravkovich, M. M. (1987). *The effects of interference between circular cylinders in cross flow*. J. Fluids Struct., 1:239-261.
- Zhao, M. and Cheng, L. (2011). *Numerical simulation of two-degree-of-freedom vortex-induced vibration of a circular cylinder close to a plane boundary*. J. Fluids Struct. 27:1097-1110.
- Zhou, Y. and Yiu, M. W. (2006). *Flow structure, momentum and heat transport in a two-tandem-cylinder wake*. J. Fluid Mech., 548:17-48.

APPENDIX A: TIMESERIES OF HYDRODYNAMIC COEFFICIENTS

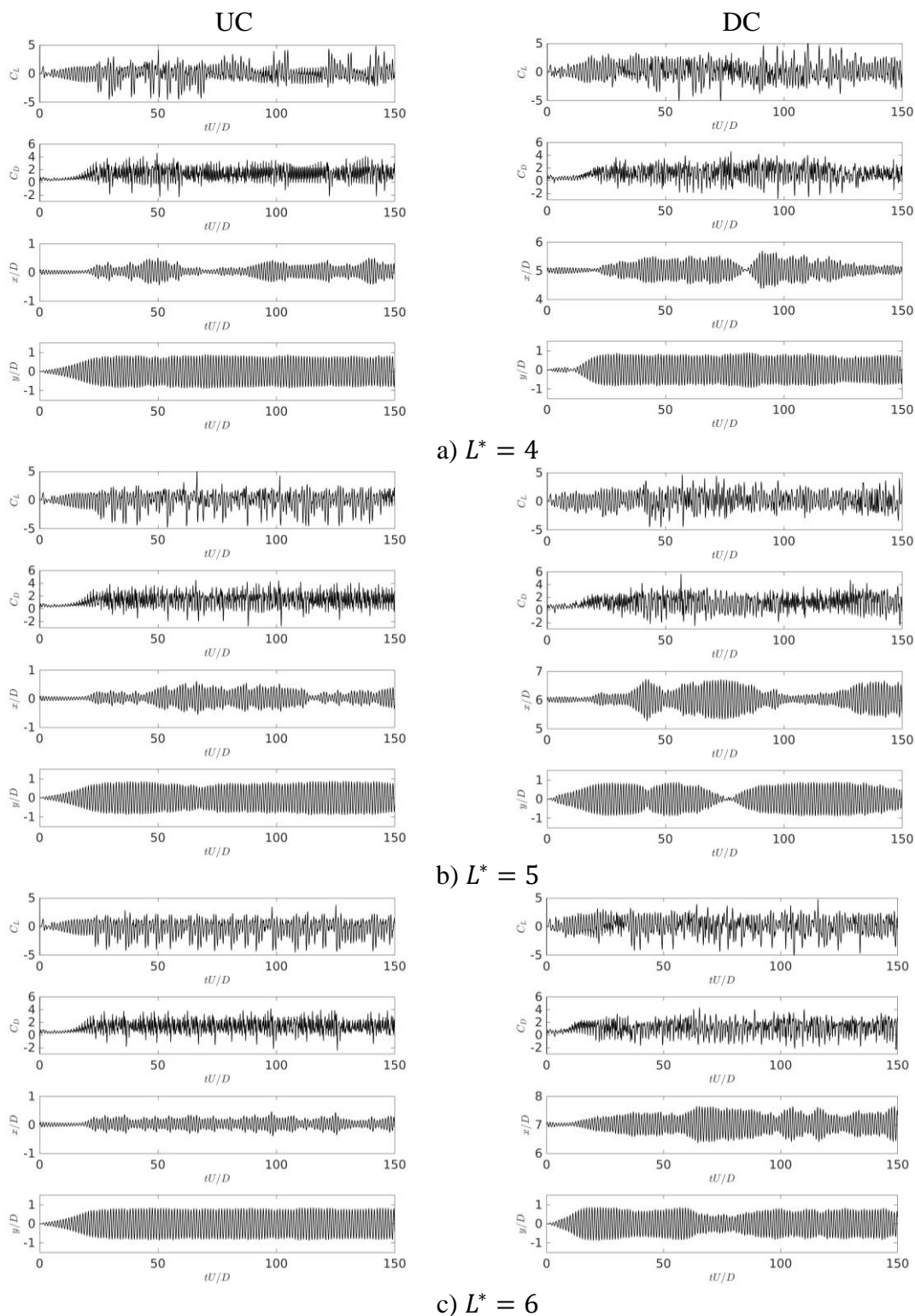
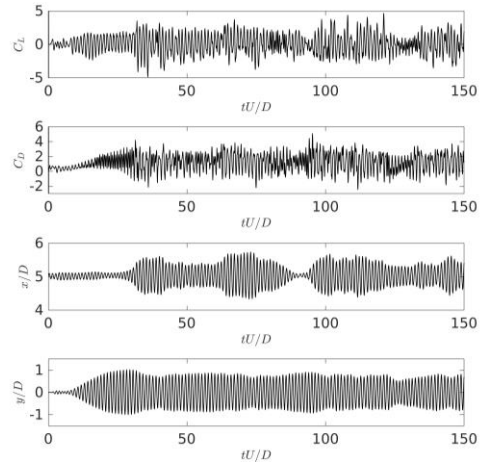
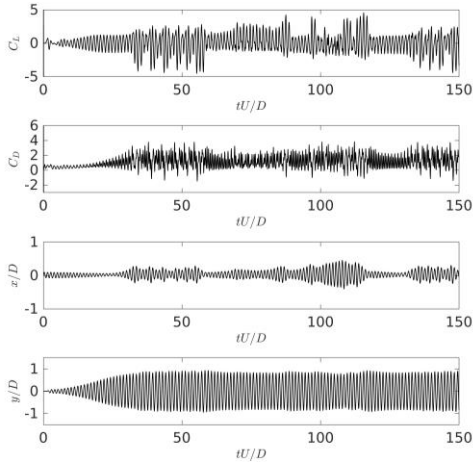


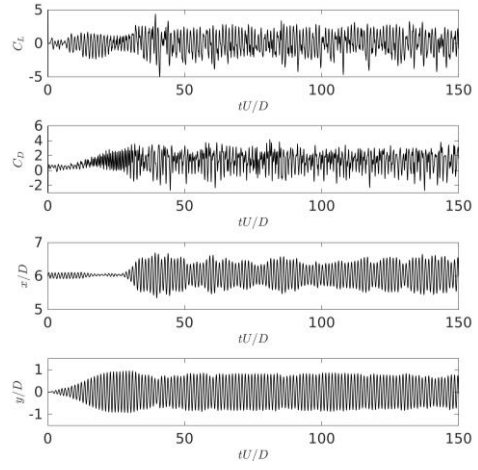
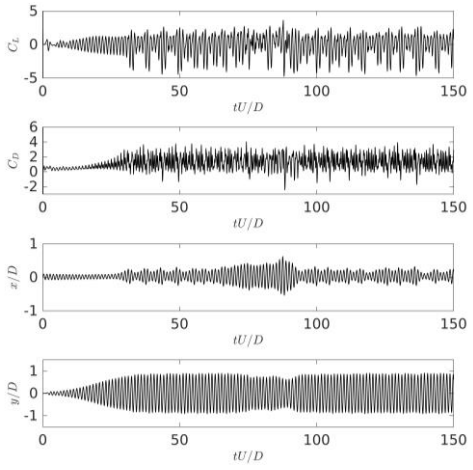
Figure A1: Hydrodynamic coefficients and displacements at $U_r = 4$, $G^* = 1.5$.

UC

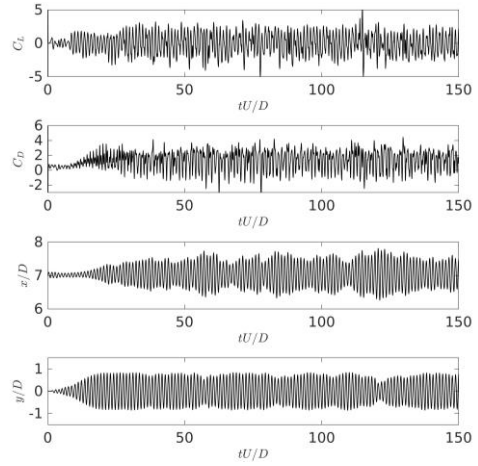
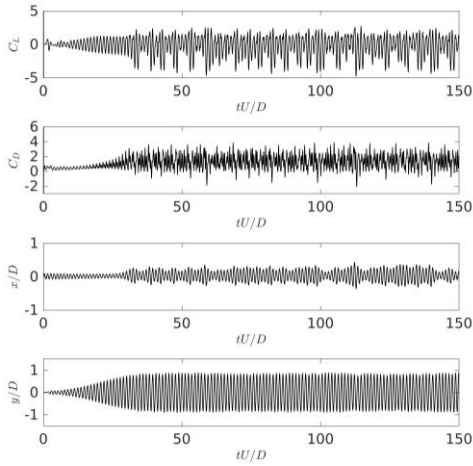
DC



a) $L^* = 4$



b) $L^* = 5$



c) $L^* = 6$

Figure A2: Hydrodynamic coefficients and displacements at $U_r = 4$, $G^* = 2$.

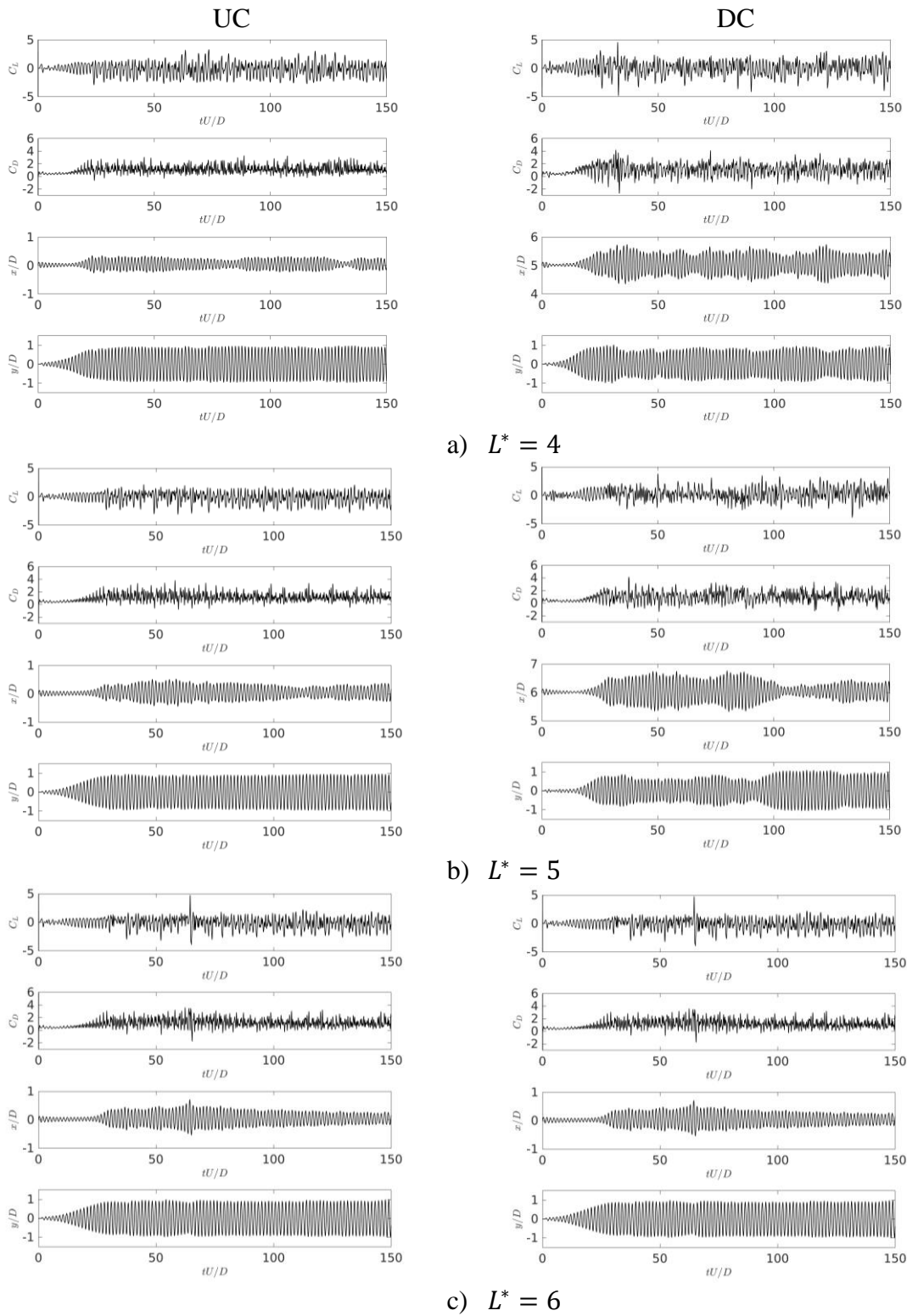


Figure A3: Hydrodynamic coefficients and displacements at $U_r = 5$, $G^* = 1.5$.

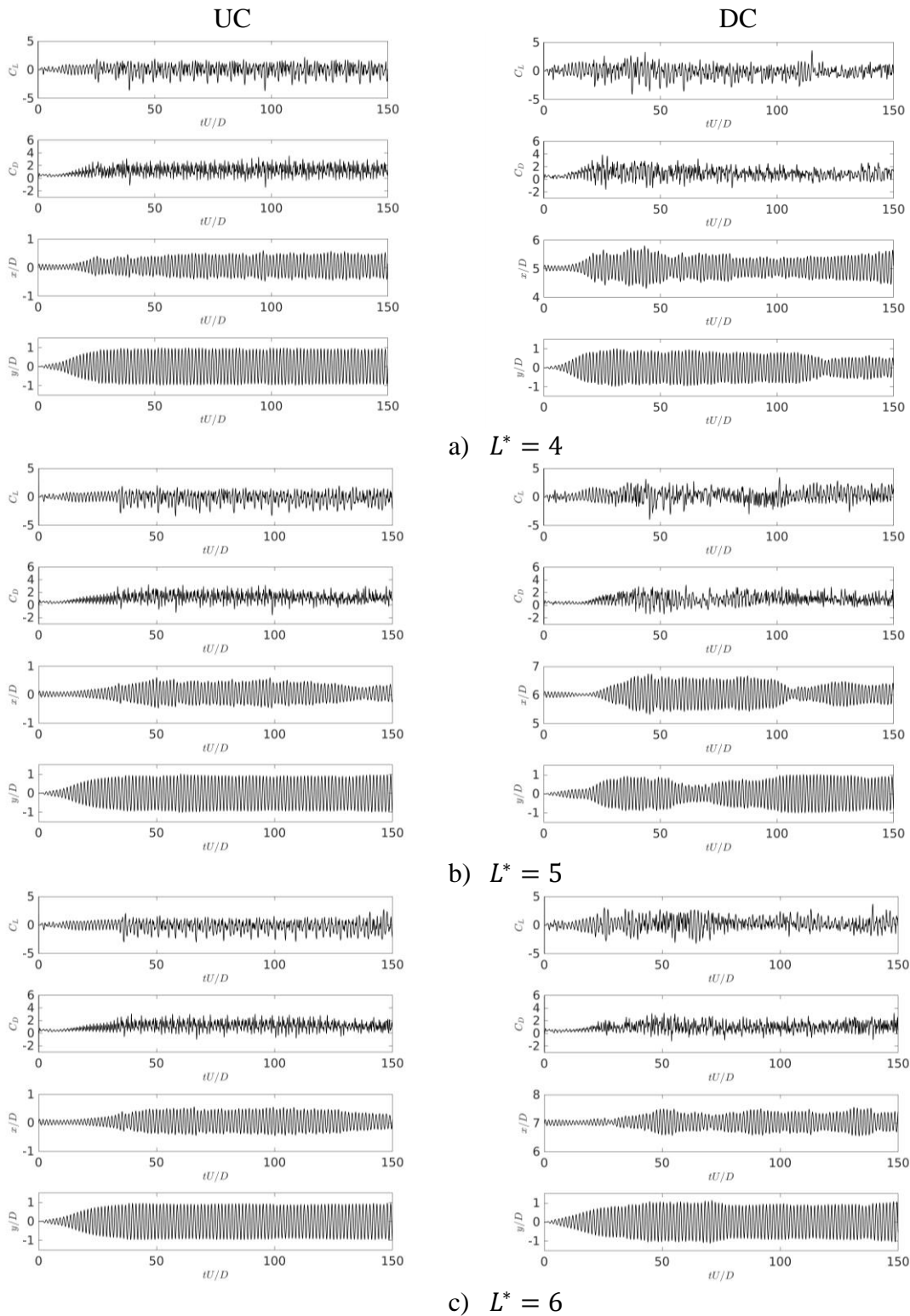
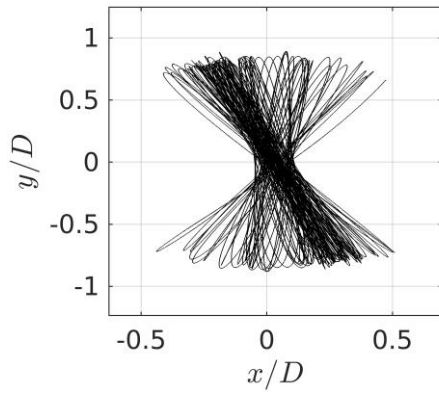
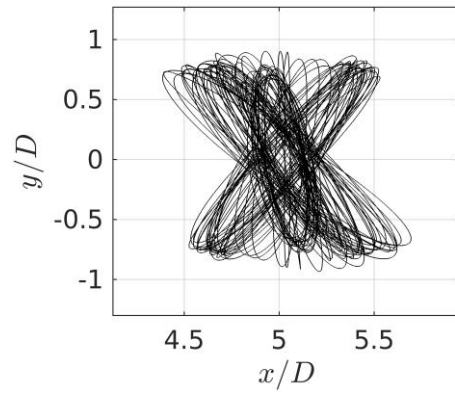


Figure A4: Hydrodynamic coefficients and displacements at $U_r = 5$, $G^* = 2$.

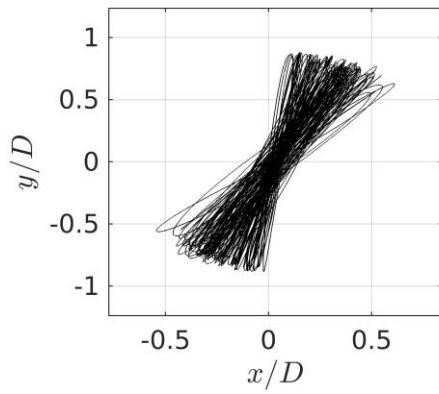
APPENDIX B: MOTION TRAJECTORIES



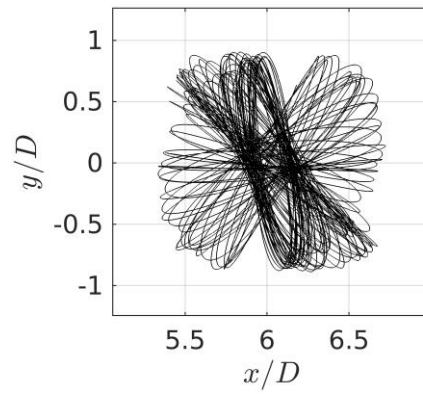
a) UC, $L^* = 4$



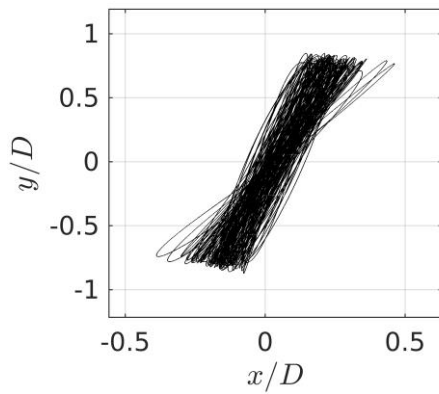
b) DC, $L^* = 4$



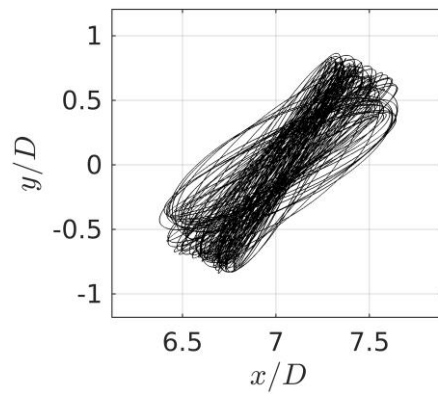
c) UC, $L^* = 5$



d) DC, $L^* = 5$

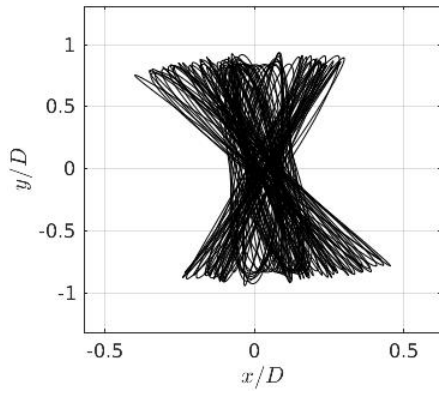


e) UC, $L^* = 6$

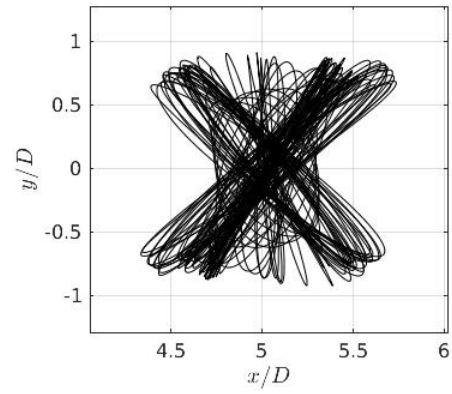


f) DC, $L^* = 6$

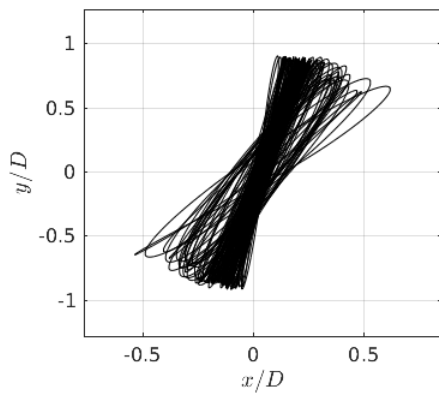
Figure B1: Motion trajectories for $U_r = 4$, $G^* = 1.5$.



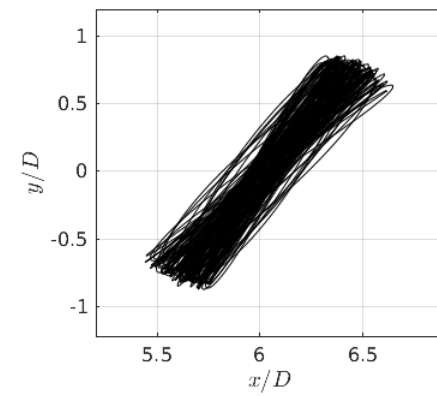
a) UC, $L^* = 4$



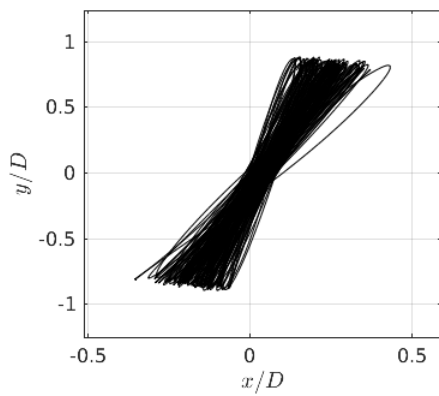
b) DC, $L^* = 4$



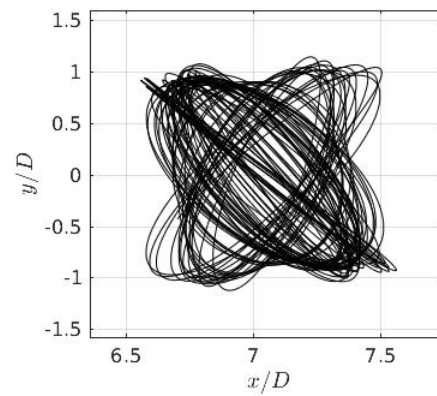
c) UC, $L^* = 5$



d) DC, $L^* = 5$

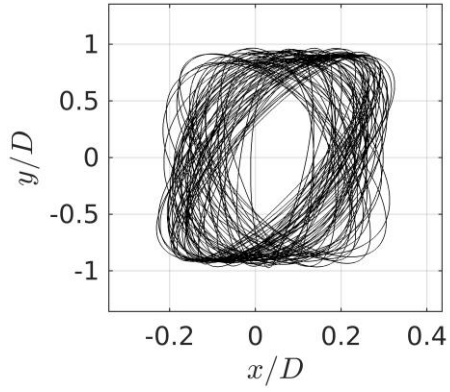


e) UC, $L^* = 6$

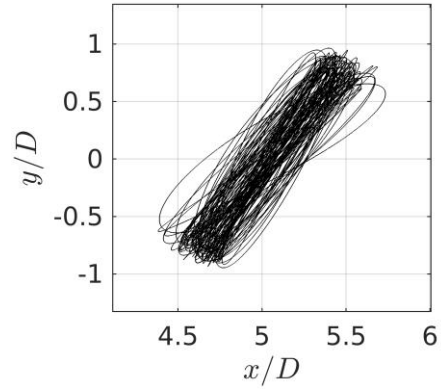


f) DC, $L^* = 6$

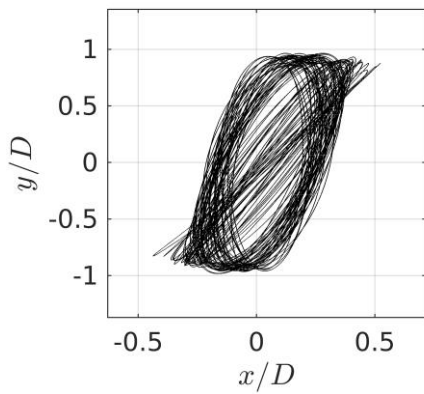
Figure B2: Motion trajectories for $U_r = 4$, $G^* = 2$.



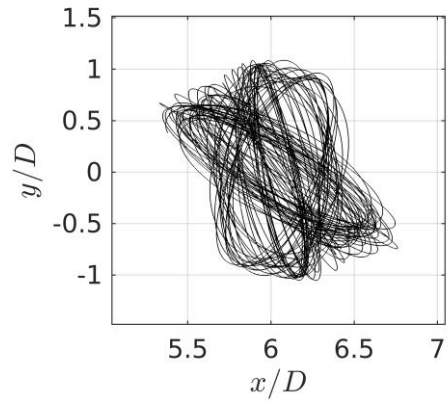
a) UC, $L^* = 4$



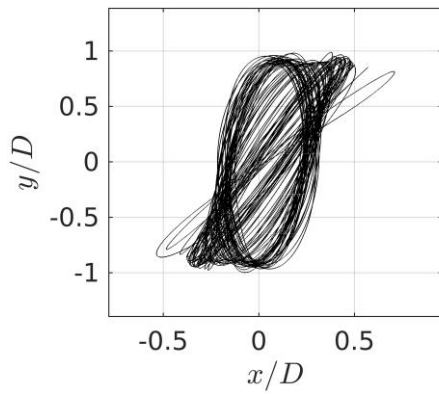
b) DC, $L^* = 4$



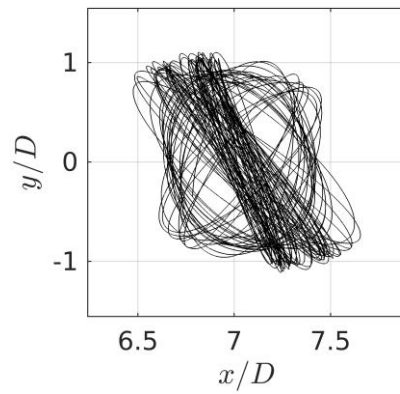
c) UC, $L^* = 5$



d) DC, $L^* = 5$

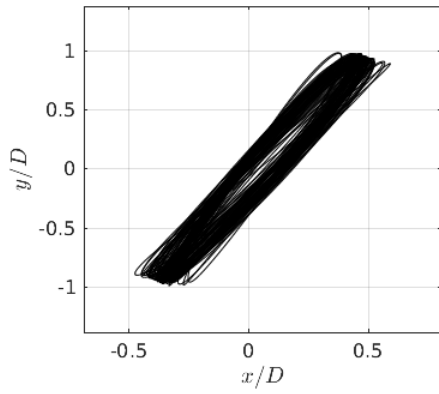


e) UC, $L^* = 6$

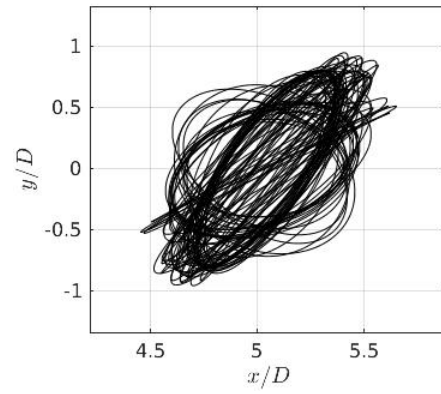


f) DC, $L^* = 6$

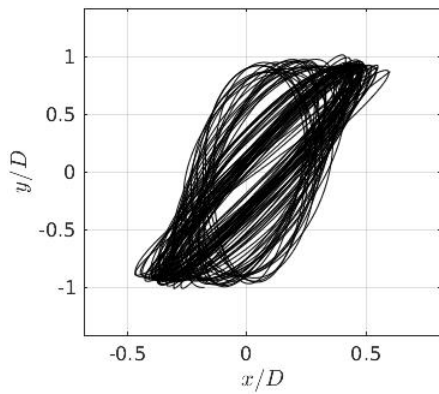
Figure B3: Motion trajectories for $U_r = 5$, $G^* = 1.5$.



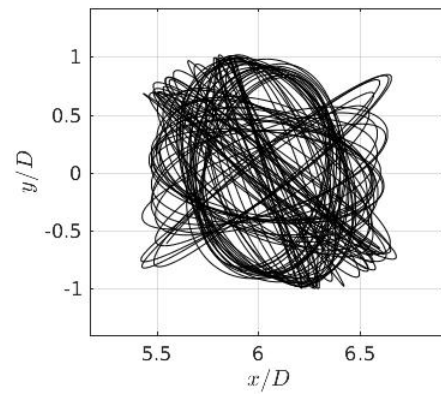
a) UC, $L^* = 4$



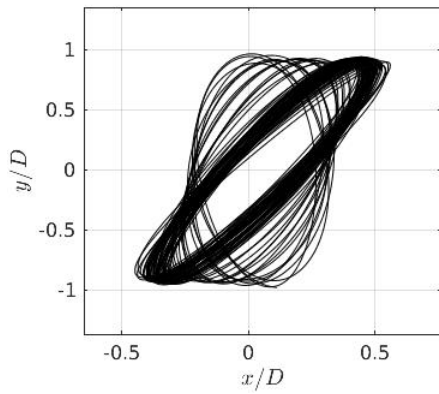
b) DC, $L^* = 4$



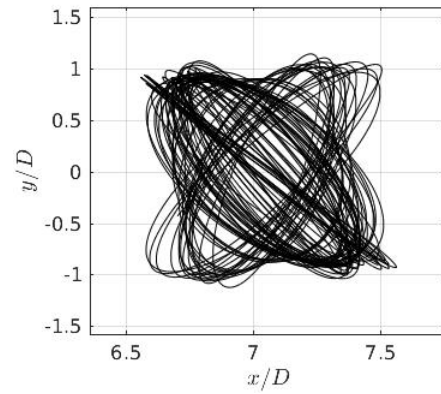
c) UC, $L^* = 5$



d) DC, $L^* = 5$



e) UC, $L^* = 6$



f) DC, $L^* = 6$

Figure B4: Motion trajectories for $U_r = 5$, $G^* = 2$.

APPENDIX C: FREQUENCY POWER SPECTRA

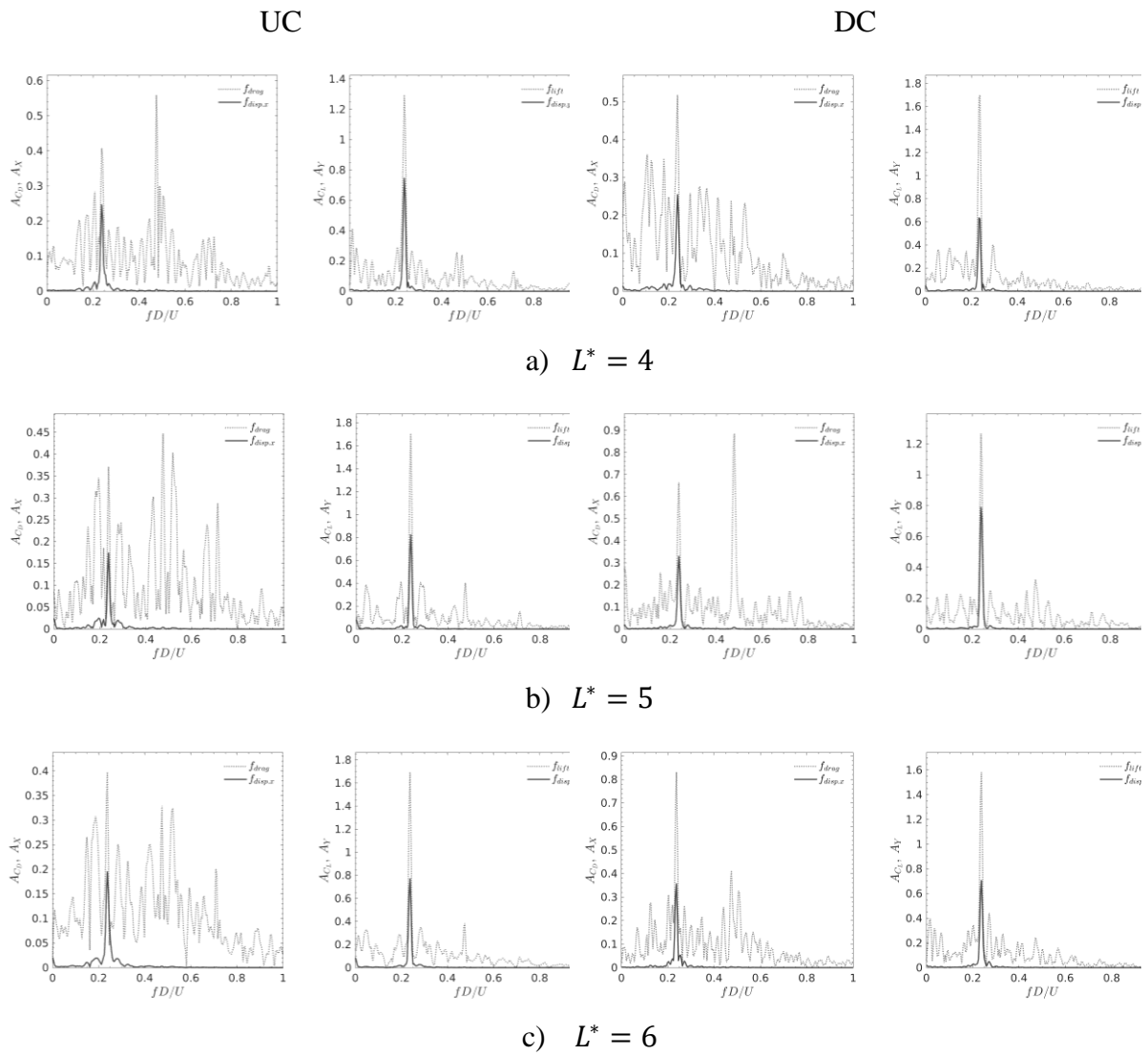


Figure C1: Frequency power spectra for $U_r = 4$ at gap ratio $G^* = 1.5$.

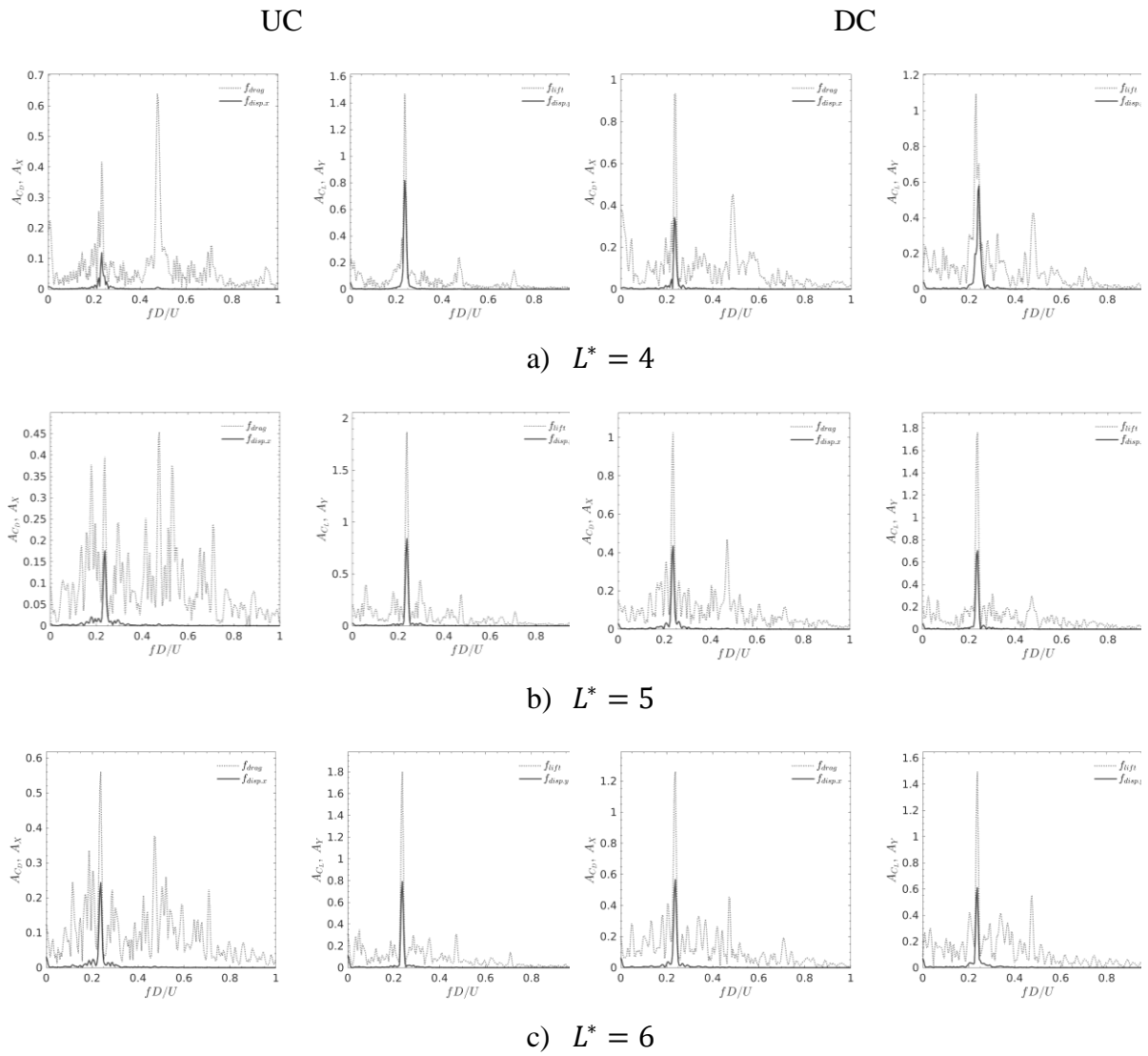


Figure C2: Frequency power spectra for $U_r = 4$ at gap ratio $G^* = 2$.

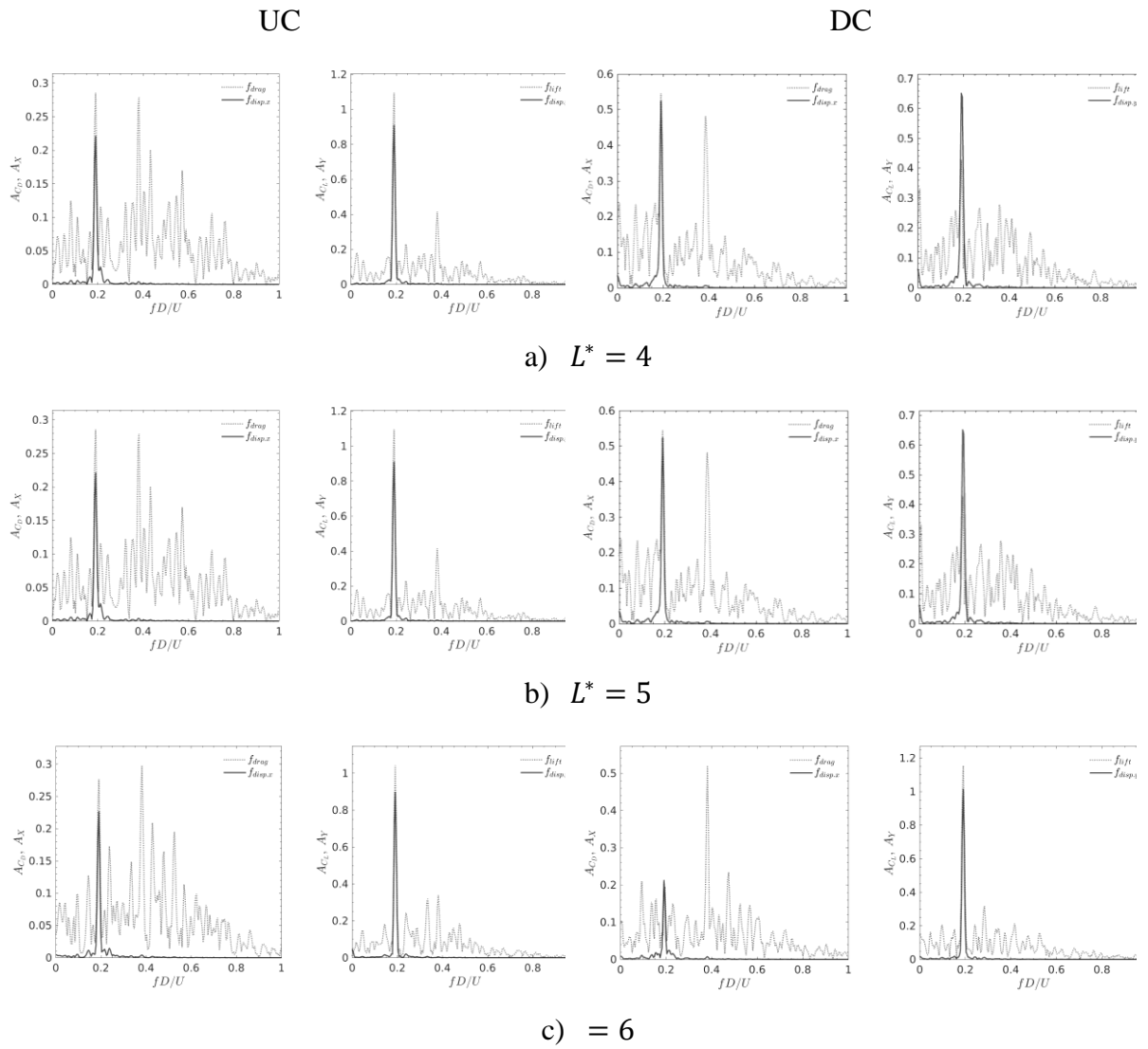


Figure C3: Frequency power spectra for $U_r = 5$ at gap ratio $G^* = 1.5$.

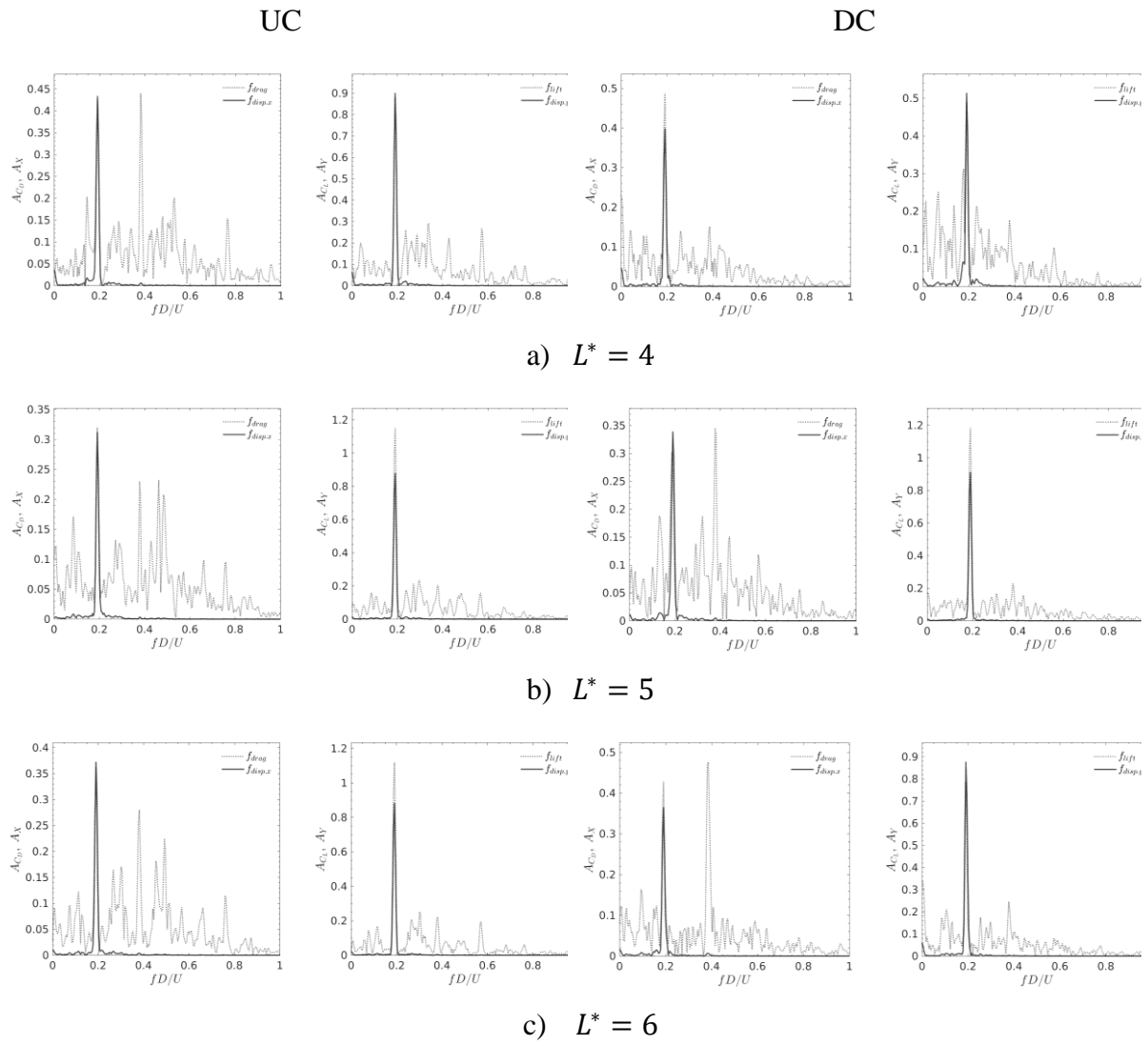


Figure C4: Frequency power spectra for $U_r = 5$ at gap ratio $G^* = 2$.